The role of the transcription factor BCL11A

in midbrain dopaminergic neurons

Dissertation

Zur

Erlangung des Doktorgrades (Dr. rer. Nat.)

der

Mathematisch-Naturwissenschaftlichen Fakultät

der

Rheinischen Friedrich-Wilhelms-Universität Bonn

vorgelegt von

Marianna Tolve

aus

Potenza, Italien

Bonn, 2021

"What we know is a drop, what we don´t know is an ocean."
Isaac Newton

TABLE OF CONTENTS

ABBREVIATIONS

BCL11A   B cell CLL/lymphoma 11a
A1-A14   aminergic1-aminergic14
ADLH1A1   aldehyde dehydrogenase 1a1
APs   action potentials
BLA   basolateral amygdala
CALB1   calcium-binding protein Calbindin1
cko   conditional knock-out
Cli   caudal linear nucleus
CNS   central nervous system
CreER   Cre recombinase fused with a modified form of the human estrogen receptor
CTB   choleratoxin subunit B
CTIP1   Chicken ovalbumin upstream promoter transcription factor-interacting proteins 1
DA   dopamine, dopaminergic
DAT   dopamine transporter
DLS   dorsolateral striatum
DMS   dorsomedial striatum
GABA   γ-aminobutyric acid
GAD   glutamate decarboxlyase
I_A A-type potassium current
IF   interfascicular nucleus
I_H hyperpolarization-activated current
IRES   internal ribosomal entry site
l_SN   lateral SN
LHB   lateral habenula
LMX1A   LIM homeodomain transcription factor 1A
LS   lateral septum
LSD   dorsal region of the lateral septum
LSI   intermediate region of the lateral septum
lSNc   lateral SNc
m_SN   medial SN
mDA   midbrain dopaminergic
mPFC   medial prefrontal cortex
MPTP   1-methyl-4-phenyl-1,2,3,6-tetrahydropyridine
mSNc   medial SNc
NAc   nucleus accumbens
NAcC   nucleus accumbens core
NAcSh   nucleus accumbens shell
NDS   normal donkey serum
NEUROG2   Neurogenin 2
NSC1   neuronal Ca^{2+} sensor 1
OT   olfactory tubercles

PAG	periaqueductal gray
PBP	parabrachial pigmented nucleus
PD	Parkinson´s disease
pDMS	posterior dorsomedial striatum
PF	positive feedback
PFA	paraformaldehyde
PN	paranigral nucleus
qPCR	quantitative polymerase chain reaction
rAAV	recombinant adeno-associated viruses
RLi	rostral linear nucleus of the raphe
RRF	retrorubral field
RT	room temperature
SEM	standard error of the mean
Sema3c	semaphorin 3c
SHH	sonic hedgehog
SN	substantia nigra
SNc	substantia nigra pars compacta
SNl	substantia nigra pars lateralis
SNr	substantia nigra pars reticulata
tetO	tet operator
TH	tyrosine hydroxylase
TM	Tamoxifen
TRE	tetracycline response element
TS	tail of the striatum
TSd	dorsal TS
TSv	ventral TS
tTA	tertacycline responsive transactivator
VGAT	vesicular GABA transporter
Vglut2	vesicular glutamate transporter 2
VMAT2	vesicular monoamine transporter 2
VTA	ventral tegmental area

SUMMARY

Midbrain dopaminergic (mDA) neurons are located in three midbrain nuclei, the substantia nigra (SN), ventral tegmental area (VTA) and retrorubral field (RRF). mDA neurons are diverse in their developmental origin, their gene expression, their projection targets, their electrophysiological and functional properties, their ability to co-release other neurotransmitters together with dopamine and their vulnerability to neurodegeneration. Little is known about the molecular mechanisms that establish this diversity in mDA neurons during development.

Diverse cellular programs have to be executed and maintained during differentiation and maturation to establish mDA neurons with distinct projections and functions. Transcription factors are known to direct these cellular differentiation programs. In this study the expression of a zinc finger transcription factor, BCL11A (B-cell lymphoma 11a), has been characterized in both the developing and adult murine brain, to examine whether BCL11A is expressed in a subset of mDA neurons. To explore whether *Bcl11a*-expressing mDA neurons form a highly specific subcircuits within the dopaminergic (DA) system, intersectional fate mapping, anterograde viral mediated tracing and retrograde tracing approaches were combined. To investigate whether BCL11A is necessary for establishing and/or maintaining *Bcl11a*-expressing mDA neurons and their cell fate, a conditional knock-out mouse model for *Bcl11a* in mDA neurons was generated. A set of behavioural experiments was carried out to assess whether the loss of *Bcl11a* leads to functional impairment in the mDA system, Moreover, to elucidate the role of *Bcl11a* expression in the context of neuronal challenges and neurodegenerative processes affecting mDA neurons in the SN, mDA neurons were challenged with α-synuclein overexpression.

The results of this study reveal that BCL11A is expressed in about a third of mDA neurons in the SN, VTA and RRF and that *Bcl11a*-expressing mDA neurons contribute to several known subpopulations of mDA neurons. Intersectional labelling and tracing experiments show that *Bcl11a*-expressing mDA neurons, despite their broad anatomical distribution, form a highly specific subcircuit within the DA system. *Bcl11a* specific inactivation in mDA neurons led to changes in the anatomical positioning of *Bcl11a*-expressing mDA neurons. Moreover, mice lacking *Bcl11a* expression in mDA neurons show deficiencies in motor learning, suggesting that loss of *Bcl11a* results in a functional impairment of mDA neurons. Furthermore, by challenging mDA neurons with α-synuclein overexpression, a model of Parkinson's disease, *Bcl11a*-expressing SN neurons have been shown to be particularly vulnerable to neurodegeneration. Additionally, the loss of *Bcl11a* in this population increases their susceptibility to α-synuclein-induced degeneration.

This study links the developmental origin of a specific subset of mDA neurons to their vulnerability phenotype and functional and circuit specialization. Thus, the results of this study demonstrate that a better understanding of the genetically defined developmental history of mDA neurons is instrumental to understand the functional organization of the DA system and its susceptibility to neurodegeneration in the adult brain.

ZUSAMMENFASSUNG

Dopaminerge Neuronen des Mittelhirns (mDA) befinden sich in drei Kerngebieten des Mittelhirns, der Substantia nigra (SN), dem ventralen tegmentalen Areal (VTA) und dem retrorubralen Feld (RRF). mDA-Neurone unterscheiden sich in ihrem entwicklungsbedingten Ursprung, ihrer Genexpression, ihren Projektionszielen, ihren elektrophysiologischen und funktionellen Eigenschaften, ihrer Fähigkeit, andere Neurotransmitter zusammen mit Dopamin freizusetzen und ihrer Anfälligkeit für Neurodegeneration. Über die molekularen Mechanismen, die diese Vielfalt in mDA-Neurone während der Entwicklung etablieren, ist jedoch wenig bekannt.

Diverse zelluläre Programme müssen während der Differenzierung und Reifung ausgeführt und aufrechterhalten werden, um mDA-Neuronen mit unterschiedlichen Projektionen und Funktionen zu etablieren. Transkriptionsfaktoren sind dafür bekannt, diese zellulären Differenzierungsprogramme zu steuern. In dieser Studie wurde die Expression eines Zinkfinger-Transkriptionsfaktors, BCL11A (B-Zell-Lymphom 11a), sowohl im sich entwickelnden als auch im adulten murinen Gehirn charakterisiert, um zu untersuchen, ob BCL11A in einer Untergruppe von mDA-Neuronen exprimiert wird. Und um zu beurteilen, ob *Bcl11a*-positive mDA-Neuronen zu mehreren bekannten Subpopulationen von mDA-Neuronen gehören, wurden immunhistochemiesche Experimente sowohl im neonatalen als auch im adulten murinen Mittelhirn durchgeführt. Um zu untersuchen, ob *Bcl11a*-exprimierende mDA-Neuronen Teil eines spezifischen Netzwerks innerhalb des dopaminergen Systems bilden, wurden intersektionales Fate Mapping, anterogrades virenvermitteltes Tracing und retrograde Tracing-Ansätze kombiniert. Um zu ermitteln, ob BCL11A für die Etablierung und/oder Aufrechterhaltung von *Bcl11*a-exprimierenden mDA-Neuronen und deren Zellschicksal notwendig ist, wurde ein konditionales Knock-out Mausmodell für Bcl11a in mDA-Neuronen erzeugt. Es wurden eine Reihe Verhaltensexperimente durchgeführt um zu untersuchen ob der Verlust von Bcl11a zu einer funktionellen Beeinträchtigung im mDA System führt. Letztendlich wurde die Anfälligkeit von Bcl11a exprimierenden mDA-Neuronen auf neurodegenerative Prozesse durch die Überexpression von α-Synuclein getestet. .

Die Ergebnisse dieser Studie zeigen, dass BCL11A in etwa einem Drittel der mDA-Neuronen in der SN, VTA und dem RRF exprimiert wird und dass *Bcl11a*-exprimierende mDA-Neurone zu mehreren bekannten Subpopulationen von mDA-Neuronen beitragen. Intersektionelle Markierungs- und Tracing-Experimente zeigen, dass *Bcl11*a-exprimierende mDA-Neurone, trotz ihrer breiten anatomischen Verteilung, einen hochspezifischen Teil des neuronalen Netzwerks innerhalb des dopaminergen Systems bilden. Die spezifische Inaktivierung von *Bcl11a* in mDA-Neuronen führte zu anatomischen Veränderungen in der Positionierung der

Bcl11a-positiven mDA-Neurone. Darüber hinaus zeigen Mäuse, denen die *Bcl11a*-Expression in mDA-Neuronen fehlt, Defizite beim motorischen Lernen, was darauf hindeutet, dass der Verlust von *Bcl11a* zu einer funktionellen Beeinträchtigung von mDA-Neuronen führt. Außerdem wurde durch eine Überexpression von α-Synuclein in mDA-Neuronen, einem Modell der Parkinson-Erkrankung, gezeigt, dass *Bcl11a*-exprimierende SN-Neurone besonders anfällig für Neurodegeneration sind. Zusätzlich erhöht der Verlust von *Bcl11a* in dieser Population ihre Anfälligkeit für eine α-Synuclein-induzierte Degeneration.

Diese Studie verbindet den entwicklungsbedingten Ursprung einer spezifischen Untergruppe von mDA-Neuronen mit ihrem Vulnerabilitätsphänotyp und ihrer funktionellen und schaltungstechnischen Spezialisierung. Somit zeigen die Ergebnisse dieser Studie, dass ein besseres Verständnis der genetisch definierten Entwicklungsgeschichte von mDA-Neuronen entscheidend ist, um die funktionelle Organisation des dopaminergen Systems und seine Anfälligkeit für Neurodegeneration im erwachsenen Gehirn zu verstehen.

1. INTRODUCTION

1.1 The midbrain dopaminergic system

1.1.1 Anatomical classification

Monoamine-containing cells of the central nervous system (CNS) distributed from the medulla oblongata to the hypothalamus have been classified in the early 1960s according to the A1-A14 nomenclature ("A" stands for aminergic) (Dahlström & Fuxe, 1964; Dahlström & Fuxe, 1965). The A1-A7 groups of cells include noradrenergic neurons located in the medulla oblongata, while the A8-A10 and A11-A14 groups consist of dopaminergic neurons of the mesencephalon and diencephalon, respectively (Dahlström & Fuxe, 1964; Dahlström & Fuxe, 1965). Later studies added three additional dopaminergic cell groups, A15-A17, located in the ventral hypothalamus, olfactory bulbs and retina (Hökfelt et al., 1984). According to this classification, midbrain dopaminergic (mDA) neurons, typically defined as neurons releasing the neurotransmitter dopamine (DA) (Lammel et al., 2008; Morales & Margolis, 2017; Roeper, 2013), are located in three main nuclei: the retrorubral field (A8, RRF), the substantia nigra (A9, SN) and the ventral tegmental area (A10, VTA) (Björklund & Dunnett, 2007a; Dahlström & Fuxe, 1964; Dahlström & Fuxe, 1965) **(Figure 1A)**. However, this anatomical classification has long been recognized as an oversimplification. In fact, more recent studies have identified different subregions within the A8-A10 dopaminergic (DA) cell groups.

The SN extends from rostral to caudal within the midbrain and can be subdivided into substantia nigra pars compacta (SNc), substantia nigra pars lateralis (SNl) and substantia nigra pars reticulata (SNr) (Nelson et al., 1996) **(Figure 1B)**. The SNr is the largest part of the SN and it contains numerous and densely packed parvalbumin-positive interneurons (Fu et al., 2012). The majority of DA neurons are located in the SNc, a smaller population forms the SNl and only a few of them can be found in the SNr. The SNc can be further subdivided into medial and lateral SNc. The RRF represents the caudal extension of the SNc (Nelson et al., 1996) **(Figure 1B)**. The VTA includes the interfascicular nucleus (IF), the parabrachial pigmented nucleus (PBP), the paranigral nucleus (PN), the caudal linear nucleus (CLi) and the rostral linear nucleus of the raphe (RLi) (Fu et al., 2012) **(Figure 1B)**. The CLi neurons are located at the caudal level of the mDA neuron complex, at the same rostrocaudal level as the RRF neurons (Nelson et al., 1996). mDA neurons can be identified by the expression of tyrosine hydroxylase (TH), the rate limiting enzyme in DA synthesis. TH catalyses the conversion of tyrosine to L-3,4-dihydroxyphenylalanine (L-DOPA), which can be, through a series of downstream enzymatic reactions, processed into the neurotransmitter DA.

A   **sagittal view**
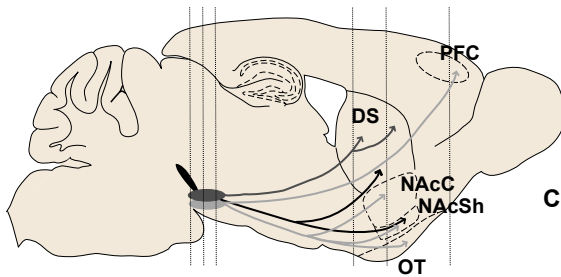
SN   (A9): mSNc + lSNc + SNl
VTA (A10): PBP + PN + IF + CLi + RLi
RRF (A8)

nigrostriatal pathway: SN → DS

mesocortical pathway: VTA → PFC

mesolimbic pathway: VTA → NAcC, NAcSh, OT
                                  RRF→ NAcSh

B   **coronal view**

ventral midbrain

Forebrain target areas

- basolateral amygdala (BLA)
- dorsolateral striatum (DLS)
- dorsomedial striatum (DMS)
- hippocampus (HIP)
- lateral habenula (LHb)
- lateral septum (LS)
- nucleus accumbens core (NAcC)
- nucleus accumbens lateral shell (lNAcSh)
- nucleus accumbens medial shell (mNAcSh)
- prefrontal cortex (PFC)
- ventral striatum
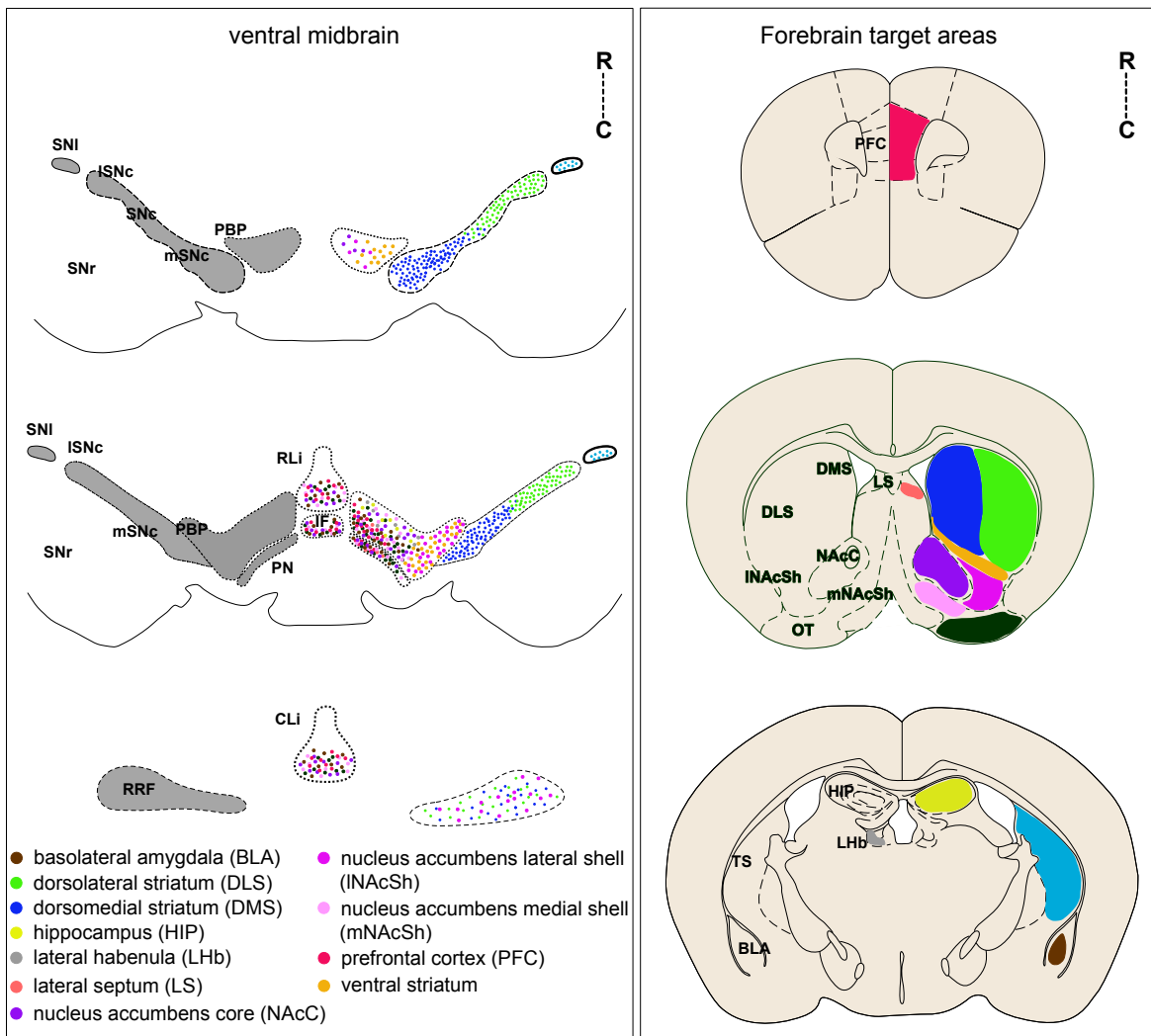
Figure 1. (Figure legend on next page)

Figure 1. mDA neurons and their projections in the adult mouse brain. (A) Schematic of a sagittal section through the adult mouse brain. mDA nuclei send projections to forebrain target areas. SN: substantia nigra; mSNc: substantia nigra pars compacta, medial; lSNc: substantia nigra pars compacta, lateral; SNl: substantia nigra pars lateralis; VTA: ventral tegmental area; PBP: parabrachial pigmented nucleus; PN: paranigral nucleus; IF: interfascicular nucleus; CLi: caudal linear nucleus; RLi: rostral linear nucleus of the raphe; RRF: retrorubral field; DS: dorsal striatum: OT: olfactory tubercle; NAcC: nucleus accumbens core; NAcSh: nucleus accumbens shell; PFC: prefrontal cortex. Lines indicate the rostrocaudal levels of the forebrain target areas and ventral midbrain coronal sections shown in B. **(B)** Schematic of coronal rostrocaudal levels of the midbrain showing the anatomical organization of SNc, VTA and RRF (left panel). Differently coloured dots represent the cell body location of mDA neurons projecting to corresponding forebrain targets (labelled with the same colour, right panel).

1.2 mDA neuron diversity

The distinct projection patterns of mDA neurons and their impacts on DA-modulated behaviour shows that this neuronal population is very heterogeneous **(see Figure 1)**. In addition, mDA neurons are characterized by distinct synaptic connectivity (inputs onto DA neurons), electrophysiological properties and ability of co-release of neurotransmitters other than dopamine, molecular profiles, and vulnerability to neurodegeneration.

In this section, mDA neuron diversity at these different levels will be discussed.

1.2.1 mDA neuron projections and functions

mDA neurons of the SN and VTA project to distinct forebrain target areas and modulate different aspects of behaviour (Lammel et al., 2008; Lammel et al., 2012; Lammel et al., 2014). The SNc mDA neurons are thought to project to the striatum (nigrostriatal pathway), regulating voluntary movement and action selection. Their degeneration results in the major motor symptoms of Parkinson´s disease (PD) (Bentivoglio & Morelli, 2005; Björklund & Dunnett, 2007a; Roeper, 2013) **(Figure 1A)**. Moreover, mDA neurons of the rostromedial SNc send their axons to the posterior dorsomedial striatum (pDMS) and regulate explorative behaviour (Roeper, 2013). Recent studies have introduced a new subdivision of the SNc into a medial and a lateral part according to projection targets and functional outputs. Medial SNc (mSNc) mDA neurons project to the dorsomedial striatum (DMS) and their firing may signal the valence of the outcome (Lerner et al., 2015). Lateral SNc (lSNc) mDA neurons send their projections to the dorsolateral striatum (DLS) and their firing may signal a salience signal (appetitive or aversive) (Lerner et al., 2015). mDA neurons located in the SNl project to the posterior tail of the striatum (TS) and have been shown to reinforce avoidance of threatening stimuli (Menegas et al., 2015; Menegas et al., 2018) **(Figure 1B)**.

Unlike the SN, there is no clear relationship between the anatomical location of mDA cell bodies in the different subgroups of the VTA and their projection targets (Morales & Margolis, 2017). Early studies suggested that VTA mDA neurons send their projections to limbic and

cortical target areas through the mesolimbic and mesocortical pathways (Björklund & Dunnett, 2007a; Fallon & Moore, 1978; Lammel et al., 2008; Lindvall et al., 1977; Lindvall & Björklund, 1974) **(Figure 1A)**. However, most recent studies have shown that anteromedial and ventral parts of the striatum derive their innervation from the lateral part of the VTA as well. Thus, VTA mDA neurons contribute to striatal projections via the mesostriatal pathway, a more convenient term to be used to include every component of the DA system projecting to the striatum (Björklund & Dunnett, 2007a). The main VTA mDA neurons projection targets are the medial prefrontal cortex (mPFC), the basolateral amygdala (BLA) and the core and shell of the nucleus NAc (NAcC and NAcSh, respectively) and the olfactory tubercles (OT). NAc and OT are both part of the ventral striatum (Björklund & Dunnett, 2007a) **(Figure 1A)**. VTA mDA neurons project also to other limbic-related regions such as lateral septum (LS), lateral habenula (LHB) and hippocampus (HIP) (Antonopoulos et al., 1997; Gasbarri et al., 1994; Stamatakis et al., 2013; Swanson, 1982). DA projections to the mPFC, BLA, NAcC and NAc medial shell and to the medial and lateral OT arise from mDA neurons of the medial posterior VTA, with their cell bodies located in the medial PN nucleus, the medioventral part of the PBP nucleus and in a smaller portion in the adjacent IF nucleus (Ikemoto, 2007; Lammel et al., 2008). In contrast, mDA neurons located in the lateral PBP nucleus send their projections to the NAc lateral shell **(Figure 1B)**. mDA neurons projecting to all of the above mentioned projection targets areas, with the exception of the lateral shell, are found also in the RLi and CLi nuclei (Ikemoto, 2007; Lammel et al., 2008) **(Figure 1B)**. mDA neurons of the VTA mediate reward-related and goal-directed behaviours, working memory, attention, decision making, incentive salience, stimulus salience and aversion (Morales & Margolis, 2017). Dysfunctions within the mesocorticolymbic system have been associated with depression, attention deficit/hyperactivity disorder, addiction and schizophrenia (Chenu et al., 2009; Dailly et al., 2004; Sulzer, 2007; Winterer & Weinberger, 2004; Wise, 2009). Several studies have shown that mDA neurons of the VTA are involved in different reward prediction behaviours. Some VTA- mDA neurons are activated in response to an unpredicted reward, shift their activation to reward-predicting cues following learning and transiently decrease their activity when an expected reward is omitted. Moreover, VTA-mDA neurons can be also excited or inhibited by aversive stimuli or by cues that predict an aversive outcome (Cohen et al., 2012; Matsumoto & Hikosaka, 2009; Morales & Margolis, 2017; Schultz, 1997).

Based on optogenetic-based dissection of neuronal circuits it has been suggested that different subpopulation of VTA mDA neurons mediate different functions and are therefore associated with distinct neuronal networks (Morales & Margolis, 2017). In fact, several studies revealed various subcircuits regulating particular behaviours. Chaudhury and colleagues showed that mDA neurons can rapidly regulate depression-related behaviours. Specifically, phasic activation of VTA mDA neurons projecting to the NAc induced susceptibility to social

defeat stress while their inhibition induced resilience. On the other hand, optogenetic inhibition of mPFC-projecting VTA neurons promoted susceptibility (Chaudhury et al., 2013). Another study from Gunaydin and colleagues revealed that activity of a VTA-to-NAc projection encodes and predicts key features of social interaction and that optogenetic control of these neurons was sufficient to modulate social behaviour (Gunaydin et al., 2014). Moreover, a specific circuit involving inputs from the anterior cortex to VTA mDA neurons and their output to the lateral NAc shell is believed to be reinforcing (Beier et al., 2015). In a more recent study Edwards and colleagues found that GABAergic inputs from the NAc to the VTA regulated cocaine-induced locomotion (Edwards et al., 2017). It has also been shown that DA terminals in the ventral NAc medial shell are excited by unexpected aversive outcomes and to cues that predict them, and that mDA neurons sending these projections receive afferents from glutamatergic neurons in the lateral hypothalamus that provide information about aversive outcomes (de Jong et al., 2019). mDA neurons located in the RRF are contributing to the mesostriatal pathway and some of them send projections to the NAc lateral shell (Deutch et al., 1988; Lammel et al., 2008). However, their impact on behaviour has not yet been elucidated.

1.2.2 mDA neurons input/output relationships

An extensive anatomical map of neuronal connections is the foundation for understanding neuronal circuit function. Recent studies using Cre-based cell-type-specific targeting, axon-initiated viral transduction with rabies mediated trans-synaptic tracing, optogenetics, photo-tagging and fibre photometry made it possible to map input-output relationship of mDA neurons (Beier et al., 2015; Beier et al., 2019b; Lammel et al., 2012; Lerner et al., 2015; Menegas et al., 2015; Tian et al., 2016; Watabe-Uchida et al., 2012b).

SNc mDA neurons receive monosynaptic inputs from the somatosensory and motor cortex and from the subthalamic nucleus (Watabe-Uchida et al., 2012). Moreover, the DMS and DLS are preferentially reciprocally connected with the same SNc mDA neurons that project back to these striatal areas. Strong DLS projections to DMS projecting SNc mDA neurons were also found, suggesting a new route of lateral to medial information flow (Lerner et al., 2015). Of note, DLS inputs are an order of magnitude stronger that inputs from the DMS (Lerner et al., 2015). SNc mDA neurons projecting to the posterior striatum constitute a unique class of mDA neurons regulated by different inputs. In fact, these neurons receive relatively few inputs from the ventral striatum and instead receive more inputs from the globus pallidus, subthalamic nucleus and zona incerta (Menegas et al., 2015) **(Table 1A)**. VTA mDA neurons projecting to the NAc lateral shell are receiving inputs from laterodorsal tegmentum neurons while those projecting to the mPFC receive inputs from neurons located in the lateral habenula

(Lammel et al., 2012). Moreover, Watabe-Uchida and colleagues identified monosynaptic inputs onto VTA mDA neurons originating from the lateral hypothalamus (Watabe-Uchida et al., 2012). Input/output relationships of VTA mDA neurons were also mapped by Beier and colleagues in two different studies. In their 2015 study they could demonstrate that VTA mDA neurons projecting to the medial and lateral NAc represent two discrete population with distinct targets and receive differential inputs. VTA mDA neurons sending their projections to the medial NAc receive input preferentially from the dorsal raphe, while those projecting to the lateral NAc receive input from the anterior cortex and striatal regions (Beier et al., 2015). In a more recent study, Beier and colleagues further dissected the connectivity in the VTA by defining input/output relations of neurochemically and output-defined neuronal population and found that the output site correlates with whole-brain inputs, rather than neurochemical phenotype (e.g. vesicular glutamate transporter 2 (VGLUT2)-expressing, glutamate decarboxylase 2 (GAD2)-expressing or DA neurons within the VTA) (Beier et al., 2019) **(Table 1A)**.

Although the above-mentioned circuit-mapping studies have provided a large amount of information on the input-output relationship of mDA neurons, additional *in vivo* complementary methods are required to elucidate the role of distinct SN- and VTA-mDA neurons in network dynamics.

1.2.3 mDA neuron electrophysiological profiles

Several studies that combined retrograde tracing with standard whole-cell and perforated-patch clamp recordings have provided some insights on the basic electrophysiological properties of mDA neurons based on their projection targets (Ford, 2006; Lammel et al., 2008; Liss et al., 2005; Margolis et al., 2008; Tarfa et al., 2017). A spontaneous pacemaker activity, broad action potentials (APs) and the presence of hyperpolarization-activated current (I_H)-mediated sag components have been for a long time considered to be the typical electrophysiological properties of mDA neurons (Liss et al., 2005; Margolis et al., 2006; Neuhoff et al., 2002). These criteria for identifying mDA neurons were originally established by recordings from mDA neurons in the SNc. However, electrophysiological differences in I_H current amplitudes, sag and maximal firing rates were found in mDA neurons. These differences were associated with distinct projections to dorsal or ventral striatal target areas (Liss et al., 2005). Lammel and colleagues identified two highly distinct functional phenotypes within the mDA system. Mesostriatal SNc mDA neurons discharge in a slow regular pacemaker mode and exhibit a typical low threshold, broad APs and a prominent afterhyperpolarization. Upon injection of hyperpolarizing currents of increasing amplitudes they develop the typical sag components, that has been routinely used to functionally identify

mDA neurons (Lammel et al., 2008) **(Table 1B)**. Mesocortical VTA mDA neurons projecting to mPFC, BLA, NAc core and NAc medial shell possess highly distinct properties. The durations of the APs are longer than those of mesostriatal mDA neurons and their spontaneous discharge frequencies were in most cases higher. Furthermore, they do not develop any obvious sag components upon injection of hyperpolarizing currents of increasing amplitudes, suggesting a lack of functional I_H currents. These neurons show instead a prominent rebound inhibition with a slow return to the firing threshold (Lammel et al., 2008) **(Table 1B)**. However, later studies have shown that these longer delays to spiking after hyperpolarization are the result of the interplay between an I_H of smaller amplitude compared to SNc mDA neurons and an A-type potassium current (I_A) (Tarfa et al., 2017). Mesocortical mDA neurons show higher maximal discharge frequencies in the range of 20-30 Hz, while mesostriatal mDA neurons show a discharge with an upper limit of 10 Hz. Interestingly, VTA mDA neurons projecting to the NAc lateral shell do not show the unconventional functional properties of the above described mesocortical neurons, but instead possess the classical phenotype of mesostriatal mDA neurons (Lammel et al., 2008) **(Figure 2B)**.

1.2.4 Co-release of neurotransmitters

Different subpopulations of mDA neurons from the SN and VTA have been shown to be able to co-release other neurotransmitters together with DA (Cai et al., 2021; Cai & Ford, 2018; Chuhma et al., 2018; Kim et al., 2015; Morales & Margolis, 2017; Poulin et al., 2018; Tritsch et al., 2012; Zhang et al., 2015).

Several studies have demonstrated that γ-aminobutyric acid (GABA), the main inhibitory neurotransmitter, can be co-released by SNc-mDA neurons (Cai et al., 2021; Cai & Ford, 2018; Kim et al., 2015; Tritsch et al., 2012) **(Table 1C)**.GABA is co-released directly from SNc DA axons into the striatum, where it rapidly inhibits action potential firing in striatal projection neurons (Tritsch et al., 2012). Its co-release does not require the activity of the vesicular GABA transporter (VGAT), but instead GABA is co-packaged with DA in mDA neurons by the vesicular monoamine transporter 2 (VMAT2), which is the vesicular transporter for DA (Tritsch et al., 2012). Moreover, GABA co-release in SNc-mDA neurons does not use the conventional GABA-synthesizing enzymes (GAD65 and GAD67), but instead an evolutionary conserved GABA synthesis pathway mediated by aldehyde dehydrogenase 1a1 (ADLH1A1) (Kim et al., 2015). SNc-mDA neurons are also able to co-release glutamate, the main excitatory neurotransmitter (Cai et al., 2021; Cai & Ford, 2018). **(Table 1C)**. Cai and Ford have shown that glutamate co-released from SNc-mDA neurons regulates DLS cholinergic interneurons via the activation of a group I metabotropic glutamate receptors-mediated excitatory conductance (Cai & Ford, 2018). This finding was confirmed by Chuhma and colleagues with

the use of optogenetics experiments (Chuhma et al., 2018). Moreover, a recent study using a viral intersectional labelling strategy uncovered a subpopulation of Vglut2-expressing DA neurons of the lateral SNc that projects to the TS (Poulin et al., 2018). However, the functional impact of glutamate release from this subpopulation has not yet been elucidated.

mDA neuron diversity

(A) Input/output relationships	
SN	**VTA**
• SNc mDA projecting to DMS: inputs from DMS, but also DLS (Lerner et al., 2015) • SNc mDA projecting to DLS: inputs from DLS (Lerner et al., 2015) • SNc mDA projecting to the posterior striatum: inputs from globus pallidus, subthalamic nucleus and zona incerta (Lerner et al., 2015)	• VTA mDA projecting to NAc lateral shell: inputs from laterodorsal tegmentum (Lammel et al., 2012) • VTA mDA projecting to mPFC: inputs from lateral habenula (Lammel et al., 2012) • VTA mDA neurons projecting to the medial NAc: inputs from the dorsal raphe (Beier et al., 2015) • VTA mDA neurons projecting to the lateral NAc: inputs from the anterior cortex and striatal regions (Beier et al., 2015)
(B) Electrophysiological profiles	
SN	**VTA**
• Slow pacemaker AP firing rate (max 10 Hz) • Low threshold • Broad AP • Prominent AHP • Typical I_H-mediated sag component (Lammel et al., 2008)	• High spontaneous AP firing rate (20-30 Hz) • Smaller AP amplitude and longer duration compared to SN mDA • No obvious sag and I_H • Prominent rebound inhibition (Lammel et al., 2008)
(C) Co-release of neurotransmitters	
SN	**VTA**
• DA and GABA (Cai et al., 2021; Cai & Ford, 2018; Kim et al., 2015; Tritsch et al., 2012) • DA and glutamate (Cai et al., 2021; Cai & Ford, 2018; Chuhma et al., 2018; Silm et al., 2019)	• DA and glutamate (Hnasko et al., 2010; Morales & Margolis, 2017; Stuber et al., 2010; Zhang et al., 2015)
(D) Gene expression profiles	
SN	**VTA**

• Poulin et al., 2014, two subtypes:
  ○ DA¹ᴬ (high expression of *Aldh1a1, Sox6* and *Ndnf*), ventral tier of the SNc
  ○ DA¹ᴮ (lack of *Aldh1a1* expression), dorsal SNc
 	
• La Manno et al., 2016, one subtype:
  ○ mDA-SNC *(high expression of Aldh1a1 and Sox6 and low expression of Calb1)*, SNc
 	
• Tiklová et al., 2019, one subtype:
  ○ *AT-Dat^{high}* (*Aldh1a1* expression), SNc
	• Poulin et al., 2014, three subtypes:
	  ○ DA²ᴬ (high expression of *Vgat,* low expression of *Satb1, Gsg1l* and *Clstn2*), intermingled throughout the VTA
	  ○ DA²ᴮ (co-expression of *Lpl, Adcyap1, Otx2* and *Aldh1a*) ventromedial VTA and IF
	  ○ DA²ᴰ (unique expression of *Vip*), PAG and DR
	
	• La Manno et al., 2016, four subtypes:
	  ○ mDA-VTA1,2 *(high expression of Aldh1a1 and Sox6 and low expression of Calb1)*, ventral and lateral VTA
	  ○ mDA-VTA 3 (*Vip* expression), PAG
	  ○ mDA-VTA 4 (high expression of *Calb1*), throughout the VTA
	
	• Tiklová et al., 2019, four subtypes:
	  ○ *T-Dat^{high}* (co-expressing *TH* and *DAT,* but not *Aldh1a1*), mainly PBP
	  ○ *VT-Dat^{high}* (*Vip* expression), PAG
	  ○ *GT-Dat^{low}* (*Vgat* expression), PBP
	  ○ *NT-Dat^{low}* (co-expression of *Nxph4* and *TH*), not localised in the mouse brain

(E) Vulnerability to neurodegeneration	
SN	**VTA**
• Aldh1a1 positive SNc mDA neurons of the ventral tier are more vulnerable to degeneration • Calbindin positive SNc mDA neurons of the dorsal tier are less vulnerable to degeneration (Di Salvio et al., 2010; Liang et al., 1996; Liu et al., 2014; Poulin et al., 2014)	• VTA mDA neurons are much less affected by neurodegeneration in PD (German et al., 1996)

Table 1. mDA neuron diversity in the adult mouse brain. This table summarizes the diversity of SN- and VTA-mDA neurons in terms of input/output relationships **(A)**, electrophysiological properties **(B)**, co-release of neurotransmitters **(C)**, gene expression profiles **(D)** and their vulnerability to neurodegeneration **(E)**.

Several studies reported VTA-mDA neurons co-releasing DA and glutamate (Morales & Margolis, 2017) **(Table 1C)**.The majority of neurons co-expressing TH and VGLUT2 are located in the midline nuclei of the VTA. However, some of them do not express VMAT2 or the dopamine transporter DAT, which are required for DA vesicular packaging and uptake (Li et al., 2013). For these neurons, co-release of glutamate and DA has been demonstrated in studies using electrophysiology on acute brain slices and voltammetry (Stuber et al., 2010; Zhang et al., 2015). The proposed mechanism for the release of DA and glutamate by the Vglut2 and TH expressing neurons differ depending on the studies and experimental methods used (Morales & Margolis, 2017). Hnasko and colleagues suggested the accumulation and co-release of DA and glutamate from the same pool of vesicles based on in vitro studies in which VGLUT2 and VMAT2 could be co-immunoprecipitated in striatal preparations enriched for synaptic vesicles (Hnasko et al., 2010). However, Zhang and colleagues could not confirm the vesicular coexistence of VMAT2 and VGLUT2 in purified vesicles from the NAc. Instead, using optogenetics they found that DA and glutamate are released from the same mesoaccumbens fibres but not at the same site or from the same synaptic vesicles (Zhang et al., 2015). Moreover, a recent study from Silm and colleagues shows that the release mechanisms for DA and glutamate from mDA neurons show different properties, reflecting storage in different synaptic vesicles (Silm et al., 2019).

1.2.5 Gene expression profiles

In addition to the anatomical mDA subgroups (see section 1.1.1), mDA neurons have been defined based on their molecular profile (Poulin et al., 2020). In the last decade, single cell transcriptomics and bioinformatic approaches allowed to detect coordinated gene-expression profiles within individual cells. These techniques have been used to classify mDA neurons based on gene expression and revealed the presence of different molecularly-defined mDA subgroups. These subgroups do not necessarily correspond to mDA populations distinct by anatomical location, projections and functional output (Hook et al., 2018; Kramer et al., 2018; La Manno et al., 2016; Poulin et al., 2014; Poulin et al., 2020; Saunders et al., 2018; Tiklová et al., 2019).
Poulin and colleagues used a single-cell gene-profiling approach to identify different molecularly distinct mDA neurons subtypes. Subsequently, they localized them in the adult mouse brain by combining immunofluorescence, fluorescent in situ hybridization (FISH) and transgenic mouse lines (Poulin et al., 2014). In this study, single mDA neurons expressing the fluorescent protein tdTomato were isolated from the midbrain of postnatal day 4 (P4) *Slc6a3 (*also known as *DAT)::Cre , Ai9* mice. Subsequently, they were FACS sorted and analysed for the expression of 96 candidate genes based on previously reported differential expression

between SNc and VTA (Chung et al., 2005; Greene et al., 2005; Grimm et al., 2004). By using multiplexed quantitative polymerase chain reaction (qPCR) followed by an unbiased coefficient similarity hierarchical clustering analysis to parcel these cells according to their gene-expression profile, Poulin and colleagues identified two main clusters of cells. The first cluster has more similarity to the molecular signature of SNc-mDA neurons and can be subdivided into two subtypes named DA^{1A} and DA^{1B}. The second cluster has an expression profile related to the VTA and can be further subdivided into four molecular subtypes named DA^{2A}, DA^{2B}, DA^{2C} and DA^{2D} (Poulin et al., 2014). The DA^{1A} subtype is the only one with high expression of *Aldh1a1* (Aldehyde Dehydrogenase 1 Family Member A1), *Sox6* and *Ndnf* and low expression of *Foxa2* and *Lmx1a* and is located in the ventral tier of the SNc. The DA^{1B} cluster has a similar expression profile to DA^{1A} but lacks *Aldh1a1* expression and is located in the dorsal part of the SNc and intermingled with other subtypes in the rostro-dorsal VTA. The DA^{2A} cluster shows high expression of *Slc32a1* (also known as *Vgat*) but low expression of *Satb1*, *Gsg1l* and *Clstn2*. These neurons were found to be intermingled with other DA subtypes throughout the VTA. The DA^{2B} cluster is defined by the unique co-expression of *Lpl*, *Adcyap1*, *Otx2* and *Aldh1a1* and these cells are located mainly in the ventromedial VTA and IF. No distinctive marker could be identified for the DA^{2C} cluster, which shows high levels of *Calb1*, *Cck*, and *Slc17a6*. Finally, the DA^{2D} cluster is defined by the unique expression of *Vip* combined with low expression of *Snca*, *Chrna4*, and *Ntf3.* These cells are located in the periaqueductal gray (PAG) and dorsal raphe (Poulin et al., 2014) **(Table 1D)**.

La Manno and colleagues confirmed the presence of five types of mDA neurons in a separate single-cell RNAseq analysis of adult mouse mDA neurons, using again a *Slc6a3 ::Cre , Ai9* mouse line (La Manno et al., 2016). They identified one cell type mapped to the SNc (mDA-SNC), three to the VTA (mDA-VTA 1,2 and 4) and one to the PAG (mDA-VTA 3). High expression of genes such as *Aldh1a1* and *Sox6* and low expression of *Calb1* were found in mDA-SNC, mDA-VTA1 and mDA-VTA2 neurons. mDA-VTA3 neurons are characterized by Vip expression (La Manno et al., 2016) **(Table 1D)**.

In a more recent study Tiklová and colleagues used single cell RNAseq of isolated mouse neurons expressing the transcription factor *Pitx3* (*Pitx3^{EGFP}* mouse line), a marker for mDA neurons, followed by unsupervised clustering analysis and identified seven neuronal subgroups divided into two major branches of developing Pitx3-expressing neurons (Tiklová et al., 2019). Two of them express GABAergic and glutamatergic markers, while five of them express DA markers. The subgroups expressing DA markers were divided into two groups based on the expression level of the *Slc6a3* gene: *Dat^{high}* and *Dat^{low}*. The *Dat^{high}* group is further subdivided into three clusters: *AT-Dat^{high}*, *T-Dat^{high}* and *VT-Dat^{high}*. The *Dat^{low}* group is further subdivided into *N-Dat ^{low}*, NT-*Dat ^{low}, G-Dat ^{low}* and *GT-Dat ^{low}*. N-*Dat ^{low}* and *G-Dat ^{low}* subtypes were not expressing TH and could be glutamatergic and GABAergic cells, respectively. The

localization of the different clusters in the adult mouse brain was then determined by combining FISH with immunohistochemistry for distinguishing markers. *AT-Dat^(high)* neurons co-expressing *TH* and *Aldh1a1* are located mainly in the SNc, confirming the findings by La Manno and Poulin (La Manno et al., 2016; Poulin et al., 2014, 2020; Tiklová et al., 2019). *T-Dat^(high)* cells positive for *Dat* and *TH* but showing no expressions of *Aldh1a1* are mainly located in the PBP nucleus and some of them are also found in the medial VTA. These mDA neurons share the *Sncg* expression with the *AT-Dat^(high)* group and could correspond to the DA[1B] subgroup and mDA-VTA1 subpopulation identified by La Manno and Poulin, respectively (La Manno et al., 2016; Poulin et al., 2014; Tiklová et al., 2019). Neurons of the *VT-Dat^(high)* group are co-expressing *Vip* and *TH* and are mainly situated within the PAG and most likely correspond to the DA[2D] and mDA-VTA3 groups described by La Manno and Poulin, respectively (La Manno et al., 2016; Poulin et al., 2014; Poulin et al., 2020; Tiklová et al., 2019). The *GT-Dat ^(low)* cells co-express *Pitx3* and *Vgat* and are found only in the PBP nucleus of the VTA. These neurons might correspond to the DA[2A] and mDA-VTA4 groups identified by La Manno and Poulin, respectively (La Manno et al., 2016; Poulin et al., 2014; Poulin et al., 2020; Tiklová et al., 2019). Although the NT-*Dat ^(low)* group co-expressing *Nxph4* and *TH* was found in this study, the authors could not identify this group within the adult mouse midbrain (Tiklová et al., 2019) **(Table 1D)**.

The molecular heterogeneity within the mouse DA system has been investigated by at least three more independent studies, with the attempt to classify mDA neurons based on their gene expression profiles (Hook et al., 2018; Kramer et al., 2018; Saunders et al., 2018). Although these and the studies described above used different experimental parameters and analysis methods, they identified at least seven partially overlapping mDA subtypes (Poulin et al., 2020). Some of these mDA neurons subtypes are located in a manner independent from the traditional anatomical classification (see section 1.1.1). Interestingly, a more recent study from Phillips and colleagues based on single nucleus RNA-sequencing on rat VTA cells identified sixteen transcriptionally distinct cell types within the VTA, including seven neuronal subpopulations. Further sub-clustering of VTA neuronal cells revealed populations of combinatorial neurons expressing markers for more than one neurotransmitter system (Phillips et al., 2021).

1.2.6 mDA neuron vulnerability to neurodegeneration

SNc-mDA neurons degenerate in PD, leading to the cardinal motor symptoms of the disease. VTA-mDA neurons are much less affected by neurodegeneration in PD (German et al., 1996) **(Table 1E)**. However, SNc-mDA neurons are not homogeneous in their vulnerability: SNc-mDA neurons in the ventral tier are more vulnerable than the ones located in the dorsal tier.

This selective vulnerability has been found in both humans and various PD models in rodents (Damier et al., 1999; Kordower et al., 2013). In mouse, the more vulnerable population has been shown to express ALDH1A1 (G. Liu et al., 2014; Poulin et al., 2014) **(Table 1E)**. Poulin and colleagues evaluated the susceptibility of DA[1A] neurons showing high expression of *Aldh1a1* (see section 1.2.4) to the neurotoxin MPTP (1-methyl-4-phenyl-1,2,3,6-tetrahydropyridine) that has been widely used to induce parkinsonism in mice (Poulin et al., 2014). They found that DA[1A] neurons were significantly more vulnerable to neurodegeneration, since a 66.2% diminution of *Aldh1a1* positive cells occurred in the SNc of MPTP treated mice. The remaining mDA neurons in the SNc were significantly less affected by MPTP. In comparison, the DA[2B] subtype co-expressing *Aldh1a1* and *Otx2* in the ventromedial VTA was not differentially affected by MPTP when compared to other mDA subpopulations (Poulin et al., 2014). In a study from the same year, Liu and colleagues showed that, in α-synuclein transgenic mice, a mouse model of PD, neurodegeneration occurs mainly in a dorsomedial SNc subpopulation negative for *Aldh1a1*, suggesting that ALDH1A1 may exert a protective function against degeneration (G. Liu et al., 2014)*.* In fact, genetic inactivation of *Aldh1a1* enhanced the overall degeneration of SNc-mDA neurons, whereas its overexpression appeared to preferentially protect against α-synuclein mediated mDA neurons degeneration. Since loss of ALDH1A1 function makes SNc-mDA neurons even more prone to neurodegeneration, ALDH1A1 seems unlikely to be the functionally decisive factor in the increased vulnerability (Liu et al., 2014). In mouse, the less vulnerable subpopulation expresses the calcium-binding protein Calbindin1 (CALB1) (Di Salvio et al., 2010; Liang et al., 1996; G. Liu et al., 2014; Poulin et al., 2014) **(Table 1E).** Liang and colleagues showed that CALB1 plays a neuroprotective role against mDA neurodegeneration in MPTP-treated mice (Liang et al., 1996). Taken together, these insights suggest that susceptibility to neurodegeneration in mDA subgroups could be genetically and developmentally pre-determined (Schwamborn, 2018).

1.2.7 mDA neuron subsets establishment

It is not clear to what extent these different levels of diversity described above can be reduced to a common denominator to define mDA diversity. Since anatomical position, molecular profile and connectivity are largely determined during development, a better understanding of the developmental factors that determine mDA subpopulations could deliver important new insights on how to define mDA subpopulations.

The mechanisms and transcription factors that control the generation of mDA fate during development have been extensively described (Alves dos Santos & Smidt, 2011; Ang, 2006; Arenas et al., 2015; Blaess & Ang, 2015; Bodea et al., 2014; Smidt & Burbach, 2007), but very

little is known on how mDA neurons subsets are established. Growing evidence suggests that diversity in the mDA system starts to emerge during development. In the upcoming section, the developmental mechanisms that determine the mDA fate and mDA neurons diversification will be briefly summarised.

1.3 mDA neuron development

1.3.1 Generation of dopaminergic fate

mDA neurons are generated from a progenitor zone in the ventral midline of the midbrain. Around embryonic day (E) 8 of murine development the induction of the floor plate by sonic hedgehog (SHH) begins. With the onset of LIM homeodomain transcription factor 1A (LMX1A) expression at E9, the mDA progenitor domain emerges in the ventral midline (Andersson et al., 2006; Arenas et al., 2015; Blaess & Ang, 2015) **(Figure 2)**. Subsequently, around E10.5, the neurogenesis of mDA neurons starts and it is characterised by the expression of the proneural gene Neurogenin 2 (NEUROG2) and of TH (Andersson et al., 2006; Dumas & Wallén-Mackenzie, 2019; Kele, 2006). mDA neurons start to differentiate around E11.5 and are characterized by the expression of the transcription factor NURR1 **(Figure 2)**. mDA neuron differentiation continues until E14.5, and differentiated mDA neurons simultaneously migrate, form projections and establish synaptic contacts with neurons located in their forebrain target areas **(Figure 2)**. Each stage in mDA development, from the specification of mDA precursors from floor plate cells to their differentiation into mDA neurons, is characterized by the expression of several transcription factors and other molecular markers (reviewed in (Arenas et al., 2015; Blaess & Ang, 2015)).
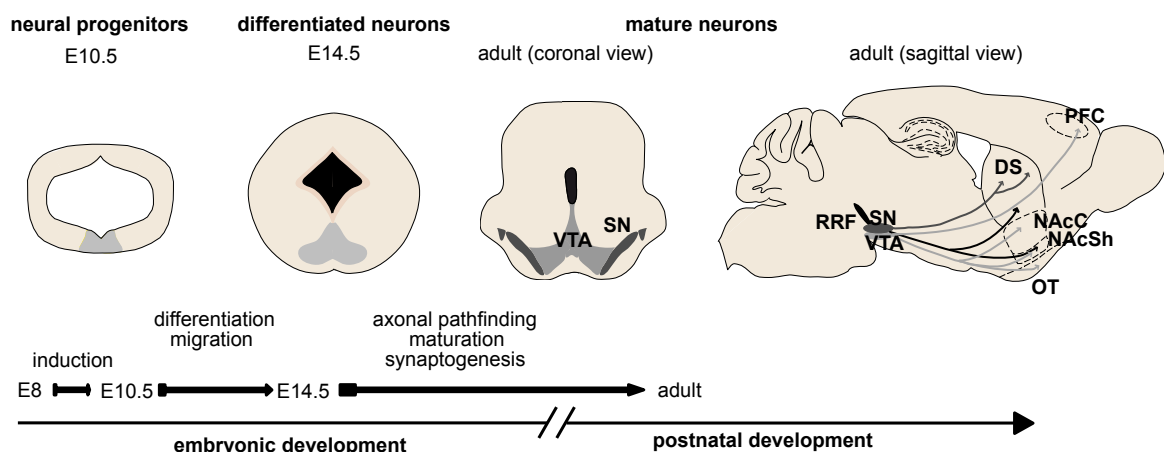
Figure 2. Timeline of mDA neuron development in the mouse. mDA progenitors are induced in the ventral midline of the midbrain. Afterwards, they differentiate and mature. Differentiated mDA neurons migrate, form projections and establish synaptic contacts with neurons in their forebrain targets areas.

1.3.2 Diversity in dopaminergic progenitors

mDA neuron diversity has been shown to be partially specified in mDA progenitors. mDA progenitors are divided into medial and lateral progenitors based on the time when they express *Shh* and *Gli1* (in response to SHH signalling) and are characterized by different expression profiles of the transcription factors SOX6, OTX2 and ZFP503 (also known as NOLZ1) (Blaess et al., 2011; Hayes et al., 2011; Joksimovic et al., 2009; Panman et al., 2014). Different research groups made use of the temporal dynamic expression of *Shh* to conduct genetic inducible fate mapping studies using Shh^{CreER} or Gli1^{CreER} mouse lines in combination with reporter alleles (Blaess et al., 2011; Hayes et al., 2011; Joksimovic et al., 2009). These studies provide evidence that medial mDA progenitors express *Gli1* from E7.5 to E8.5 and *Shh* from E8.5 to E10.5. Both *Gli1* and *Shh* expression is delayed by about one day in the lateral domain (Blaess et al., 2011; Hayes et al., 2011; Joksimovic et al., 2009). In a different study, Panman and colleagues showed that mDA neuron progenitors are organized in molecularly distinct medial (Sox6^{+}/Otx2^{weak}/Nolz1^{-}) and lateral (Sox6^{-}/Otx2^{strong}/Nolz1^{+}) domains. The medial and lateral progenitors give rise to different subsets of mDA neurons, in both the developing and adult brain. mDA progenitors from the medial domain give preferentially rise to mDA neurons located in the SNc and dorsolateral VTA, while lateral mDA progenitors generate predominantly mDA neurons located in the ventromedial VTA (Blaess et al., 2011; Hayes et al., 2011). In differentiating and mature mDA neurons SOX6 is selectively expressed in SNc mDA neurons and in mDA neurons of the dorsolateral VTA, while OTX2 and NOLZ1 are expressed in a subset of VTA mDA neurons (Panman et al., 2014).

A few transcription factors have been identified that are expressed in mDA subpopulations during development and/or in the adult brain. Of these, only some have been shown to directly influence the subtype fate of differentiated mDA neurons (Di Salvio et al., 2010; Panman et al., 2014). Using loss- and gain-of-function mouse models, Di Salvio and colleagues found that the transcription factor Otx2 controls neuron subtype identity by antagonizing molecular and functional features of dorsal-lateral VTA (Di Salvio et al., 2010).

The developmental logic underlying the functional organization of the mDA system is still not clear. Since transcription factors are key regulators of cell specification programs, one hypothesis is that during development distinct mDA neurons subtypes express distinct transcription factors that ultimately regulate their molecular make-up, their projection targets and ultimately their function. The current study shows that the C2H2 zinc finger transcription factor BCL11A (B cell CLL/lymphoma) is expressed in subpopulations of mDA neurons in the developing and adult brain (see section 4.1). However, the function of BCL11A in development

and maintenance of the mDA system has not been examined. In the next section, the role of this transcription factor in human and in murine CNS development will be covered.

1.4 The transcription factor BCL11A

BCL11A (B cell CLL/lymphoma 11a), also known as CTIP1 (Chicken ovalbumin upstream promoter transcription factor-interacting proteins 1), was first identified for its function in the immune system as a proto-oncogene (Satterwhite et al., 2001). BCL11A is a transcriptional repressor and a dedicated subunit of the mammalian SWI/SNF complex, a polymorphic assembly of at least 14 subunits (encoded by 28 genes) that functions as an ATP-dependent chromatin remodeler (Kadoch et al., 2013; Simon et al., 2020).

1.4.1 BCL11A protein isoforms

The *BCL11A/Bcl11a* gene encodes for a Krüppel-like sequence-specific C2H2 zinc finger transcription factor located on human chromosome 2 or murine chromosome 11 and shows a high level of conservation across a wide range of species (H. Liu et al., 2006; Nakamura et al., 2000; Satterwhite et al., 2001). In addition to the DNA-binding C2H2 zinc finger domain located in exon 4, the BCL11A protein contains a C2HC finger motif and a nucleosome remodelling and deacetylase (NuRD) interacting domain, both located at its N- terminus (Liu et al., 2006; Simon et al., 2020) **(Figure 3A)**. It has been suggested that the C2HC motif could mediate homodimerization and nuclear translocation thus allowing the transcriptional regulation of target genes, although no data are available so far (Simon et al., 2020).

Bcl11a mRNA might be alternatively spliced, resulting in four different protein isoforms of mouse and human BCL11A (Simon et al., 2020). The resulting proteins are named BCL11A-XS (mouse, 191aa; human, 142aa), BCL11A-S (mouse and human, 243aa), BCL11A-L (mouse and human, 773aa) and BCL11A-XL (mouse and human, 835aa) (Liu et al., 2006; Satterwhite et al., 2001). Exons 1 and 2 contain the NuRD interacting and C2HC zinc-fingers domains, respectively. These domains are common to all BCL11A isoforms, except the mouse Bcl11a-XS isoforms that lacks both motifs. Moreover, the above mentioned BCL11A isoforms differ in the number of C2H2 zinc finger domains. The human BCL11A-XS isoform lacks the C2H2 domain while the murine one contains just one C2H2 domain, like the human and mouse BCL11A-S isoforms. Both the human and mouse BCL11A-L isoforms contain three C2H2 domains, whereas the BCL11A-XL contains all six of them **(Figure 3A)**.

A study from Nakamura and colleagues showed that the longer BCL11A isoforms are located in the nucleus whereas short isoform are restricted to the cytoplasm, thus suggesting a possible modulating function of the transcriptional activity of a BCL11A protein complex

(Nakamura et al., 2000). BCL11A isoforms have been shown to be expressed to various degrees in different tissues, but the different isoforms in the brain have not been linked to specific functions so far (Simon et al., 2020).

1.4.2 *BCL11A* and neurological disorders

Several studies on patients carrying heterozygous mutations for *BCL11A* revealed neurodevelopmental disorders including intellectual disabilities and behavioural problems (Basak et al., 2015; Dias et al., 2016; Peron et al., 2019.; Simon et al., 2020; Deciphering Developmental Disorders Study, 2015) **(Figure 3B)**.

In a study by Basak and colleagues, three patients with rare 2p15-p16.1 microdeletion syndrome who presented autism spectrum disorder and developmental delay were characterized (Basak et al., 2015). Of the genes within 2p15-p16.1, only *BCL11A* was commonly deleted in all the patients. Moreover, evaluation of gene expression data sets from developing and adult human brains revealed that its expression patterns are similar to genes associated with neurodevelopmental disorders. These data implicate that BCL11A is an important factor for neurodevelopment (Basak et al., 2015). Additionally, the 2p15-16.1 microdeletion syndrome leads to brain abnormalities like hypoplasia of the corpus callosum, neocortex, amygdala and hippocampus (Simon et al., 2020). Dias and colleagues used a comprehensive integrated approach to intellectual disabilities modelling and demonstrated that missense variants cluster in the amino-terminal region of human BCL11A. These mutations disrupt BCL11A localization, dimerization and transcriptional regulatory activity, consistent with a loss of function (Dias et al., 2016). *BCL11A*-related intellectual disabilities have been further characterized clinically by developmental delay, mild to severe intellectual disability, microcephaly and behaviour problems (Peron et al., 2019). In addition, seizures and autism spectrum disorder have been reported as well in some affected individuals. Notably, autism spectrum disorders have been shown to be also caused by impaired remodelling of the BAF complex, in which BCL11A takes part (Basak et al., 2015; Dias et al., 2016; Simon et al., 2020). Moreover, *BCL11A* was reported by different large scale exome sequencing studies as a candidate risk gene for neuropsychiatric disorders that are linked with impaired neocortical development (Cooper et al., 2011; Iossifov et al., 2012; Deciphering Developmental Disorders Study, 2015).

1.4.3 BCL11A in the murine CNS

In the mouse, BCL11A is known to regulate neuronal fate determination during spinal cord and cortex development (Simon et al., 2020) **(Figure 3C)**. Dorsal spinal neurons require

BCL11A for terminal differentiation and morphogenesis (John et al., 2012). In fact, the disrupted differentiation of dorsal spinal neurons in *Bcl11a* conditional knock-out mice interferes with their correct innervation by cutaneous sensory neurons, thus with the proper formation of the somatosensory circuitry within the dorsal spinal horn. This connectivity is in part established by the Wingless-related integration site (WNT) pathway component secreted frizzled-related protein 3 (FRZB/SFRP3), which was identified as the first functional downstream target of BCL11A during CNS development (John et al., 2012).

Using conditional gene inactivation of *Bcl11a* in cortical projection neurons, Wiegreffe and colleagues demonstrated that BCL11A regulates polarity and migration of cortical upper layer neurons (Wiegreffe et al., 2015). BCL11A-deficient late born neurons destined to settle in superficial cortical layers do not correctly switch from multipolar to bipolar morphology, resulting in impaired radial migration and thus misdistribution. Wiegreffe and colleagues identified semaphorin 3C (SEMA3C), a secreted glycoprotein and guidance molecule, as a critical component downstream of BCL11A required for radial migration. Specifically, they showed that expression of *Sema3c* is increased in migrating BCL11A-deficient neurons and that BCL11A is a direct negative regulator of *Sema3c* transcription. In fact, BCL11A binds to a regulatory element in the second intron of the *Sema3c* gene that conveys transcriptional repression. Interestingly, knockdown of *Sema3c* in *Bcl11a* mutants restores radial migration in cortical projection neurons. Thus, BCL11A acts through SEMA3C as an important regulator of radial migration in developing cortical projection neurons (Wiegreffe et al., 2015). In addition to its function in cortical projection neurons, BCL11A has been shown to be necessary for the postmitotic development of corticothalamic, callosal and subcerebral projection neurons. These different neuronal subtypes connect deep layers of the cortex with other brain regions, and BCL11A ensures that they are produced in appropriate proportions and locations (Woodworth et al., 2016). In fact, loss of BCL11A function results in a bias in favour of subcerebral projection neurons development in sensory cortex at the expense of callosal and corticothalamic neurons. In contrast, BCL11A overexpression in deep cortical layers suppresses subcerebral neuron identity and projection toward the spinal cord.

Thus, BCL11A specifies subtype identity in deep-layer cortical neurons, preventing corticothalamic and callosal projection neurons to acquire a subcerebral projection neuron identity (Woodworth et al., 2016). In a different study, Canovas and colleagues contradicted this model by showing that the development of subcerebral projection neurons in the neocortex depends on their high BCL11A expression levels (Canovas et al., 2015). In fact, reducing the expression levels of BCL11A in deep cortical layers by small hairpin RNA leads to increased TBR1 expression and decreased subcerebral neuron fate. Therefore, the repression of TBR1 expression by BCL11A appears as a critical step for the acquisition of the subcerebral fate. This discrepancy might be due to the different experimental models used in

the above mentioned studies, and could be explained by residual expression of BCL11A after knockdown as compared to genetic loss of function (Simon et al., 2020). Furthermore, BCL11A controls the acquisition of sensory area identity and establishment of sensory input fields in the developing neocortex (Greig et al., 2016). In *Bcl11a* conditional knock-out mice, abnormal gene expression causes aberrantly motorized corticofugal and cortico-cortical output connectivity. Moreover, selective loss of BCL11A in the cortex deprives thalamocortical axons of their receptive sensory field (Greig et al., 2016).

While all the above-mentioned studies point to the importance of BCL11A in the development of the central nervous system (CNS), the function of BCL11A in development and maintenance of the mDA system has not been examined.

Figure 3. BCL11A isoforms and the role of BCL11A in human and murine CNS. (A) Alternative splicing of *Bcl11a* leads to four BCL11A isoforms named XS, S, L and XL. Each isoform contains 1, 3, or 6 C2H2 zinc-finger domains required for DNA-binding. Exon 1 and 2 contain the NuRD interacting domain and a C2HC zinc-finger domain involved in protein-protein interaction and are common to all but the BCL11A-XS isoform. **(B-C)** Table summarizing BCL11A function in human **(B)** and murine CNS **(C)**.

2. OBJECTIVES OF THE STUDY

Midbrain dopaminergic neurons (mDA) are anatomically organized into the substantia nigra (SN), ventral tegmental area (VTA) and retro-rubral field (RRF). These anatomically defined areas contain subpopulations of mDA neurons that are characterized by distinct molecular profiles, distinct connectivity, and distinct impacts on dopamine-modulated behaviour. The molecular mechanisms that establish this diversity in mDA neurons during development have still not been fully elucidated.

The first aim of the present study was to characterize a subpopulation of mDA neurons expressing the transcription factor BCL11A. To assess whether *Bcl11a* was indeed identifying a subset of mDA neurons, the developmental time course of its expression and the distribution of *Bcl11a*-expressing mDA neurons in the adult brain were analysed. To investigate whether *Bcl11a*-positive mDA neurons were falling in any of the already known subclasses of DA neurons, the co-expression of several subset markers was assessed. To examine whether Bcl11a-expressing mDA neurons were forming a subcircuit within the DA system, an intersectional genetic approach was used. Considering the presence of *Bcl11a*-positive but TH negative neurons within the midbrain, this approach was needed to specifically label only mDA neurons expressing *Bcl11a* and their projections to forebrain target area. To investigate the projections of mDA neurons that express *Bcl11a* in the adult brain anterograde viral mediated tracing and retrograde tracing approaches were combined.

The second aim of this study was to investigate whether BCL11A was necessary for establishing and/or maintaining *Bcl11a*-expressing mDA neuron subpopulation. To this end, a conditional knock-out for *Bcl11a* in mDA neurons was generated and the anatomical organization of the mDA area was analysed. To assess whether *Bcl11a* was necessary for the cell fate determination of *Bcl11a*-positive mDA neurons, a subtype markers analysis was performed in conditional knock-out mice. Moreover, an array of behavioural experiments was carried out to investigate whether the loss of *Bcl11a* lead to functional impairment in the mDA system.

The third aim of this study was to elucidate the role of Bcl11a-expression in the context of neurodegenerative processes affecting mDA neurons in the SN. Therefore, mDA neurons were challenged with α-synuclein overexpression, a model for Parkinson´s disease. The subsequent loss of mDA neurons and their projections was then compared between control and conditional knock-out mice.

This study was performed to gain a better understanding of the functional organization of the DA system and its susceptibility to neurodegeneration in the adult brain.

3. MATERIALS AND METHODS

3.1 Materials

3.1.1 Table 2: Equipment

Product	Model/Cat. No.	Manufacturer	Registered Office
Autoclave	DX-150 benchtop	SysTec	Bergheim, DE
Balance	AC211S	Sartorius	Göttingen, DE
Balance	ATL-822-1	Sartorius	Göttingen, DE
Beam Walking Assay equipment	12 mm wide, 1 m long rod made of synthetic material		
Cryostat	Leica CM 3050S	Leica Biosystems	Wetzlar, DE
Gel chamber	Model 41-1525	PeqLab	Erlangen, DE
Gel chamber	Model 40-1515	PeqLab	Erlangen, DE
Gel imager	Gel Doc XR+ with Image Lab Software	BioRAD	Hercules, CA, USA
Homoeothermic Monitoring System for Small Rodents	55-7020	Harvard Apparatus	Holliston, MA, USA
Incubator (with shaker)	KS-15	Edmund Bühler GmbH	Bodelshausen, DE
Magnetic Stirrer	AGE 1200 rpm	VELP Scientifica	Usmate, IT
Micro drill 50/60 Hz 200-240 V	Omni Drill 35	World Precision Instruments	Sarasota, FL, USA
Microinjection Pump Micro4	UMP4	World Precision Instruments	Sarasota, FL, USA
Open Field Arena	open arena (30x 30 x 30 cm)		
pH Meter	FE20 FiveEasy	Mettler Toledo	Columbus, OH, USA
Power Supply Electophoresis	EV231	PeqLab	Erlangen, DE
Refrigerators Freezers 4°C, -20°C, -80°C	G2013 Comfort HERAfreeze	Liebherr Kendro	Lindau Hanau, DE

RNAScope® Hybridization oven	PN 321710/321720	Advanced Cell Diagonostic	Newark, USA
RotaRod Apparatus	47600	Ugo Basile	Gemonio, IT
Rocking platform	4440148	VWR	Darmstadt, DE
Social Behavior test equipment	3 chambers arena equipped with two 10 cm^2 cages		
Shaker	Nutation Mixer	VWR	Darmstadt, DE
Stereotactic Frame with Digital Display Console	Model 942	David Kopf Instruments	Tujunga, CA, USA
Thermocycler	DANN engine PTC-200	BioRAD	Hercules, CA, USA
Thermocycler	Biometra TRIO	Analytik Jena	Jena, DE
Vortexer	Vortex Genius	IKA	Staufen, DE
Waterbath	10679808	FGL	Burgwedel, DE

3.1.2 Table 3: List of microscopes

Microscope/Equipments	Model/Cat. No.	Manufacturer	Registered Office
Epifluorescence Microscope	AxioObserver Z1	Carl Zeiss	Oberkochen, DE
10x objective	EC PlnN 10x/0.3 DIC I 1.11µm	Carl Zeiss	Oberkochen, DE
20x objective	EC PlnN 20x/0.5 DIC II 0.67 µm	Carl Zeiss	Oberkochen, DE
40x objective	Pln Apo 40x/1.3 Oil DIC III 0.26 µm	Carl Zeiss	Oberkochen, DE
63x objective	Pln Apo 63x/1.4 Oil DIC II 0.24µm	Carl Zeiss	Oberkochen, DE
ApoTome	ApoTome.2	Carl Zeiss	Oberkochen, DE
Fluorescence Lamp	Illuminator HXP120C	Carl Zeiss	Oberkochen, DE
Microscope Camera (ApoTome)	AxioCam MRm	Carl Zeiss	Oberkochen, DE

Microscope Color Camera (ApoTome)	AxioCam MRc	Carl Zeiss	Oberkochen, DE
Power Unit	Power Supply 231	Carl Zeiss	Oberkochen, DE

Microscope/Equipments	Model/Cat. No.	Manufacturer	Registered Office
Spinning Disk Confocal Microscope)	AxioObserver 7	Carl Zeiss	Oberkochen, DE
40x objective	C-Apochromat, 40x/1.2 water	Carl Zeiss	Oberkochen, DE
405 nm laser line	VS-Laser control	Visitron Systems	Puchheim, DE
488 nm laser line	VS-Laser control	Visitron Systems	Puchheim, DE
561 nm laser line	VS-Laser control	Visitron Systems	Puchheim, DE
Microscope Camera	sCMOS pco.edge 4.2	PCO	Kelheim, DE
Spinning Disk Unit	CSU-W1	Yokogawa Electric Corporation	Tokyo, JP

Microscope/Equipments	Model/Cat. No.	Manufacturer	Registered Office
Axio Scope	Axio Scope.A1	Carl Zeiss	Oberkochen, DE
Microscope Camera	AxioCam 503 Color	Carl Zeiss	Oberkochen, DE

Microscope/Equipments	Model/Cat. No.	Manufacturer	Registered Office
Motorized microscope	IX2 UCB	Olympus	Shinjuku, Tokyo, JP
63x objective	Plan-Apo, 63x/1.4 oil	Olympus	Shinjuku, Tokyo, JP
Spinning Disk Unit	Olympus DSU	Olympus	Shinjuku, Tokyo, JP
Microscope Camera	EM-CCD	Olympus	Shinjuku, Tokyo, JP

Microscope/Equipments	Model/Cat. No.	Manufacturer	Registered Office
OP-Microscope	VM900	Möller-Wedel GmbH	Wedel, DE

3.1.3 Table 4: Data acquisition and analysis

Computing	Software	Manufacturer	Registered office
Gel documentation	Quantity one	BioRAD	Hercules, CA, USA
Image acquisition	Zen 2 (blue edition)	Carl Zeiss	Oberkochen, DE
Image acquisition	VisiView	Visitron Systems	Puchheim, DE
Image editing	Affinity Designer 1.5.5	Serif	Nottingham, UK
Image processing	Affinity Photo 1.5.5	Serif	Nottingham, UK

Image processing	Fiji version 1.0	Wayne Rasband, National Institute of Health	Bethesda, USA
Statistical analysis	GraphPad Prism version 8.4.2	GraphPad Software	San Diego, USA
Statistical analysis	R	The R Foundation of Statistical Computing	Vienna, AT
Stereological cell counting	Stereo Investigator 9	MBF Biosciences	Williston, VTA, USA
Video tracking and editing	EthoVision XT version 9.0	Noldus	Wageningen, NL

3.1.4 Table 5: Consumables

Product	Model/Cat. No	Manufacturer	Registered office
12-well culture plate	353043	BD Biosciences	Heidelberg, DE
24-well culture plate	353047	BD Biosciences	Heidelberg, DE
34 G Beveled Nanofil Needle	NF34BV-2	World Precision Instruments	Sarasota, FL, USA
36 G Beveled Nanofil Needle	NF36BV-2	World Precision Instruments	Sarasota, FL, USA
Adhesion Slides	Super Frost Ultra Plus	Menzel-Gläser	Braunschweig, DE
Autoclave tape	SteriClin sticky tape	VP group	Feuchtwangen, DE
Blades	Apollo	Apollo Herkenrath GmbH & Co KG	Sarstedt, USA
COATED VICRYL® Plus Antibacterial (polyglactin 910) Suture	V303H	Ethicon	Somerville, NJ, USA
Cover slips	LAME110071	Labomedic	Bonn,DE
Castroviejo Needle Holder (14 cm)	12565-14	Fine Science Tools	Heidelberg, DE
Dako Pen	S2002	Agilent	Santa Clara, CA, USA
DermaClean gloves	PFC 4303971	Ansell	Munich, DE
Disposable blades	14035838382	Leica Biosystems	Wetzlar, DE
Embedding molds	Peel-A-Way	Polysciences Inc.	Eppelheim, DE
Eppendorf tubes 1.5mL	72690	Eppendorf AG	Hamburg, DE
Eye ointment	Bepanthen Augen und Nasenalbe	Bayer	Leverkusen, DE
Feeding Needles-Single Use	18061-20	Fine Science Tools	Heidelberg, DE
Filter tips	ART 100/200/1000	Thermo Fisher Scientific	Schwerte, DE
Forceps Dumont (#5)	11252 – 30	Fine Science Tools	Heidelberg, DE

Graefe Forceps (0.8mm)	11050-10	Fine Science Tools	Heidelberg, DE
Heating Pad	464-265	ThermoLux	Murrhardt, DE
Iris scissors (11 cm)	14060-11	Fine Science Tools	Heidelberg, DE
Iris scissors (9 cm)	14060-09	Fine Science Tools	Heidelberg, DE
Lens Cleaning Tissue 105	2105841	Whatman	Dassel, DE
Liquid scintillation vials	Z190527	Merck	Darmstadt, DE
Microscope Slides	Super Frost	Menzel-Gläser	Braunschweig, DE
NanoFil Microsyringe (10 µL)	NANOFIL	World Precision Instruments	Sarasota, FL, USA
Needles	0.40x20 mm BL/LB 27Gx3/4''	Braun	Melsungen, DE
Noyes Spring Scissors (14mm)	15012-12	Fine Science Tools	Heidelberg, DE
Noyes Spring Scissors (14mm)	15012-12	Fine Science Tools	Heidelberg, DE
Parafilm, PM996	P7793-1EA	Merck	Darmstadt, DE
Pasteur Plastic Pipettes (1 ml)	2655181	VWR	Darmstadt, DE
PCR strip tubes	732-0551	VWR	Darmstadt, DE
PCR tubes with individual cap	732-0545	VWR	Darmstadt, DE
Perforated Spoon	Moria MC17BIS 10370- 18	Fine Science Tools	Heidelberg, DE
Petri dishes (15 mm)	351029	BD Biosciences	Heidelberg, DE
Pipettes (10, 20, 200, 1000 µL)	FA10002M FA10003M FA10005M FA10006M	Gilson	Middleton, WI, USA
Pipette-boy Accujet pro	26300	Brand	Wertheim, DE
Polypropylene conical tubes 15mL	352096	Fine Science Tools	Heidelberg, DE
Polypropylene conical tubes 50mL	352070	BD Biosciences	Heidelberg, DE
Rein Rotmarder Brush 770	149-2120	VWR	Darmstadt, DE
Scalpel Blades No. 10	0201000010	Feather Safety Razor Co. ltd.	Köln, DE
Scalpel handle	0003-12	Fine Science Tools	Heidelberg, DE
Serological pipettes	4487 (5mL) 4488 (10mL) 4489 (25mL)	Corning Life Sciences	Kaiserslautern, DE
Slide boxes	HS15994E	Carl Roth GmbH	Karlsruhe, DE
Student surgical scissors	91401-12	Fine Science Tools	Heidelberg, DE
Surgical skin marker	Securline skin marker-sterile	Sigma Aldrich	St. Louis, MO, USA

Syringes – 1mL	2-piece fine dosage/9166033V 3-piece fine dosage/9161465V	Braun	Melsungen, DE
Syringes – 50mL	Omnifix Solo 50 ml	Braun	Melsungen, DE
Tissue Wipes	05511	KimTech	Surrey, UK
Winged Needle	P295A05	Venisystems	Hospira, USA
Xylocain Pumpspray	03839499	Astra Zeneca GmbH	Cambridge, UK

3.1.5 Table 6: Chemical reagents

Chemicals	**Catalog No.**	**Manufacturer**	**Registered office**
Ampuwa water	40676.00.00	Ampuwa, Fresenius	Bad Homburg, DE
Antisedan (Atipamezole) 5 mg/mL	134786-3	Vetoquinol	Lure Cedex, FR
Aqua-PolyMount	18606	Polysciences Inc.	Eppelheim, DE
Bromophenol blue	A1120.005	AppliChem	Darmstadt, DE
Carprofen	QM01AE91	Virbac	Carros, FR
Cepetor 1 mg/mL (medetomidinhydrochloride)	798-491	Cp-Pharma	Burgdorf, DE
Corn oil	C8267-500ML	Sigma-Aldrich	St. Louis, MO, USA
DNA Ladder 100bp	15628019	Thermo Fisher Scientific	Waltham, MA, USA
DNA Ladder 1Kb Plus	10787-018	Thermo Fisher Scientific	Waltham, MA, USA
dNTPs (100mM)	28-4065-52	GE Healthcare	Dornstadt, DE
EDTA	E6511	Merck	Darmstadt, DE
Ethidium bromide	2218.2	Carl Roth	Karlsruhe, DE
Ethylene glycol	1009492500	Merck	Darmstadt, DE
Flumazenil Hikma 0.1 mg/mL	V03AB25	Hikma Pharmaceuticals	London, UK
Glacial acetic acid	A6283-1L	Merck	Darmstadt, DE
Glycerol	G5516	Sigma Aldrich	St. Louis, MO, USA
Hoechst 33258	ab228550	Abcam	
Ketanest®	Ketanest® S 25 mg/ml	Pfizer	New York, NY, USA
Magnesium chloride (MgCl$_2$)	25108.260	VWR	Darmstadt, DE
Midazolam	Midazolam HEXAL®	HEXAL	Holzkirchen, DE
Naloxon PUREN 0.4 ml/mL	11356645	PUREN Pharma	München, DE
Normal donkey serum (NDS)	017-000-121	Jackson ImmunoResearch	Ely, Cambridgeshire, UK
Paraformaldehyde (PFA)	0335.2	Carl Roth	Karlsruhe, DE

Potassium chloride (KCl)	26764.260	VWR	Darmstadt, DE
Potassium phosphate monobasic (KH$_2$PO$_4$)	P9791	Merck	Darmstadt, DE
Rompun®	Rompun® 2%	Bayer	Leverkusen, DE
RNAse away	13398800	Roche	Basel, CH
RNAScope® Hydrogen Peroxide Reagent	322330	Advanced Cell Diagnostic	Newark, USA
RNAScope®Protease III	322340	Advanced Cell Diagnostic	Newark, USA
RNAScope® Target Retrieval	322000	Advanced Cell Diagnostic	Newark, USA
RNAScope® Wash buffer	322000	Advanced Cell Diagnostic	Newark, USA
Sodium bicarbonate (NaHCO$_3$)	27775.293	VWR	Darmstadt, DE
Sodium chloride (NaCl)	27788.297	VWR	Darmstadt, DE
Sodium dihydrogen phosphate (NaH$_2$PO$_4$ 2H$_2$O)	28013.264	VWR	Darmstadt, DE
Sodium hydroxide (NaOH)	31627.290	VWR	Darmstadt, DE
Sodium phosphate (Na$_2$HPO4)	28028.298	VWR	Darmstadt, DE
Sucrose	27480.360	Sigma Aldrich	St. Louis, MO, USA
Tamoxifen	T5648-5G	Sigma Aldrich	St. Louis, MO, USA
Taq DNA polymerase recombinant	10342-020	Thermo Fischer Scientific	Waltham, MA, USA
Tissue Tek O.C.T.	4583	Sakura	Alphen aan den Rijn, NL
Transcription Buffer (10x)	10881767001	Roche	Basel, CH
Tris-HCl	108219.1000	Merck	Darmstadt, DE
Triton X-100	1.08219.1000	Merck	Darmstadt, DE
Tween-20	28829.183	VWR	Darmstadt, DE
Xylene cyanol	335940-10G	Sigma Aldrich	St. Louis, MO, USA

3.1.6 Table 7: Buffers and solutions

Buffer/Solution	Content
Blocking solution for immunohistochemistry (IHC)	For embryonic/P0 tissue: 10% normal donkey serum (NDS) in 0.2% PBT (PBS 1X plus 0.2% Triton X-100) For adult tissue: 10% normal donkey serum (NDS) in 0.5% PBT (PBS 1X plus 0.5% Triton X-100)
Loading buffer 10X (gel electrophoreses)	50% Glycerol 0.4% Bromphenol blue 0.4% Xylene Cyanol mixed and stored at 4°C
Lysis buffer	333 µL 1.5 M Tris, pH 8.8 (50 mM)

	20 µL 0.5 M EDTA (1 mM) 500 µL 10% Tween 9.1 mL dH2O stored at -20°C
Phosphate buffer solution (PBS) 5X	40 g NaCl (137 mM) 1 g KCl (2,7 mM) 7.1 g Na_2HPO_4 (10 mM) 1.36 g KH_2PO_4 (2 mM) in ~1 L dH2O stored at room temperature
Paraformaldehyde (PFA) 20%	500 g PFA in ~2.0 L dH2O 8.0 mL NaOH to adjust pH to 7.0 filtered through 0.4 µm filter and stored at -20°C
PFA 4% (fixation solution)	10 mL 20% PFA in 50mL PBS 1X
PBT 0.2% (IHC)	20 mL 10% Triton-X (0.2 %) 990 mL PBS 1X
PBT 0.3% (IHC)	30 mL 10% Triton-X (0.3 %) 970 mL PBS 1X
PBT 0.5% (IHC)	50 mL 10% Triton-X (0.5 %) 950 mL PBS 1X
Tissue digestion buffer	1. NaOH solution: 25 mM NaOH 0.2 mM EDTA 2. Tris solution: 40 mM Tris HCl calibrate to pH 5.5
Tris-acetate-buffer (TAE) 1X (gel electrophoreses)	50X TAE diluted 1:50 with H2O stored at room temperature
TAE 50X (gel electrophoreses)	242g Tris-base 100mL 0.5M EDTA (pH 8.0) 57.1mL glacial acetic acid in ~1L H2O stored at room temperature

Walter´s antifreeze solution (adult cryosections storage)	400 mL Phosphate buffer 100 mM:
	    1.57 g Na_2HPO_4
	    5.45 g Na2HPO4
	    in ~400 mL dH2O
	300 mL Etylene glycol
	300 mL Glycerol
	stored at room temperature

3.1.7. Antibodies

3.1.7.1 Table 8: Primary antibodies

Primary antibody	Cat. No.	Manufacturer	Registered office
goat anti-β-gal	Discontinued, see Alvarez Bolado et al., 2012	Biogenesis	Kingston, NH, USA
guinea pig anti-BCL11A		Kindly provided by Stefan Britsch, University of Ulm	
mouse anti-human -synuclein	36-008	Merck	Darmstadt, DE
mouse anti-TH	MAB318	Merck	Darmstadt, DE
rabbit anti-ALDH1A1	HPA002123	Sigma-Aldrich	St. Louis, MO, USA
rabbit anti-Calbindin	CB38	Swant	Marly, CH
rat anti-GFP	04404-26	Nacalai Tesque	Kyoto, JP
rabbit anti-RFP	600-401-379	Rockland-inc	Hamburg, DE
rabbit anti-SOX6	ab30455	Abcam	Cambridge, UK
rabbit anti-TH	AB152	Merck	Darmstadt, DE

3.1.7.2 Table 9: Secondary antibodies

Secondary antibody	Cat. No.	Manufacturer	Registered office
Cy3-Streptavidin	016-160-084	Jackson ImmunoResearch	Ely, Cambridgeshire, UK
donkey anti-goat Cy3	705-165-147	Jackson ImmunoResearch	Ely, Cambridgeshire, UK
donkey anti-guinea pig Biotin	706-065-148	Jackson ImmunoResearch	Ely, Cambridgeshire, UK
donkey anti mouse-Alexa 488	A-21202	Thermo Fischer Scientific	Waltham, MA, USA
donkey anti mouse-Alexa 647	A-31571	Thermo Fischer Scientific	Waltham, MA, USA
donkey anti rabbit-Alexa 488	A-21206	Thermo Fischer Scientific	Waltham, MA, USA
donkey anti rabbit-Alexa 546	A10040	Thermo Fischer Scientific	Waltham, MA, USA

donkey anti rabbit-Alexa 647	A-31573	Thermo Fischer Scientific	Waltham, MA, USA
donkey anti rat-Alexa 488	A-21208	Thermo Fischer Scientific	Waltham, MA, USA

3.1.8 Table 10: RNAScope® probes

RNA probe	Manufacturer	Registered office
Mm-Bcl11a-C3	Advanced Cell Diagnostic	Newark, USA

3.1.9 Table 11: Enzymes

Enzyme	Cat. No.	Manufacturer	Registered office
Proteinase K	03115879001	Roche	Basel, CH

3.1.10 Table 12: PCR primers for genotyping mice

PCR	Primer	Sequence 5'-3'
Ai82D	WT R	CAC ACC TTT AAT CCC GAT GC
	WT F	TTC CCC AAC GGT CAC TTA CT
	MT R	CTG AAC TTG TGG CCG TTT AC
	MT F	ACG AGA TCA GCA GCC TCT GT
Ai9	WT R	CCG AAA ATC TGT GGG AAG TC
	WT F	AAG GGA GCT GCA GTG GAG TA
	MT R	GGC ATT AAA GCA GCG TAT CC
	MT F	CTG TTC CTG TAC GGC ATG G
Bcl11a-flox	LP	GAG GCT TGC AGA AAC AGA AAG AT
	UP	TAG CTC CTG CTA GCC AGG TTT CTT
Cre	Cre F	TAA AGA TAT CTC ACG TAC TGA CGG TG
	Cre R	TCT CTG AGC AGA GTC ATC CTT AAG C
CreER	ERT1	ERT 1: GCC TGG TCT GGA CAC AGT GCC
	ERT2	ERT 2: CTG TCT GCC AGG TTG GTC AGT AAG C
Dat-tTA	WT R	TGA TGA GGG TGG AGT TGG TC
	MT R	AGA AGA AGG AAA CAG ACT TCC TC
	F	GCT TGT TCT TCA CGT GCC AGT
LacZ	LacZ 1	GTA CCA CAG CGG ATG GTTCGG
	LacZ 2	GCG ATG TCG GTT TCC GCG A

3.1.11 Table 13: Adeno-associated viruses

AAV	Cat. No.	Manufacturer	Registered office
AAV1/2-EF1α-DIO-ChR2-eYFP		UKB Viral Core Facility, Bonn, DE	
pAAV-EF1a-double floxed-hChR2(H134R)-mCherry-WPRE-HGHpA	20297-AAV1	Addgene	Watertown, MA, USA
AAV1/2-EF1α-pTRE-FLEX-ChETA-eYFP		UKB Viral Core Facility, Bonn, DE	

AAV2/6-hSYN1-h-α-synuclein-WPRE		Sirion Biotech, Martinsried, DE	

3.1.12 Table 14: Cholera toxin subunit B

Product	Cat. No.	Manufacturer	Registered office
Cholera toxin subunit B-Alexa Fluor 488 Conjugate	C34775	Thermo Fischer Scientific	Waltham, MA, USA

3.1.13 Table 15: List of mouse lines

Name	Allele symbol	Provided by/purchased from	Reference
Ai82D (TITL-GFP)	*Igs7$^{tm82.1(tetO-EGFP)Hze}$*	The Jackson Laboratory	Madisen et al., 2015
Ai9	*Gt(ROSA)26Sor$^{tm9(CAG-tdTomato)Hze}$*	The Jackson Laboratory	Madisen et al., 2010
Bcl11a^{CreER}		Dr. Walid Khaled, University of Cambridge	
Bcl11a^{flox}	*Bcl11a$^{tm2.1Peli}$*	Dr. Pentao Liu, The University of Hong Kong; Prof. Stefan Britsch, University of Ulm; Prof. Dr. Neal Copeland, Institute for Academic Medicine, Houston Methodist	Wiegreffe et al., 2015
Bcl11a^{lacz}	*Bcl11a^{tm3Peli}*	Dr. Pentao Liu, The University of Hong Kong	Dias et al., 2016
DAT$^{IRES-Cre}$	*Slc6a3$^{tm1.1(cre)Bkmn}$*	The Jackson Laboratory	Bäckman et al., 2006
Dat^{tTA}	*Slc6a3$^{tm4.1(tTA)Xz}$*	The Jackson Laboratory	Chen et al., 2015

3.2 Methods

3.2.1 Mice

3.2.1.1 Mouse breeding and maintenance

Mice were housed in a controlled environment, with 12 hr light/night cycles and ad libitum availability of food and water. The *Bcl11a^{lacZ}* line was kept on a C57BL/6 background. All other transgenic mouse lines were maintained on a CD1/ C57BL/6 mixed background. Breedings

were set up using two females of at least six weeks of age and a male with at least eight weeks of age. Pups were weaned at postnatal day 21.

All experiments were performed in strict accordance with the regulations for the welfare of animals issued by the Federal Government of Germany, European Union legislation and the regulations of the University of Bonn. The protocol was approved by the Landesamt für Natur, Umwelt und Verbraucherschutz Nordrhein-Westfalen (Permit Number: 84-02.04.2014.A410, 84-02.04.2016.A238, 84-02.04.2015-A550).

3.2.1.2 Conditional gene inactivation of *Bcl11a* in mDA neurons

$Dat^{IRES-Cre}$ mice were generated by driving the Cre recombinase expression from the 3' untranslated region (3'UTR) of the endogenous dopamine transporter (DAT) gene (*Slc6a3*) by means of an internal ribosomal entry sequence (Bäckman et al., 2006). $Bcl11a^{flox}$ allele (Wiegreffe et al., 2015) was generated by introducing a neomycin resistance cassette (neo) at the 3′ end of exon 1 of the *Bcl11a* gene; exon 1 and the neomycin resistance cassette were flanked by loxP sites. The line was kindly provided by Dr. Pentao Liu, School of Biomedical Sciences, The University of Hong Kong, China; Prof. Stefan Britsch, University of Ulm and Prof. Dr. Neal Copeland, Institute for Academic Medicine, Houston Methodist. $Bcl11a^{lacZ}$ null allele (Dias et al., 2016) was generated by inserting an SA-IRES-lacZ cassette with a 3' loxP site into intron 3. An F3 site-flanked neomycin resistance cassette with a 5' loxP site was inserted downstream of exon 4. The line was kindly provided by Dr. Pentao Liu, School of Biomedical Sciences, The University of Hong Kong, China.

To inactivate *Bcl11a* specifically in mDA neurons, $Dat^{IRES-Cre}$ mice were crossed with $Bcl11a^{flox/flox}$ mice (*Bcl11a* cko mice; genotype: $Dat^{IRES-Cre/+}$, $Bcl11a^{flox/flox}$). In a subset of *Bcl11a* cko mice, the $Bcl11a^{lacZ}$ null allele was introduced by crossing $Dat^{IRES-Cre}$ mice with $Bcl11a^{flox/lacZ}$ mice (Genotype: $Dat^{RES-Cre/+}$, $Bcl11a^{flox/lacZ}$).

3.2.1.3 *Bcl11a*-expressing mDA neurons labelling using the intersectional fate mapping approach

The $Bcl11a^{CreER}$ mouse line was generated by inserting the DNA sequence for IRES (internal ribosomal entry site) and CreER (Cre recombinase fused with a modified form of the human estrogen receptor) together with a neo cassette in exon 4 of the *Bcl11a* gene. The resulting allele should be both an isoform (splice variant) of Bcl11a expressing the gene as well as CreER. This line was kindly provided by Dr. Walid Khaled, Department of Pharmacology, University of Cambridge. Dat^{tTa} (tetracycline trans-activator driven by the *Dat* promoter) mice (Chen et al., 2015) were generated by inserting a Tet operator (tetO)-tertacycline responsive

transactivator (tTA) "PF" (positive feedback) cassette between the *Dat* gene promoter and the coding sequence. An additional tTA was inserted right downstream of the DAT promoter and upstream of the "PF" cassette. In this mouse line, the DAT promoter initiates and directs tTA expression only in DA neurons and the tTA expression level is further amplified by the "PF" cassette. The intersectional reporter mouse line Ai82D (Madisen et al., 2015) is a Cre/Tet-dependent, fluorescent reporter line created by targeted insertion at the *Igs7* locus (TIGRE; an intergenic region on mouse chromosome 9 that allows reporter expression to be tightly regulated).

Intersectional fate mapping experiments were performed by using *Bcl11a^{CreER}* mice in conjunction with the *Dat^{TA}* mouse line and the intersectional reporter mouse line Ai82D. Day of vaginal plug was recorded at E0.5 and Tamoxifen (TM) (Sigma Aldrich) was administered by oral gavage to pregnant dams at E15.5 (0.05 ml/10g body weight) to label *Bcl11a*-expressing mDA neurons. Tamoxifen was prepared as a 20 mg/mL solution in corn oil (Sigma Aldrich).

3.2.1.4 Tissue biopsies and tissue lysis

Tail biopsies from embryonic/P0 mice and ear biopsies from adult mice were collected. Samples were digested in 100 µL of lysis buffer and 1 µL of proteinase K at 60°C for 3-4 hr embryonic/P0 biopsies) or for up to 8 hr (adult biopsies). Proteinase K was inactivated with an additional step of heat inactivation at 95°C for 10 minutes. Subsequently, 1 µL of digest supernatant was used to perform a polymerase chain reaction (PCR), in order to identify the above-mentioned transgenic alleles.

Alternatively, a shorter tissue digestion protocol was used. In this case, samples were digested in 75 µL of NaOH solution and incubated for 1 hr at 96°C and re-suspended in 75 µL of Tris HCl solution. 1:10 dilutions were prepared for each sample and 1 µL of diluted digest supernatant was used to perform a PCR.

3.2.1.5 Table 16: PCR protocols

AI82D			
Reaction mix (20 µL)	**Thermocycler program**		
1 µL Template DNA	Steps	Temp. (°C)	Time (min)
0.16 µl dNTPs (25 nM)	1) 1st Denaturing	94	2:00
1 µL WT F Primer (5 µM)	2) Denaturing	94	0:20
1 µL WT R Primer (5 µM)	3) Annealing	65 (-0.5 °C per cycle decrease)	0:15
1 µL MT F Primer (5 µM)	4) Extension	68	0:10
1 µL MT Primer (5 µM)	5) 2nd Denaturing	94	0:15

0.6 µL MgCl$_2$ (1.5mM)	6) Annealing	60	0:15
2 µL PCR rxn buffer (1X)	7) Extension	72	0:10
0.2 µL Taq Polymerase (1U)	8) Last Extension	72	2:00
12.04 µL dH$_2$O	9) Incubation	8	hold
	After step 4, repeat steps 2-4 for 10 cycles (touchdown) After step 7, repeat steps 5-7 for 28 cycles		
Gel electrophoresis	1.5% agarose		
Band size	Wild type band: 356 bp Mutant band: 239 bp		

Ai9			
Reaction mix (20 µL)	**Thermocycler program**		
1 µL Template DNA	Steps	Temp. (°C)	Time (min)
0.16 µl dNTPs (25 nM)	1) 1st Denaturing	94	2:00
1 µL WT F Primer (5 µM)	2) Denaturing	94	0:20
1 µL WT R Primer (5 µM)	3) Annealing	65 (-0.5 °C per cycle decrease)	0:15
1 µL MT F Primer (5 µM)	4) Extension	68	0:10
1 µL MT Primer (5 µM)	5) 2nd Denaturing	94	0:15
0.6 µL MgCl$_2$ (1.5mM)	6) Annealing	60	0:15
2 µL PCR rxn buffer (1X)	7) Extension	72	0:10
0.2 µL Taq Polymerase (1U)	8) Last Extension	72	2:00
12.04 µL dH$_2$O	9) Incubation	8	hold
	After step 4, repeat steps 2-4 for 10 cycles (touchdown) After step 7, repeat steps 5-7 for 28 cycles		
Gel electrophoresis	1.5% agarose		
Band size	Wild type band: 297 bp Mutant band: 196 bp		

Bcl11a^{flox}			
Reaction mix (20 µL)	**Thermocycler program**		
1 µL Template DNA	Steps	Temp. (°C)	Time (min)
0.16 µl dNTPs (25 nM)	1) 1st Denaturing	94	2:00
1 µL Lower Primer (5 µM)	2) Denaturing	94	0:15
1 µL Upper Primer (5 µM)	3) Annealing	65	0:30
0.6 µL MgCl$_2$ (1.5mM)	4) Extension	70	1:00
2 µL PCR rxn buffer (1X)	5) Last Extension	72	7:00
0.2 µL Taq Polymerase (1U)	6) Incubation	8	hold
14.04 µL dH$_2$O	Repeat steps 2-4 for 30 cycles		
Gel electrophoresis	1.5% agarose		
Band size	Wild type band: 377 bp Mutant band: 470 bp		

Cre			
Reaction mix (20 µL)	**Thermocycler program**		
1 µL Template DNA	Steps	Temp. (°C)	Time (min)

0.16 µl dNTPs (25 nM)	1) 1st Denaturing	95	2:00
1 µL Cre F Primer (5 µM)	2) Denaturing	95	0:40
1 µL Cre R Primer (5 µM)	3) Annealing	59	1:00
0.6 µL MgCl$_2$ (1.5mM)	4) Extension	72	0:50
2 µL PCR rxn buffer (1X)	5) Last Extension	72	10:00
0.2 µL Taq Polymerase (1U)	6) Incubation	8	hold
13.54 µL dH$_2$O	Repeat steps 2-4 for 30 cycles		
Gel electrophoresis	1.5% agarose		
Band size	Mutant band: 300 bp		

CreER			
Reaction mix (20 µL)	**Thermocycler program**		
1 µL Template DNA	Steps	Temp. (°C)	Time (min)
0.16 µl dNTPs (25 nM)	1) 1st Denaturing	94	2:00
1 µL ERT 1 Primer (5 µM)	2) Denaturing	94	1:00
1 µL ERT 2 Primer (5 µM)	3) Annealing	61	1:00
0.6 µL MgCl$_2$ (1.5mM)	4) Extension	72	1:00
2 µL PCR rxn buffer (1X)	5) Last Extension	72	10.00
0.2 µL Taq Polymerase (1U)	6) Incubation	8	hold
14.04 µL dH$_2$O	Repeat steps 2-4 for 30 cycles		
Gel electrophoresis	1.5% agarose		
Band size	Mutant band: 400 bp		

Dat^{tTA}			
Reaction mix (20 µL)	**Thermocycler program**		
1 µL Template DNA	1) 1st Denaturing	95	2:00
0.16 µl dNTPs (25 nM)	2) Denaturing	94	0:20
1 µL WT R Primer (5 µM)	3) Annealing	65 (-0.5 °C per cycle decrease)	0:30
1 µL MT R Primer (5 µM)	4) Extension	72	0:10
1 µL F Primer (5 µM)	5) 2nd Denaturing	95	0:15
0.6 µL MgCl$_2$ (1.5mM)	6) Annealing	60	0:30
2 µL PCR rxn buffer (1X)	7) Extension	72	0:10
0.2 µL Taq Polymerase (1U)	8) Last Extension	72	2:00
13.04 µL dH$_2$O	9) Incubation	8	HOLD
	After step 4, repeat steps 2-4 for 10 cycles (touchdown) After step 7, repeat steps 5-7 for 28 cycles		
Gel electrophoresis	2% agarose		
Band size	Wild type band: 184 bp Mutant band: 232 bp		

LacZ			
Reaction mix (20 µL)	**Thermocycler program**		
1 µL Template DNA	Steps	Temp. (°C)	Time (min)
0.16 µl dNTPs (25 nM)	1) 1st Denaturing	94	5:00
1 µL LacZ1 Primer (5 µM)	2) Denaturing	94	1:00
1 µL LacZ2 Primer (5 µM)	3) Annealing	61	1:00
0.6 µL MgCl$_2$ (1.5mM)	4) Extension	72	1:00
2 µL PCR rxn buffer (1X)	5) Last Extension	72	10:00
0.2 µL Taq Polymerase (1U)	6) Incubation	8	hold
13.54 µL dH$_2$O	Repeat steps 2-4 for 30 cycles		

| Gel electrophoresis | 1.5% agarose |
| Band size | Mutant band: 200 bp |

3.2.2 Histology

3.2.2.1 Tissue collection and fixation

Pregnant females were sacrificed by cervical dislocation. Embryos (E18.5) were dissected out of the uterus and immediately decapitated in ice cold PBS. Brains were dissected in ice cold PBS and then transferred to a previously cooled 12-well plate with 4% PFA. P0 pups were decapitated and their brains were dissected in ice cold PBS and then transferred to a previously cooled 12-well plate with 4% PFA. E18.5 and P0 brains were fixed in 4% paraformaldehyde (PFA) overnight at 4°C. Adult mice were anesthetised with an intraperitoneal injection of Ketanest/Rompun and the absence of pedal reflexes was verified before proceeding with the perfusion. Subsequently, mice were perfused transcardially with 50 mL PBS, followed by 50 mL 4% PFA. Brains were dissected out of the cranium, moved to a liquid scintillation vial and post-fixed overnight in 4% PFA at 4°C on a shaker.

3.2.2.2 Tissue cryopreservation

Previously fixed brains of E18.5 embryos, P0 and adult mice were washed in PBS and dehydrated as described below. First, brains were placed in a 15% sucrose in PBS solution at 4°C and were allowed to sink to the bottom of a 12 well plate (E18.5 embryos and P0 brains) or a liquid scintillation vial (adult brains). The same was done afterwards with a 30% sucrose in PBS solution. Brains were embedded in cryomolds filled with OCT TissueTek and frozen on dry ice before being stored at -80°C.

Processing of tissue from mice overexpressing α-synuclein involved post-fixation with 4% PFA for 24 hr followed by cryopreservation in 30% sucrose solution.

3.2.2.3 Tissue cryosectioning

Cryosectioning was performed with a Leica cryostat (CM 3050S), keeping the cryo-block and the knife temperature at -20°C. Embryonic and P0 brains were cryosectioned at 14 µm thickness and adhered on Superfrost Ultra Plus slide (Menzel-Gläser) in series of ten. Sections were dried for at least 2 hr at room temperature and stored in slide boxes at -20°C. Adult brains were sectioned at 40 µm thickness, collected as free floating sections in a 24-well plate and stored at -20°C in Walter´s antifreeze solution.

Adult brains from mice overexpressing α-synuclein were cut at 35 μm thickness using a freezing microtome.

3.2.3 Immunostaining

3.2.3.1 Immunostaining on frozen embryonic and P0 sections

For immunofluorescent staining, sections were thawed for 2 hr at room temperature (RT) in coplin jars (50 mL) and fixed in 4% PFA for 10 minutes. Slides were washed in PBS for 5 minutes and in PBS plus 0.2% Triton X-100 (Sigma Aldrich) (0.2% PBT), then placed into a humid chamber. Sections were incubated in 10% normal donkey serum (NDS) in 0.2% PBT for 1 hour at RT. Primary antibody incubation was carried on overnight (ON) at 4°C in a humid chamber. All primary antibodies were diluted in 3% NDS in 0.2% PBT. The following antibodies concentrations were used: goat anti-β-gal (1:2000), guinea pig anti-BCL11A (1:2500), mouse anti-TH (1:500), rabbit anti-CALBINDIN (1:5000), rabbit anti-SOX6 (1:500), rabbit anti-TH (1:500) and rat anti-GFP (1:2000). After incubation with primary antibodies, sections were washed 3 times (5 minutes each) with 0.2% PBT in coplin jars. Sections were placed back in a humid chamber and incubated for 2 hr at room temperature in the secondary antibody solution. All secondary antibodies were diluted in 3% NDS in 0.2% PBT. The following antibodies concentrations were used: donkey anti-goat Cy3 (1:200), donkey anti mouse-Alexa 647 (1:500), donkey anti rabbit-Alexa 488 (1:500), donkey anti rabbit-Alexa 546 (1:500) and donkey anti rat-Alexa 488 (1:500). Hoechst (1:10000) was added to the secondary antibody solution. After incubation with secondary antibodies, sections were washed 3 times (5 minutes each) with 0.2% PBT in coplin jars. Sections were air dried for 2 minutes and then mounted with Aqua Polymount. For the detection of BCL11A, a biotin-streptavidin amplification was required. After primary antibody incubation as described above, sections were incubated with donkey anti-guinea pig Biotin (1:200) in 3% NDS in 0.2% PBT for 2 hr at RT. After 3 washing steps (5 minutes each) with 0.2% PBT, sections were incubated for 1 hour at RT with Cy3-Streptavidin (1:1000) diluted in 0.2% PBT. Sections were mounted as described above.

3.2.3.2 Immunostaining on adult frozen sections

Free floating sections were re-fixed in 4% PFA for 10 min at RT, washed briefly with PBS and 0.3% PBT and incubated in 10% NDS in 0.5% PBT. Sections were incubated in primary antibody solution ON at 4°C. All primary antibodies were diluted in 3% NDS in 0.3% PBT. The following antibodies concentrations were used: goat anti-β-gal (1:2000), guinea pig anti-BCL11A (1:2500), mouse anti-TH (1:500), rabbit anti-ALDH1A1 (1:1000), rabbit anti-

CALBINDIN(1:5000), rabbit anti-RFP (1:1000), rabbit anti-TH (1:500) and rat anti-GFP (1:2000). In some cases, a longer incubation with rabbit anti-TH was needed; the primary antibody was then used at a concentration of 1:1000 and the incubation was carried out for 72 hr at 4°C. Sections were washed 3 times (5 minutes each) with 0.3% PBT and incubated in secondary antibody solution for 2 hr at RT. All secondary antibodies were diluted in 3% NDS in 0.3% PBT. The following antibodies concentrations were used: donkey anti-goat Cy3 (1:200), donkey anti rabbit-Alexa 488 (1:500), donkey anti rabbit-Alexa 546 (1:500) and donkey anti rat-Alexa 488 (1:500). Hoechst (1:10000) was added to the secondary antibody solution. Detection of BCL11A was carried out as described in section 3.2.3.1. Sections were washed 3 times (5 minutes each) with 0.3% PBT. All washing and incubation steps were carried out in a 24-well plate on shaker.

After staining, sections were mounted on Superfrost slides (Menzel-Gläser) and dried at RT for 5 minutes and then covered with Aqua Polymount.

After staining, sections were mounted on Superfrost Ultra Plus slides and allowed to dry at room temperature for 10 min. Coverslips with Aqua Polymount were put on top of the sections. Slides were stored at 4°C.

3.2.3.3 DAB immunostaining

DAB immunostainings against TH and human α-synuclein were performed on midbrain coronal sections from *Bcl11a* cko and control mice overexpressing human α-synuclein in the substantia nigra after rAAV injections (see section 3.2.7).

Staining of these sections followed previously described protocols (Helwig et al., 2016).

This experiment was performed by Dr. Ayse Ulusoy (DZNE, Bonn).

3.2.4 Multiplex fluorescent *in situ* hybridization

Multiplex fluorescent in situ hybridization was performed using RNAScope® Technology, which is a recent RNA *in situ* hybridization assay that allows visualization of single mRNA molecules in individual cells within tissue. This strategy is based on specific probes that amplify target-specific signals reducing background noise (Wang et al., 2012).

RNAScope was performed on pre-fixed frozen sections from P0 and adult mice tissue to visualize *Bcl11a* mRNA. Following RNAScope, immunostaining against TH was performed to visualize DA neurons.

Before hybridization, all steps were performed with equipment cleaned with RNAse Away Reagent. During the whole experiment DPBS and Ampuwa were used.

The following protocol was used, according to the instructions provided by the manufacturer for frozen tissue (User Manual: 323100-USM).

Day 1	
1.	Thaw slides for about 1 ½ h at RT
2.	Air dry slides at room temperature
3.	Dry slides at 40 °C, 30 min
4.	Fix in 4 % PFA, 10 min
5.	3x 3 min in sterile PBS
6.	Dehydration in 50 % ethanol, 3 min
7.	Dehydration in 70 % ethanol, 3 min
8.	Dehydration in 100 % ethanol, 3min
9.	Dry sections at 40 °C, 20 min
10.	Add 75 % hydrogen peroxide, incubate 10min
11.	2x 2min Ampuwa
12.	Heat up 1X target retrieval reagent to 98 °C
13.	Submerge slides in ampuwa water in the steamer for 10 s
14.	3 min 1X target retrieval reagent
15.	2x 2min Ampuwa
16.	Transfer slides to 3 min 100% ethanol
17.	Dry slides at 40 °C, 20min
18.	Create barrier with hydrophobic marker around the sections
19.	Load slides into RNAScope EZ-Batch Slide Holder and add protease III to each section, incubate for 15 min at 40 °C
20.	Warm probes for 10 min at 40 °C, cool to RT
21.	Dilute probes with probe diluent (1:50), if necessary
22.	2x 2min Ampuwa
23.	Add sufficient drops of probe mixture, incubate for 2 h at 40 °C in HybEZ oven
24.	2x 2 min 1X wash buffer
25.	Put slides in 5x SSC overnight
Day 2	
26.	2x 2 min 1X wash buffer at RT
27.	Add 4–6 drops RNAScope® Multiplex FL v2 Amp 1, incubate for 30 min at 40 °C in HybEZ oven
28.	2x 2 min 1X wash buffer at RT
29.	Repeat step 27.-28. With Amp 2
30.	Add 4–6 drops RNAScope® Multiplex FL v2 Amp 3, incubate for 15 min at 40 °C in HybEZ oven
31.	2x 2 min 1X wash buffer at RT
32.	To develop HRP-C1 signal: add 4–6 drops RNAScope® Multiplex FL v2 HRP-C1, incubate for 15 min at 40 °C in the HybEZ oven
33.	2x 2 min 1X wash buffer at RT
34.	Add 150–200 µL Cy3 fluorophore diluted in TSA per slide, incubate for 30 min at 40°C
35.	2x 2 min 1X wash buffer at RT
36.	15 min blocking with RNAScope® Multiplex FL v2 HRP blocker at 40 °C in the HybEZ oven
37.	2x 2 min 1X wash buffer at RT
38.	Repeat step 32.-37. With C2/C3-reagents to develop HRP-C2/C3 signal
39.	Wash with PBT and start regular IHC protocol

3.2.5 Anterograde tracing

3.2.5.1 Stereotactic viral vector injection

4 to 20 weeks old *Bcl11a^{CreER}* and *Bcl11a^{CreER}*, *Dat^{tTa}* mice were used to perform anterograde tracing experiments.

Mice were anesthetized with an intraperitoneal injection of Fentanyl/Midazolam/Medetomidin (100 µL/10g BW). The absence of pedal reflexes was verified before proceeding with the surgery. The fur was removed from the region between the mice ears and the mice were then placed under the stereotactic apparatus (David Kopf Instruments) and their head fixed with ears and tooth bars. An eye ointment was applied on the eyes in order to prevent drying of the corneas. The analgesic Carprofen (100 µL/10g BW) was administered via intraperitoneal injection. A microinjection syringe (WPI) equipped with a 34g bevelled needle (WPI) and previously filled with virus solution (pAAV-EF1α-double floxed-hChR2(H134R)-mCherry-WPRE-HGHpA, Addgene; AAV1/2-EF1α-DIO-ChR2-eYFP, UKB viral core facility; AAV1/2-EF1α-pTRE-FLEX-ChETA-eYFP, UKB viral core facility) was placed onto the stereotactic apparatus. A small incision from rostral to caudal was made with a scalpel through the midline of the skin in order to expose the surface of the skull. The stereotactic landmark bregma was identified using an OP-microscope and the arms of the stereotactic rig were manipulated in order to centre the tip of the needle directly on Bregma. At this point, the coordinates were all set to zero using a digital display console (David Kopf Instruments) and the needle was moved to the specific target using predetermined anterior/posterior (AP) and medial/lateral (ML) coordinates (SNc from Bregma: AP, -2.3 mm; ML, -1.1 mm; VTA from Bregma: AP, -3.44 mm; ML, -0.48 mm). A surgical skin marker was used to draw a small dot where the needle will enter the skull. Subsequently, a small hole was drilled with a micro drill and the needle was lowered to the surface of the brain to calculate the dorsal/ventral coordinates (SNc: DV, -4.1 mm; VTA: DV, -4-4 mm). The needle was slowly inserted in the brain to the desired depth and the viral injection started. 1 µl of virus solution was injected at a speed of 100 nL/min using a microsiringe pump controller (WPI). Once the injection was complete, the needle was kept in place for 3 min and slowly retracted over 1 min. The incision was closed with sutures (Ethicon) and gentamicin was applied on top. To let the mice emerge from anaesthesia, an antidote (Naloxone/Flumazenil/Atipamezole; 100 µL/10g BW) was administered via intraperitoneal injection. The surgery was performed keeping the mice body temperature at 37°C using a homoeothermic monitoring system (Harvard Apparatus). Mice were removed from the stereotactic apparatus and placed in a cage warmed up by a heating pad (ThermoLux) overnight. Mice were injected with Carprofen (100 µL/10g BW) 24 hr and 48 hr (Franklin & Paxinos, 2007) after the surgery. After 8 days from the viral injection, Tamoxifen was

administered to the mice by oral gavage (0.075 mL/10g BW) for 3 consecutive days. Two weeks after the last Tamoxifen administration, mice were perfused as described in paragraph 3.2.2.1. The brains were processed, sectioned and stained as described in paragraphs 3.2.2.2, 3.2.2.3 and 3.2.3.2.

3.2.6 Retrograde tracing

3.2.6.1 Cholera toxin subunit B stereotactic injection

4 weeks old *Bcl11a^{lacZ}* mice were used to perform retrograde tracing experiments. 1.5 µl of cholera toxin subunit B-Alexa Fluor 488 conjugate (CTB-Alexa 488, Thermo Fischer Scientific) was unilaterally injected as described in paragraph 3.2.5.1. into the lateral septum (LS, from Bregma: AP +0.98 mm ML -0.25mm, DV -2,6 mm), nucleus accumbens (NAc, from Bregma: AP +1.6 mm, ML -0.4 mm, DV -4 mm), the olfactory tubercles (OT, from Bregma: AP +1.3 mm, ML -1.10 mm, DV -5.2 mm) and the dorsal tail of the striatum (dTS, from Bregma: AP -0.7mm, ML -2.7 mm, DV 2.39 mm). One week after the injection mice were perfused as described in paragraph 3.2.2.1. The brains were processed, sectioned and stained as described in paragraphs 3.2.2.2, 3.2.2.3 and 3.2.3.2.

3.2.7 Alpha-synuclein overexpression

Recombinant adeno-associated viral particles (serotype 2 genome and serotype 6 capsid) were used to express human α-synuclein in the mouse substantia nigra. Gene expression was controlled by the human Synapsin 1 promoter and enhanced using a woodchuck hepatitis virus post-transcriptional regulatory element and a polyA signal downstream to the α-synuclein sequence. AAV-vector production, purification, concentration, and titration were performed by Sirion Biotech (Martinsried, Germany). Mice were treated with a single 1.5 µl injection of $4.0x10^{12}$ genome copies/ml using a stereotaxic frame with a mouse adapter (Stoelting) under isoflurane anaesthesia. Stereotaxic coordinates were 2.3 mm posterior and 1.1 mm lateral to bregma; injection depth was 4.1 mm relative to dura mater. The injection was made at a rate of 0.4µl/min using a Hamilton syringe fitted to a glass capillary. The capillary was left in position for an additional 5 mins before being retracted.
This experiment was performed by Dr. Ayse Ulusoy (DZNE, Bonn).

3.2.8 Image acquisition

3.2.8.1 Imaging of frozen sections

Images of fluorescently stained sections were acquired at an inverted Zeiss AxioObserver Z1 equipped with structured illumination (ApoTome) and a Zeiss AxioCam MRm (Carl Zeiss). At 10X (EC PlnN 10x/0.3, Carl Zeiss) magnification, tile images were acquired with conventional epifluorescence. At 20X (EC PlnN 20x/0.5, Carl Zeiss), 40X (Pln Apo 40x/1.3 Oil, Carl Zeiss) and 63X (Pln Apo 63x/1.4 Oil, Carl Zeiss) magnifications, structured illumination was used to acquire tile images and z-stacks. Some of the images taken with the 20X objective and all the images taken with the 40X and 63X objective are maximum intensity projections of z-stacks. Tile images were stitched with Zen blue software (Zeiss, 2012).

3.2.8.2 Imaging of DAB-stained sections

Brightfield images were visualized with a Zeiss Axio Scope.A1 microscope, collected using AxioCam 503 Color and processed with Zen blue software (Zen lite, 2019).

3.2.8.3 Imaging of sections with RNAScope signal

In situ hybridized sections at adult stages were imaged at an inverted Zeiss AxioObserver equipped with a CSU-W1 Confocal scanner unit (50 μm pinhole disk, Yokogawa). At 40X (C-Apochromat, 40x/1.2 water, Zeiss) magnification, tile images and z-stacks were acquired with laser lines 405 nm, 488 nm and 561 nm. Images taken with the 40X objective are maximum intensity projections of z-stacks. Tile images were stitched with VisiView software (Visitron Systems).

3.2.9 Data analysis

3.2.9.1 TH$^+$ β-gal$^+$ neurons and additional subset markers

The percentage of *Bcl11a*-expressing mDA neurons in SN or VTA at P30 was determined by quantifying TH$^+$ β-gal$^+$ neurons at three rostrocaudal midbrain levels (Franklin & Paxinos, 2007). TH$^+$ β-gal$^+$ neurons in CLi and RRF were analysed separately from neurons in the SN or VTA. The number of TH$^+$ β-gal$^+$ neurons was counted unilaterally in the SN, VTA, RRF and CLi and normalized for the total number of mDA neurons per region separately. The analysis was performed on n=6 *Bcl11a-lacZ* (control) mice and n=6 *Bcl11a* cko^{lacZ} mice. The percentage of *Bcl11a*-expressing mDA neurons co-expressing additional subtype markers

CALB1 and ALDH1A1 in SN or VTA at P30 was determined by quantifying TH^+ β-gal$^+$ neurons at four rostrocaudal midbrain levels (Franklin & Paxinos, 2007). The number of TH^+ β-gal$^+$ neurons co-expressing the respective subset marker in these regions was counted unilaterally and the numbers were normalized for the total number of TH^+ β-gal$^+$ mDA neurons in each region (SN or VTA). This analysis was performed for n=3 *Bcl11a-lacZ* mice and n=3 *Bcl11a* cko^{lacZ} mice.

3.2.9.2 Quantification of CTB-Alexa 488 retrogradely labelled neurons

The percentage of *Bcl11a*-expressing mDA neurons labelled with CTB-Alexa 488 was determined by quantifying $CTB^{+.}$ TH^+ β-gal$^+$ neurons into the SN and VTA and normalizing this number for the total number of CTB labelled neurons in each of the two areas analysed. This analysis was performed on n=3 *Bcl11a-lacZ* mice (P30) unilaterally injected into either the dTS, the NAc or the OT.

3.2.9.3 Stereology

Analyses were performed on SNc samples by an investigator blinded to the sample codes. Unbiased stereological estimates of the number of nigral neurons were obtained by counting under brightfield or confocal microscopy. Samplings were performed on every fifth section throughout the entire SNc. Delineations were made using a 4x objective, and counting was performed using a 63x Plan-Apo oil objective (Numerical aperture=1.4). A guard zone thickness of 1 µm was set at the top and bottom of each section. Cells were counted using the optical fractionator technique (Stereo Investigator software version 9, MBF Biosciences) using a motorized Olympus microscope (IX2 UCB) equipped with an Olympus disk spinning unit (DSU) and a light sensitive EM-CCD camera. Coefficient of error was calculated according to (Gundersen and Jensen 1987); values <0.10 were accepted.
This analysis was performed by Dr. Ayse Ulusoy (DZNE, Bonn).

3.2.9.4 Analysis of TH^+ fiber density

40 µm sections of 3 to 6 rostrocaudal levels of the striatum were stained for TH and epifluorescence images were taken using and inverted Z1 Axioobserver microscope with 10X objective. The mean grey value of the TH^+ striatal projections was calculated in the dorsal striatum, OT and TS (divided into ventral and dorsal TS) with Fiji/ImageJ and normalized for background fluorescence (corpus callosum which is devoid of TH^+ fibres or neurons). This analysis was performed for n=3 control mice and n=3 Bcl11a cko^{lacZ} mice at P30. The same analysis was performed on DAB-stained forebrain sections containing the dorsal striatum and

TS of mice in which α-synuclein was overexpressed in the SNc. In this case, the mean grey value of the injected side was compared to the mean grey value calculated on the intact side. This analysis was performed for n=4 control and n=3 cko mice of the adult experimental group and n=3 control and n=4 cko mice of the aged experimental group.

3.2.10 Images analysis for axon terminals mapping

The hemispheric images of the striatal region obtained from intersectional fate mapping experiments (see section 3.2.1.3) were aligned at five rostral-to-caudal Bregmas (1.42 mm, 0.95 mm, 0.62 mm, -0.15 mm and -0.58 mm) for each one of the analysed mice. The TH staining was converted to greyscale and the EGFP fluorescence signal showing Bcl11a-expressing mDA neurons projections was converted to a binary file, after background subtraction. Binary files from each mouse were assigned a different colour of choice and superimposed on their correspondent TH staining to produce the results shown in Figure 16A.

3.2.11 Analysis of Bcl11a-expressing mDA neurons starter population labelled with intersectional fate mapping experiments

To assess the distribution of TH$^+$ EGFP$^+$ neurons labelled with the intersectional fate mapping approach, the SN and the VTA were divided into subregions and the number of double labelled cells was quantified for each one of the subregions. The SN was divided into medial SN (m_SN), lateral SN (l_SN) and substantia nigra pars lateralis (SNl). The VTA was divided into parabrachial pigmented nucleus (PBP), paranigral nucleus (PN) and interfascicular nucleus (IF). The above described analysis was performed at four different rostrocaudal levels of the midbrain.

3.2.12 Behavioural tests

Male mice were kept ad libitum in groups of 2-3 animals in a 12-hour day/night rhythm on a normal diet. The animals were transferred to the examination room for experimental purposes and each one was housed in a separate cage. After a one-week acclimation period in the examination room, mice performed the RotaRod test and beam walking assay (both tests in one day) for five consecutive days, followed by the social recognition test and the open-field test. After 30 days of rest from the initial test run, another test run was performed for the open-field, the social recognition test and the beam walking assay.

3.2.12.1 RotaRod test

The animals were taken out of the cage and were acclimated to the Rotarod apparatus (Ugo Basile) in a 5-minute run on a rod rotating at a constant speed of 8 rpm. Afterwards the animals went through three test runs per day, with a break of 30 min between each run. In each test run, the animals had to balance on the rotating rod for 5 min, whereby the torque increased from 4 to 40 rpm within 5 min. The duration that each mouse was able to stay on the rotating rod in each trial was recorded as the latency to fall. The three test runs per day were repeated on 5 consecutive days. During the test, the rod was kept clean and dry by wiping the mouse urine and faeces off.

3.2.12.2 Beam Walking Assay

To examine fine motor skills independent of rotational movement (Luong et al., 2011), animals had to balance from one platform over a 12 mm wide and 1 m long wooden rod to another platform that held a box with a food reward. The time taken for the animals to cross the bar and the number of times the animals missed the bar with their hind legs during the run is a good measure of the motor skills of mice. This test was initially run for a training period of 5 days, then after a 30-day rest period, another test run was performed to check the memory performance of the animals.

3.2.12.3 Open-field test

In the open-field test, the mice were placed in an open arena (30 x 30 x 30 cm). They were allowed to move freely for 5 minutes. The animals were recorded by Video (Noldus, EthovisionXT) and the running distance, the time spent in the border area, the corners and the centre of the cage as well as crossings from the border to the centre area were measured.

3.2.12.4 Social recognition test

For the social recognition test, the animals were first accustomed to the examination room as described above. On the test day the mice were put into a cage with three compartments. The middle compartment was empty, in the right and left compartment there was a small cage of 10 cm^2 floor space, in which a familiar or unfamiliar mouse was sitting, depending on the test conditions. The test animals were placed in the middle compartment and their movements were digitalized for 10 min by video recordings (Noldus, EthovisionXT). Afterwards, the video recordings were evaluated according to the probability of stay in the cage compartments, the number of contacts and the distance travelled. Duration of time spent in each chamber for

every condition (empty chamber or chamber with intruder mice), as well as distance moved was assessed. The duration of time spent around cages with familiar and stranger mouse was assessed, as well as transitions between familiar and stranger mouse.

3.2.13 Statistical analysis

3.2.13.1 Statistical analysis of cell body quantification

Statistical analyses of cell numbers were done with GraphPad Prism (8.0) software using ANOVA followed by Šídák's multiple comparison test, one-way ANOVA followed by test for linear trend, Welch's ANOVA followed by Dunnett's T3 multiple comparison test or one-way ANOVA followed by Tukey's *post hoc* test for multiple comparisons.
P values of less than 0.05 were considered statistically significant. Data are reported as mean values ± standard error of the mean (SEM).

3.2.13.2 Statistical analysis of TH positive fibres intensity

Statistical analyses of TH positive fibre intensity were done with GraphPad Prism (8.0) software using unpaired t-test or ordinary one-way ANOVA followed by Tukey's *post hoc* test for multiple comparisons.
P values of less than 0.05 were considered statistically significant. Data are reported as mean values ± standard error of the mean (SEM).

3.2.13.3 Statistical analysis of behavioural experiments

Statistical analyses of behavioural experiments were done with R studio through a collaboration with Prof. Dr. Stephan Baader.
Open field tests were evaluated by one-way analysis followed by Tukey's post hoc test for multiple comparisons. Differences in the balanced beam test and rotarod were assessed by two-way ANOVA taking time and genotype as numerical and categorical variables. Social recognition test was evaluated by Levene test for homogeneity of data and two-way ANOVA taking genotype and either chambers, cages or setup as numerical and categorical variables. P values of less than 0.05 were considered statistically significant. Data are reported as mean values ± standard error of the mean (SEM).

4. RESULTS

4.1 BCL11A is expressed in a subset of SN, VTA, CLi and RRF mDA neurons

Bcl11a was initially identified as a potential marker for a subset of mDA neurons based on its expression pattern available on the Allen Brain Atlas (Developing Mouse Brain).
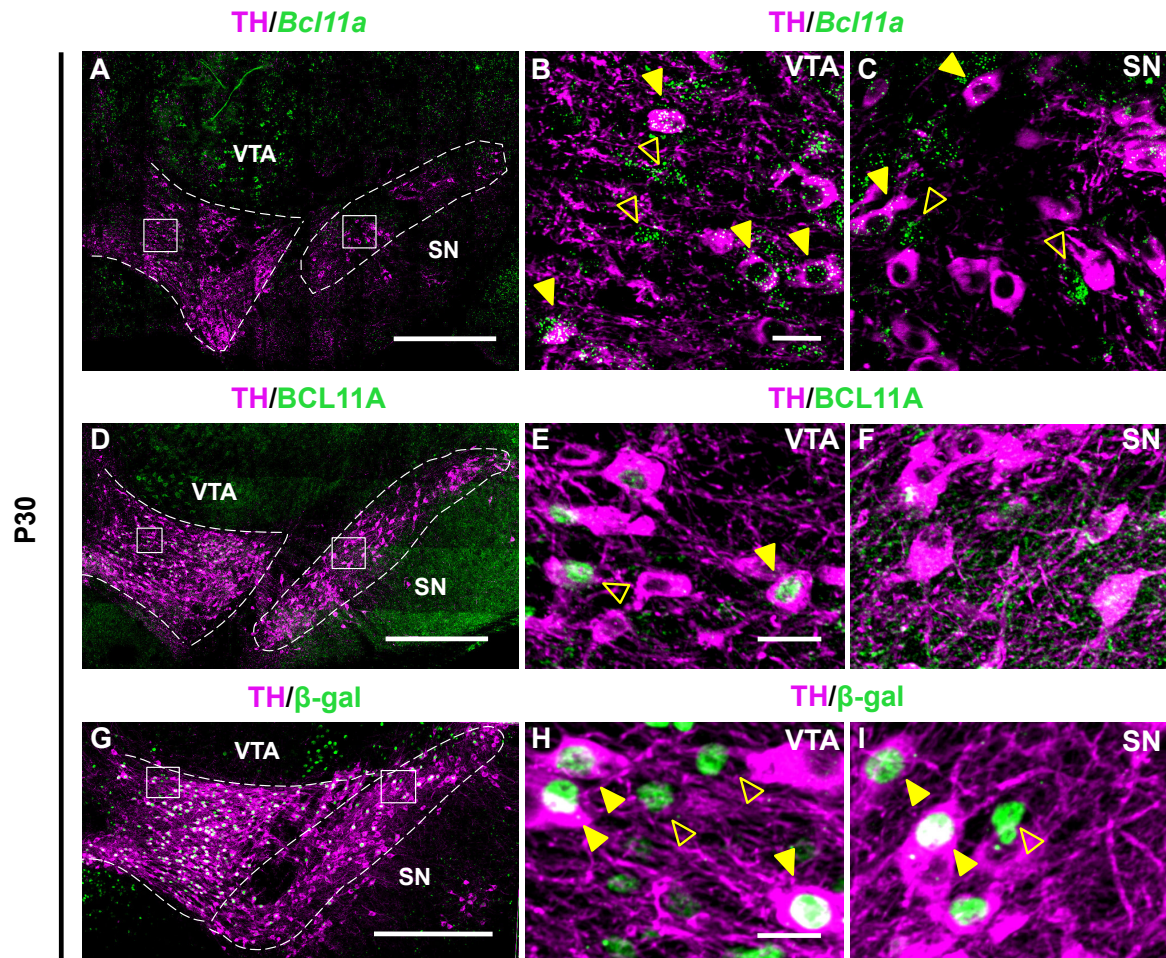

Figure 4. *Bcl11a*-**expressing mDA neurons in the adult ventral midbrain. (A-C)** Multiplex fluorescent *in situ* hybridization for *Bcl11a* mRNA and immunofluorescent staining for TH on P30 coronal sections (experiments performed by Khondker Ushna Sameen Islam). **(B,C)** Higher magnification of the boxed areas in A. **(D-F)** Immunofluorescent staining for BCL11A and TH on P30 coronal sections. **(E-F)** Higher magnification of the boxed areas in D. The immunostaining for BCL11A failed to detect the protein in the SN. **(G-I)** Immunofluorescent staining for β-gal and TH on coronal sections of P30 *Bcl11a-lacZ* mice. Filled arrowheads indicate cells that are double positive for *Bcl11a*/BCL11A/β-gal and TH, empty arrowheads indicate cells that express *Bcl11a*/BCL11A/β-gal but are TH negative. Scale bars: 500 µm **(A,D,G)**, 25 µm **(B,C,E,F,H,I)**.

To examine if *Bcl11a*/BCL11A is indeed expressed in a subpopulation of mDA neurons, *Bcl11a* mRNA expression was initially analysed in combination with TH, the rate limiting enzyme in dopamine synthesis **(Figure 4A-C,** experiments performed by Khondker Ushna

Sameen Islam**)**. In the adult brain, a subset of mDA neurons in the SN, VTA, CLi and RRF was expressing *Bcl11a* mRNA. In the VTA, *Bcl11a*-expressing mDA neurons were found distributed throughout the VTA. *Bcl11a*-positive mDA neurons in the SN were located in the medial and dorsal SNc, as well as in the more lateral SNl. When compared to *Bcl11a*-expressing mDA neurons in the VTA, SN-mDA neurons showed a lower density of fluorescent dots within the TH positive cells, thus indicating lower levels of *Bcl11a* mRNA **(Figure 4A-C)**. These data were also confirmed in the neonatal brain (data not shown)**.** Next, the expression of BCL11A protein in combination with TH was analysed in the adult brain **(Figure 4D-F)**. Within the VTA the distribution of cells that were double positive for BCL11A protein and TH was comparable to the distribution of TH positive cells expressing *Bcl11a* mRNA. *Bcl11a* mRNA expression data could not be confirmed in the SN of adult brains, since we were not able to detect BCL11A protein in mDA neurons of the SNc and SNl **(Figure 4D-F)**. Since *Bcl11a* mRNA levels are lower in SN-mDA neurons when compared to the VTA, SN-mDA neurons likely express lower protein levels that may not detected by the anti-BCL11A antibody that we used for our study. BCL11A protein expression data were also confirmed in the neonatal brain (data not shown).
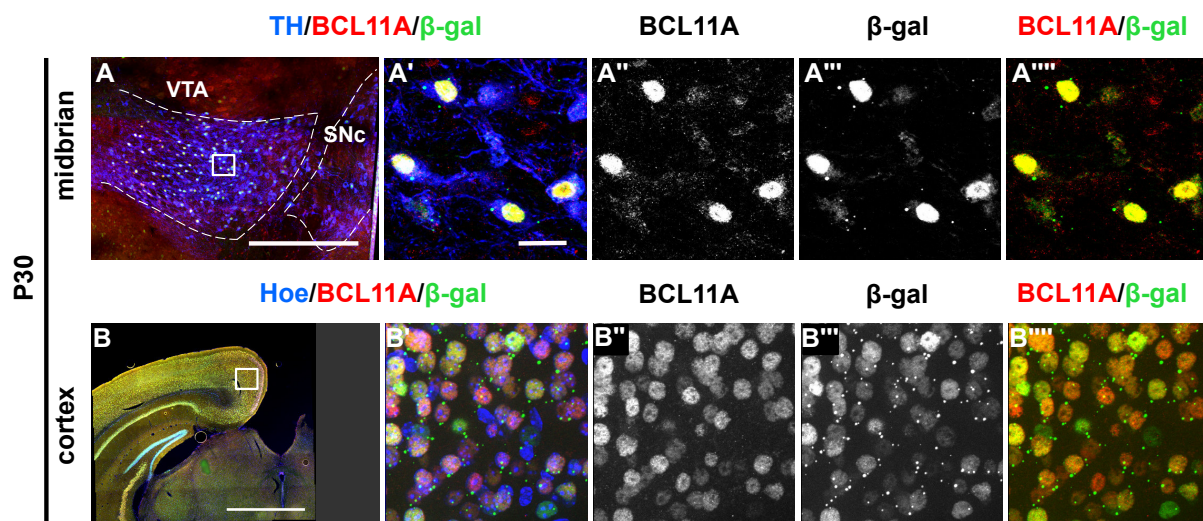

Figure 5. Expression pattern of β-gal and BCL11A largely overlaps in the VTA and in the cerebral cortex of adult *Bcl11a-lacZ* mice. (A-A'''') Triple immunofluorescent staining for TH (blue), BCL11A (red) and β-gal (green) in the ventral midbrain of P30 *Bcl11a-lacZ* mice. **(A'-A'''')** Higher magnification of the boxed area in A. **(B-B'''')** Triple immunofluorescent staining for Hoechst (blue), BCL11A (red) and β-gal (green) in the cerebral cortex of P30 *Bcl11a-lacZ* mice. **(B'-B'''')** Higher magnification of the boxed area in B. Scale bars: 500 μm **(B,D)**, 25 μm **(A'-A'''',B'-B'''')**.

Since the BCL11A antibody might not be able to label all the *Bcl11a*-expressing mDA neurons (e.g neurons in the SNc), a different approach needed to be used in order to visualize cells with a Bcl11a identity. Therefore, the distribution of Bcl11a-expressing mDA neurons was analysed in *Bcl11a^{lacZ}* mice. In this mouse line, the β-gal expression is restricted only to cells

that express *Bcl11a* thanks to the *lacZ* allele being knocked into the endogenous *Bcl11a* locus (Dias et al., 2016). β-gal-expressing mDA neurons were found throughout the VTA, as well as in the medial and dorsal SNc and in the SNl **(Figure 4G-I)**. Therefore, the distribution of β-gal-positive mDA neurons was comparable to the one of mDA neurons expressing *Bcl11a* mRNA in both VTA and SN. To assess whether the β-gal expression reliably reflects the endogenous BCL11A expression, thus marking BCL11A-expressing neurons, a double labelling for β-gal and BCL11A was performed in adult sections of the midbrain **(Figure 5A-A'''')**. The expression pattern of β-gal and BCL11A was largely overlapping in the VTA. The overlap between β-gal and BCL11A expressing cells was also observed in adult sections of the cerebral cortex **(Figure 5B-B'''')**. The overlap between β-gal and BCL11A in the midbrain as well as in the cortex was largely confirmed in the neonatal brain (data not shown). Using the *Bcl11a^{lacZ}* line, the percentage of mDA neurons expressing *Bcl11a* was quantified by counting cells that were double positive for β-gal and TH in the adult brain. For this purpose, three rostrocaudal levels of the midbrain containing VTA and SN were analysed. A more caudal midbrain level was used to analyse the β-gal expression in mDA neurons of the CLi and RRF **(Figure 6A-F'')**. In the VTA, 42.84% +/- 1.326 mDA neurons expressed β-gal. When analysed in the SN, β-gal expression was restricted to 22.63% +/- 21.79 mDA neurons. β-gal was also expressed in 32.61 +/- 1.933 CLi- and 30.97% +/- 2.757 RRF-mDA neurons **(Figure 6G)**. These results were largely confirmed at a neonatal stage. β-gal expression was also found in non-DA cells within the SN, VTA, RRF and CLi. Specifically, 53.81% +/- 3.329 β-gal neurons were TH negative in the SN, 49.89% +/- 3.747 β-gal neurons were TH negative in the VTA, 50.05% +/- 3.552% β-gal neurons were TH negative in the RRF and 61.78% +/- 4.595% β-gal neurons were TH negative in the CLi **(Figure 6H)**. Moreover, non-DA neurons positive for β-gal were also found in the ventral midline of the midbrain and rostral to the SN **(Figure 6C-F'')**.

To analyse the time course of BCL11A expression in the ventral midbrain during development, immunostaining for BCL11A protein was performed between embryonic day E12.5 and E15.5 **(Figure 7,** experiments performed by Dr. Gabriela Oana Bodea**)**. At E12.5, BCL11A was mainly localized in the area below the mDA progenitor domain and in some differentiated mDA neurons expressing TH **(Figure 7A-A'')**. At E14.5 and E15.5, BCL11a was expressed in a larger subpopulation of mDA neurons of the forming SN and VTA **(Figure 7B-E'')**.
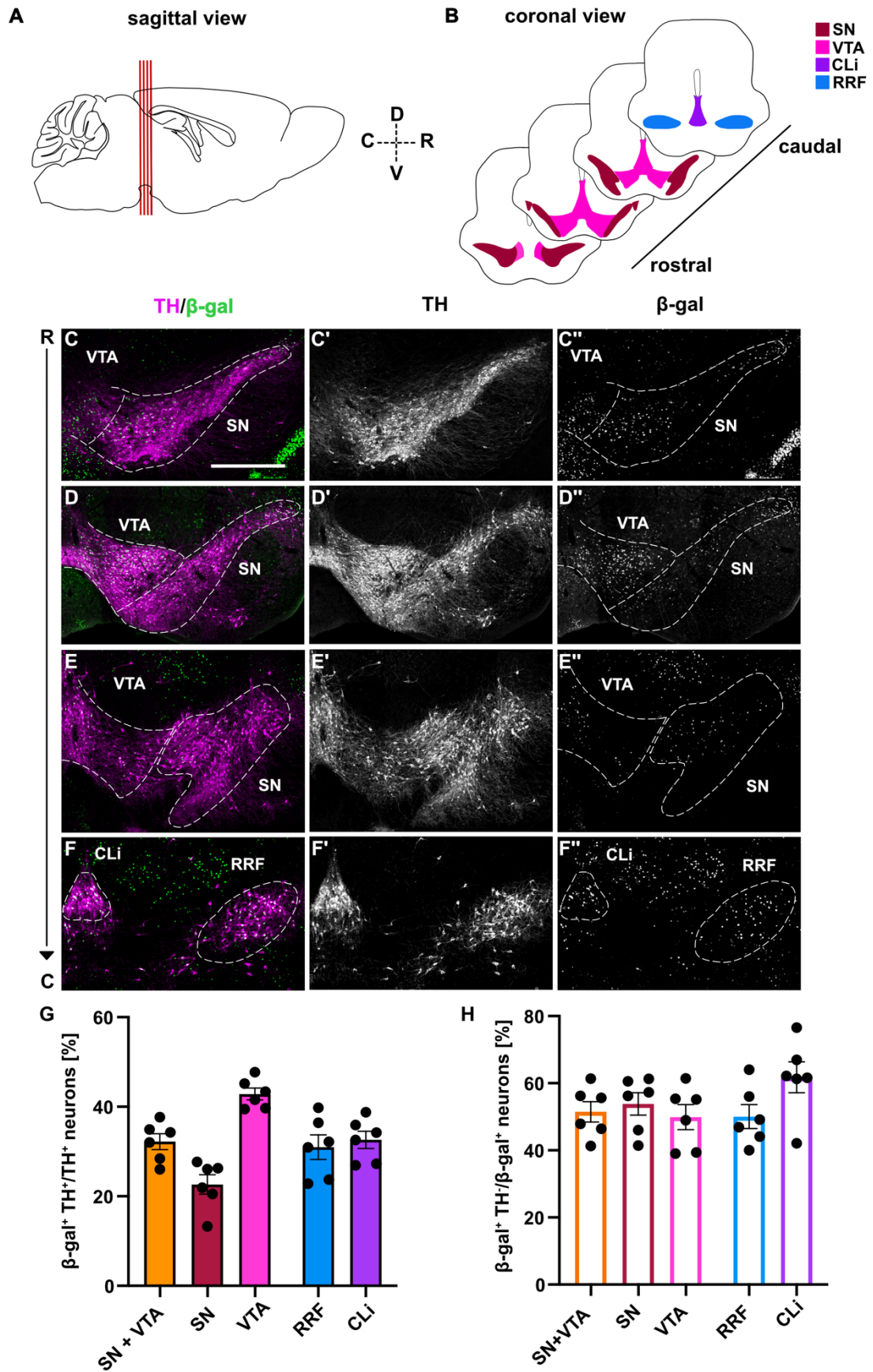
Figure 6. (Figure legend on next page)

Figure 6. *Bcl11a* is expressed in a subset of SN, VTA, CLi and RRF neurons. **(A)** Schematic of a sagittal section through the adult mouse brain. Red lines indicate the rostrocaudal levels of the coronal sections shown in B. **(B)** Schematic of coronal rostrocaudal levels of the adult ventral midbrain shown in C-F''. **(C-F'')** Immunofluorescent staining for β-gal and TH on coronal sections at different rostrocaudal levels of *P30 Bcl11a-lacZ* mice. *Bcl11a*-expressing mDA neurons were found throughout the VTA, except for the most medial regions **(C-E'')**. *Bcl11a*-expressing mDA neurons of the SN are mainly located in the medial SNc (rostral levels) and the dorsal tier of the SNc (more caudal sections) and in the SNl **(C-E'')**. *Bcl11a*-expressing mDA neurons are also located in the CLi and RRF **(F-F'')**. **(G)** Percentage of TH-expressing neurons that are positive for β-gal in *Bcl11a-lacZ* mice at P30 (n=6 mice). Note that rostrocaudal levels shown in C-F'' were selected for each mouse to perform this analysis. *Bcl11a*-expressing neurons that are TH negative were found throughout the midbrain of *P30 Bcl11a-lacZ* mice **(C-F'')**. **(H)** Percentage of *Bcl11a*-expressing neurons that are TH negative in *Bcl11a-lacZ* mice at P30 (n=6 mice). Error bars indicate mean +/- SEM. Scale bar: 500 μm **(C-F'')**.

Taken together, these data show that *Bcl11a* expression defines a subset of mDA neurons in the VTA, SN, CLi and RRF in the developing and adult brain.
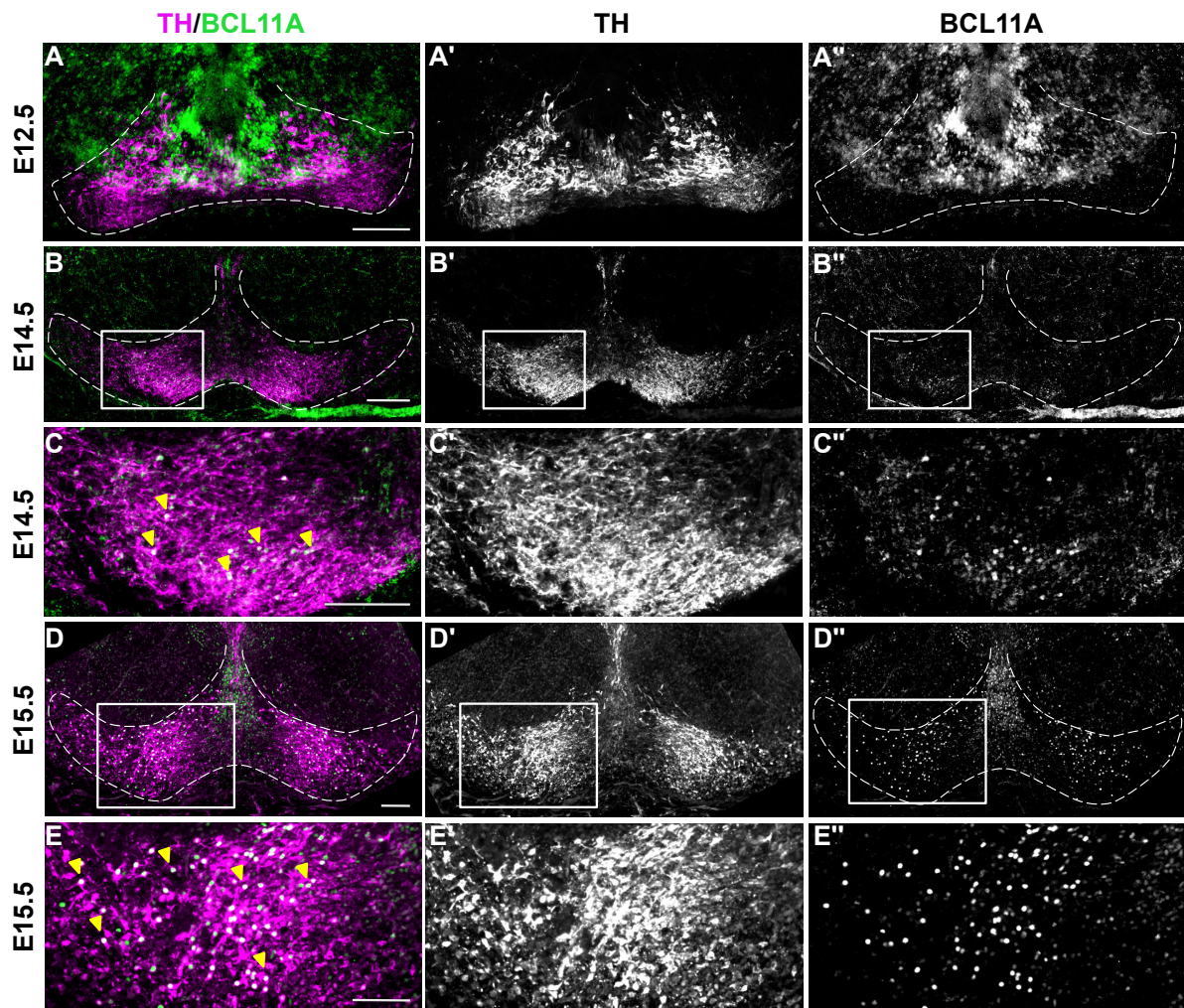

Figure 7. *Bcl11a* expression in the midbrain starts at E12.5. (A-E'') Immunofluorescent staining for BCL11A and TH on E12.5 **(A-A'')**, E14.5 **(B-C'')** and E15.5 **(D-E'')** coronal sections of the ventral midbrain (experiments performed by Dr. Gabriela Oana Bodea). **(C-C'', E-E'')** Higher magnification of the boxed area in B-B'', D-D''. Arrowheads indicate cells that are double positive for BCL11A and TH. Scale bar: 100 μm **(A-E'')**.

4.2 *Bcl11a*-expressing mDA neurons contribute to several known subpopulations of mDA neurons

Several subtype markers are known to label specific subtypes of mDA neurons, like CALB1 and ALDH1A1 (Liu et al., 2014; Poulin et al., 2014). In the SNc, CALB1 and ALDH1A1 expression defines complementary domains. CALB1 expression is restricted to the dorsal tier and ALDH1A1 to the ventral tier of the SNc. CALB1 expression is found throughout the VTA, while ALDH1A1-expressing mDA neurons are mainly located in the ventral VTA (Thompson, 2005; Wu et al., 2019).

Since *Bcl11a*-positive mDA neurons were found in both SN and VTA, *Bcl11a* expression was next analysed in combination with CALB1 and ALDH1A1, to understand if the *Bcl11a*-expressing mDA subpopulation falls within one of these previously characterized subclasses. This analysis was performed using adult brains of *Bcl11a-lacZ* mice on which immunostainings for TH, β-gal and the respective subtype marker were performed **(Figure 8A-D)**. Triple immunostaining for TH, β-gal and CALB1 revealed that at P30, 45.18% +/- 5.903% of *Bcl11a*-expressing mDA neurons in the SN co-expressed CALB1. Therefore, even though *Bcl11a*-expressing mDA neurons are mainly found in the dorsal tier of the SNc (see Figure 3), which is characterized by CALB1 expression, less than half of them co-express CALB1 at this stage. In the VTA, 71.09% +/- 6.018% of *Bcl11a*-expressing mDA neurons co-expressed CALB1 **(Figure 8E)**. Triple immunostaining for TH, β-gal and ALDH1A1 showed that 19.76% +/- 1.342% of *Bcl11a*-positive neurons in the SN and 20.70% +/- 3.337% in the VTA co-expressed ALDH1A1 **(Figure 8F)**.

These data show that the *Bcl11a*-expressing mDA neurons do not clearly fall within these previously defined mDA subgroup, thus representing a previously uncharacterized subpopulation of mDA neurons.
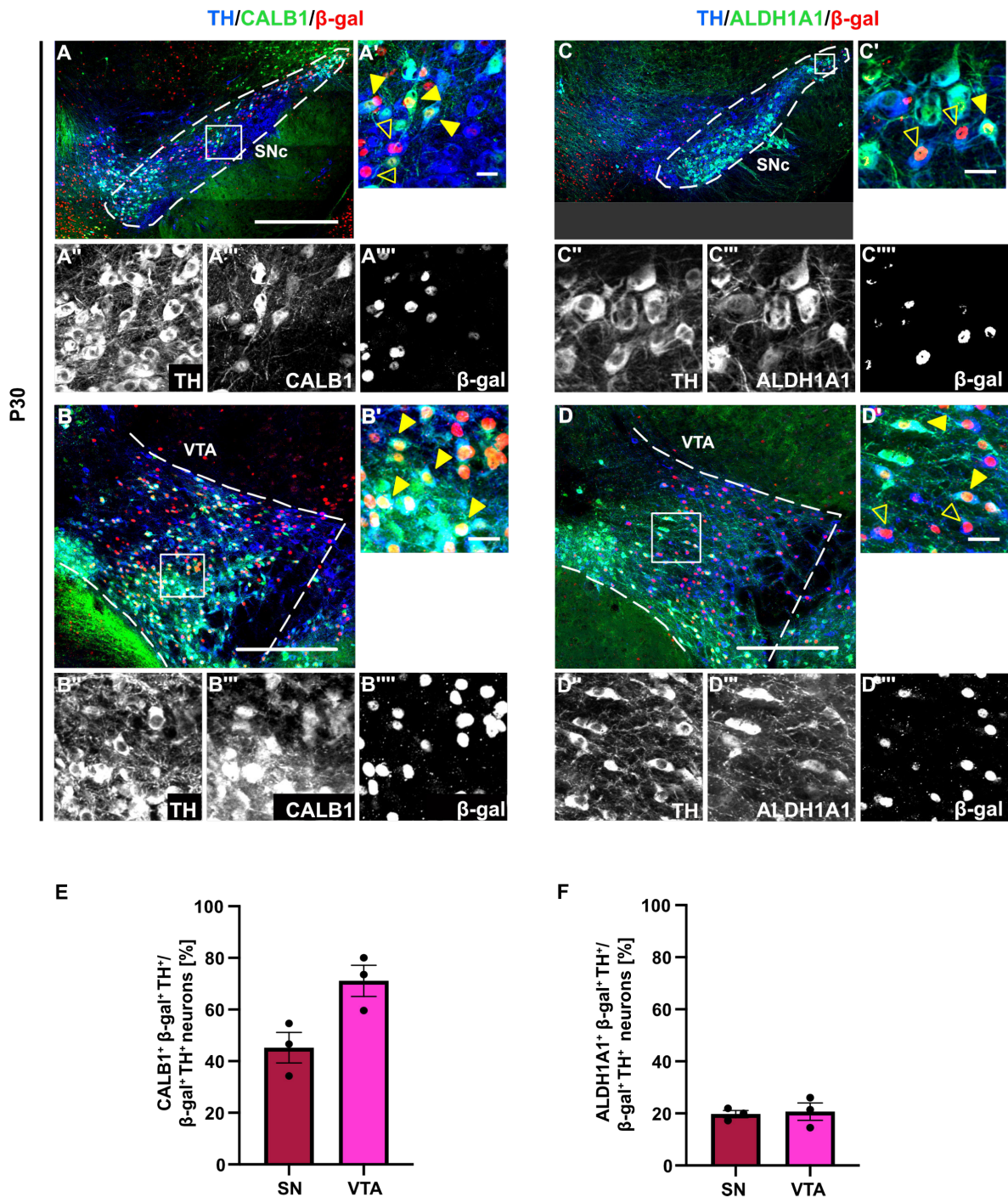
Figure 8. *Bcl11a*-**expressing mDA neurons are a distinct mDA subset that does not correspond to previously defined mDA neuronal subpopulations. (A,B)** Triple immunostaining for TH (blue), β-gal (red) and CALB1 (green) in the SN **(A-A'''')** and VTA **(B-B'''')** of P30 *Bcl11a-lacZ* mice. **(A'-A'''',B'-B'''')** Higher magnification of the boxed area in A,B. **(C,D)** Triple immunostaining for TH (blue), β-gal (red) and ALDH1A1 (green) in the SN **(C-C'''')** and VTA **(D-D'''')** of P30 *Bcl11a-lacZ* mice. **(C'-C'''',D'-D'''')** Higher magnification of the boxed area in C,D. Filled arrowheads indicate TH[+] β-gal^{+} cells expressing the respective subset markers, unfilled arrowheads indicate TH[+] β-gal^{+} cells negative for the respective subset marker. **(E-F)** Percentage of TH[+] β-gal^{+} neurons that are positive for the respective subset marker at P30. Mice analysed (n=3 mice). Scale bars: 500 µm **(A,B,C,D),** 25 µm **(A'-A'''',B'-B'''',C'-C'''',D'-D'''')**.

4.3 *Bcl11a*-expressing neurons form a subcircuit in the dopaminergic system

4.3.1 Bcl11a-CreER mediated recombination pattern in mDA neurons

To understand whether the mDA neurons subset expressing *Bcl11a* contributes to specific subcircuits within the mDA system, the first step was to establish a method to label neurons expressing *Bcl11a*. For this purpose, a *Bcl11a^{CreER}* mouse line was used (Pensa et al., under revision). In this line, the DNA sequence required for IRES (internal ribosomal entry site) and CreER (Cre recombinase fused with a modified form of the human estrogen receptor) was inserted together with a neomycin cassette (neo) in the exon 4 of the *Bcl11a* gene **(Figure 9)**. In order to validate the line, *Bcl11a^{CreER}* mice were crossed with a TdTomato-expressing reporter mouse line (*Rosa$^{loxP\text{-}STOP\text{-}loxP\text{-}tdtomato}$* or *Ai9*; Madisen et al., 2010). The *Rosa$^{loxP\text{-}STOP\text{-}loxP\text{-}tdtomato}$* reporter mouse line requires CreER-mediated recombination to excise a stop codon preceding the TdTomato sequence, resulting in TdTomato labelling of CreER expressing cells **(Figure 9)**. CreER was activated during embryogenesis through the administration of Tamoxifen to pregnant females at E15.5 **(Figure 9)**. To assess the CreER mediated recombination pattern in mDA neurons, females were sacrificed three days after Tamoxifen administration at E18.5 and brains of *Bcl11a$^{CreER/+}$, Rosa$^{loxP\text{-}STOP\text{-}loxP\text{-}tdtomato/+}$* embryos were dissected and analysed **(Figure 10A)**.
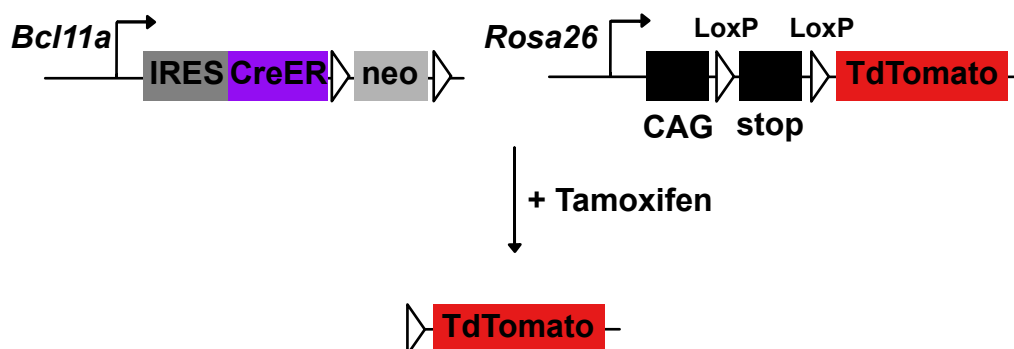

Figure 9. Transgenic mouse lines used to analyze CreER-mediated recombination under the *Bcl11a* promoter in the ventral midbrain. A *Bcl11a^{CreER}* mouse line was used in combination with a reporter mouse line. The *Rosa26* reporter allele contains a floxed STOP cassette upstream of tdTomato. Only after the CreER is activated by Tamoxifen administration, TdTomato is expressed in cells positive for CreER.

To check whether the labelling of *Bcl11a*-expressing neurons with TdTomato was successful in the ventral midbrain, E18.5 embryonic brains were stained for the mDA neurons marker TH and the red fluorescent protein TdTomato **(Figure 10B-E'')**. Neurons double positive for TH and TdTomato were found throughout different rostro-caudal level of the midbrain, in both SN

and VTA **(Figure 10B-E'')**. As expected, since *Bcl11a* expression is not restricted to mDA neurons only (see also Figure 6), TdTomato positive cells that are negative for TH were also found throughout the VTA, in the SN and in the area just below the VTA **(Figure 10B-E'')**.
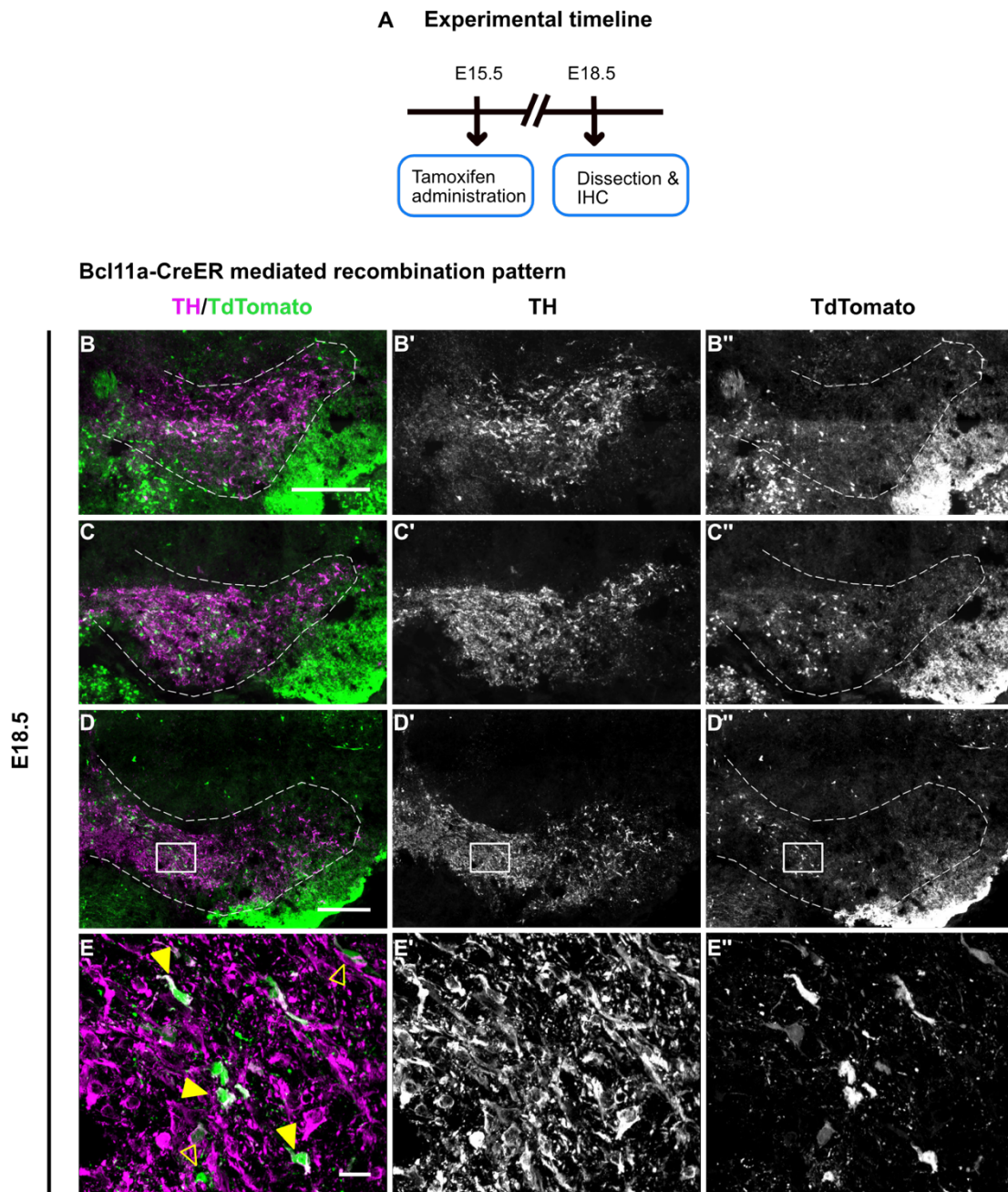

Figure 10. Bcl11a-CreER mediated recombination pattern in the ventral midbrain. (A) Schematic showing the experimental timeline. Tamoxifen was administered to pregnant mice at embryonic day E15.5. Brains were dissected and analysed at E18.5. **(B-E'')** Immunofluorescent staining for TH and TdTomato showing the Bcl11a-CreER mediated recombination in the ventral midbrain of E18.5 embryos. **(E-E'')** Higher magnification of the boxed area in E-E''. Filled arrowheads indicate mDA neurons expressing *Bcl11a* (TdTomato positive), empty arrowheads indicate *Bcl11a*-expressing neurons (TdTomato positive) that are TH negative. Scale bars: 200 µm **(B-C'')**, 100 µm **(D-D'')** and 25 µm **(E-E'')**.

These data show that the *Bcl11a^CreER* mouse line is a valid tool to label *Bcl11a*-expressing neurons in the ventral midbrain. However, to be able to specifically label only *Bcl11a*-expressing mDA neurons (and not other type of *Bcl11a*-expressing cells) a different approach needs to be used.

4.3.2 Intersectional fate mapping strategy to label *Bcl11a*-expressing mDA neurons and their projections

To specifically label *Bcl11a*-expressing mDA neurons and investigate their projections we used an intersectional genetic approach. This strategy combines a reporter allele in which expression of a fluorescent reporter protein is driven by a tetracycline response element (TRE), but is also Cre-dependent (Madisen et al., 2015; Poulin et al., 2018). To activate the reporter allele in mDA neurons we used a *Dat^tTa* (tetracycline trans-activator driven by the *Dat* promoter) mouse line in conjunction with the *Bcl11a^CreER* mouse line and the intersectional reporter mouse line Ai82D (Madisen et al., 2015) **(Figure 11)**.
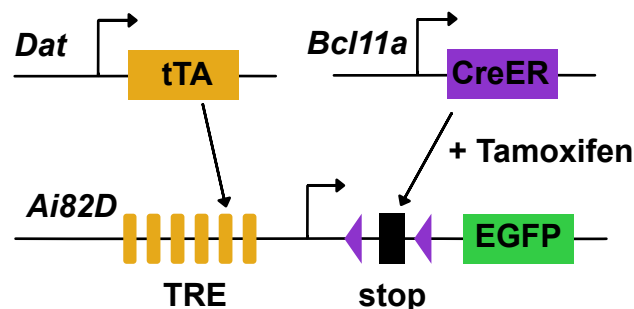

Figure 11. Intersectional fate mapping approach to specifically label *Bcl11a*-expressing mDA neurons and their projections. Schematic showing the intersectional fate mapping strategy. A *Bcl11a^CreER* mouse line was used in combination with *Dat^tTA* mice and an intersectional reporter mouse line (*AI82D)*. EFGP is expressed only in cells positive for both CreER and tTa and only after CreER is activated by administration of Tamoxifen.

CreER was activated during embryogenesis by Tamoxifen administration to pregnant females at E15.5 **(Figure 12A)**, since *Bcl11a* is already expressed in a subset of mDA neurons at this developmental stage **(**see **Figure 7)**. Initially, the distribution of recombined EGFP positive neurons and their projections to the striatal area were analysed in E18.5 embryonic brains. In the VTA, recombined neurons were found throughout the VTA at different rostrocaudal levels of the ventral midbrain **(Figure 12B-D'')**. In the SN, EGFP positive neurons were found in the medial and dorsal SNc and also in the more lateral SNl **(Figure 12B-D'')**.
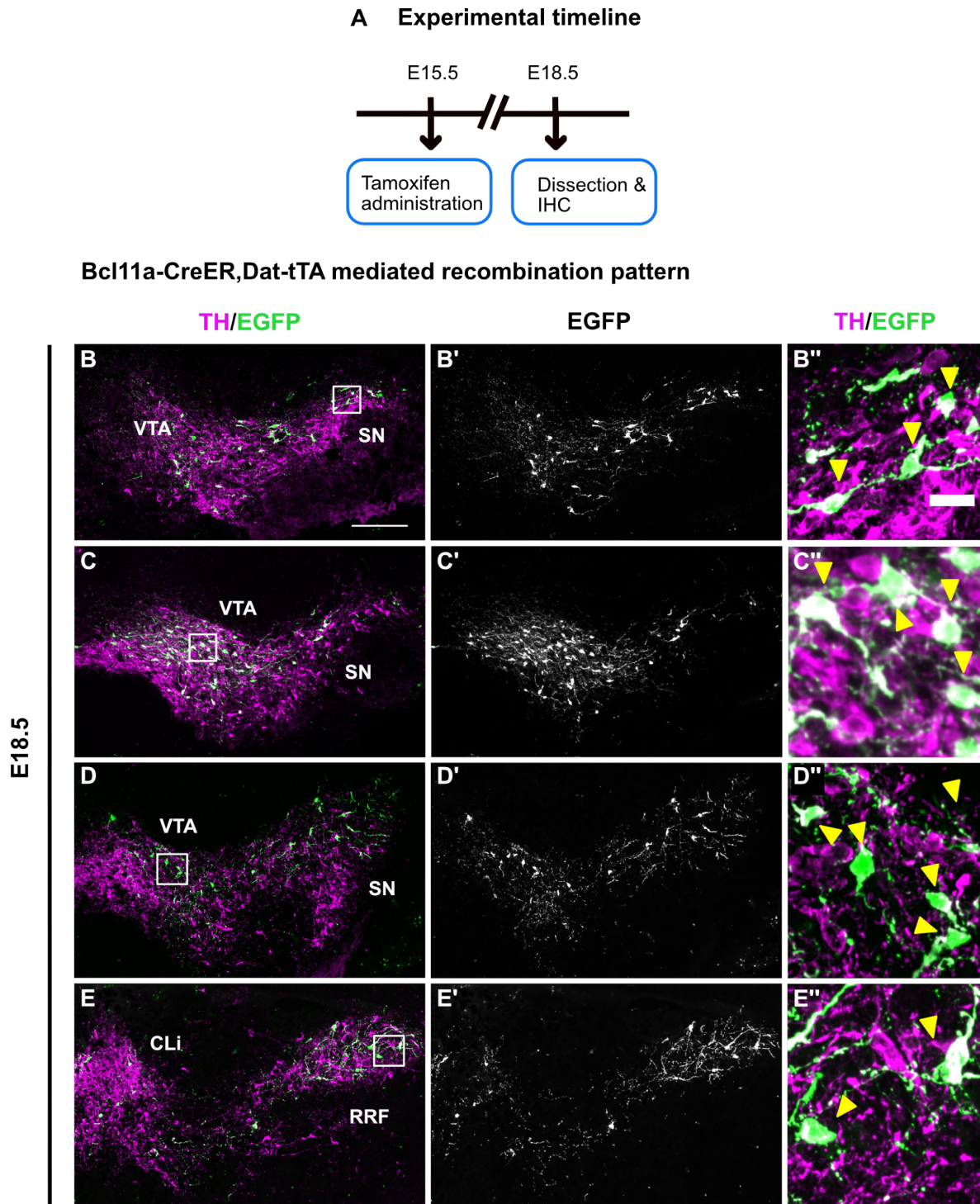
Figure 12. Distribution of recombined neurons using the intersectional fate mapping approach in the embryonic brain at E18.5. (A) Schematic showing the experimental timeline. Tamoxifen was administered to pregnant mice at embryonic day E15.5. Brains were dissected and analysed at E18.5. **(B-E'')** Immunofluorescent staining for TH and EGFP on coronal sections of the midbrain at E18.5. Recombined neurons were found in the VTA and SN **(B-D'')** as well as in the CLi and RRF **(E-E'')**. (A'',B'',C'',D'') Higher magnification of the boxed area in A, B, C and D. Mice analysed (n=4 mice). Scale bars: 200 µm **(B-E)** and 25 µm **(B''-E'')**.

Recombined neurons were also found in the Cli and RRF **(Figure 12E-E'')**. Of note, the EGFP expression was restricted to mDA neurons only. To investigate whether the *Bcl11a*-expressing

subset of mDA neurons contributes to specific subcircuits in the mDA system, EGFP positive fibres labelled with the intersectional fate mapping approach were analysed.
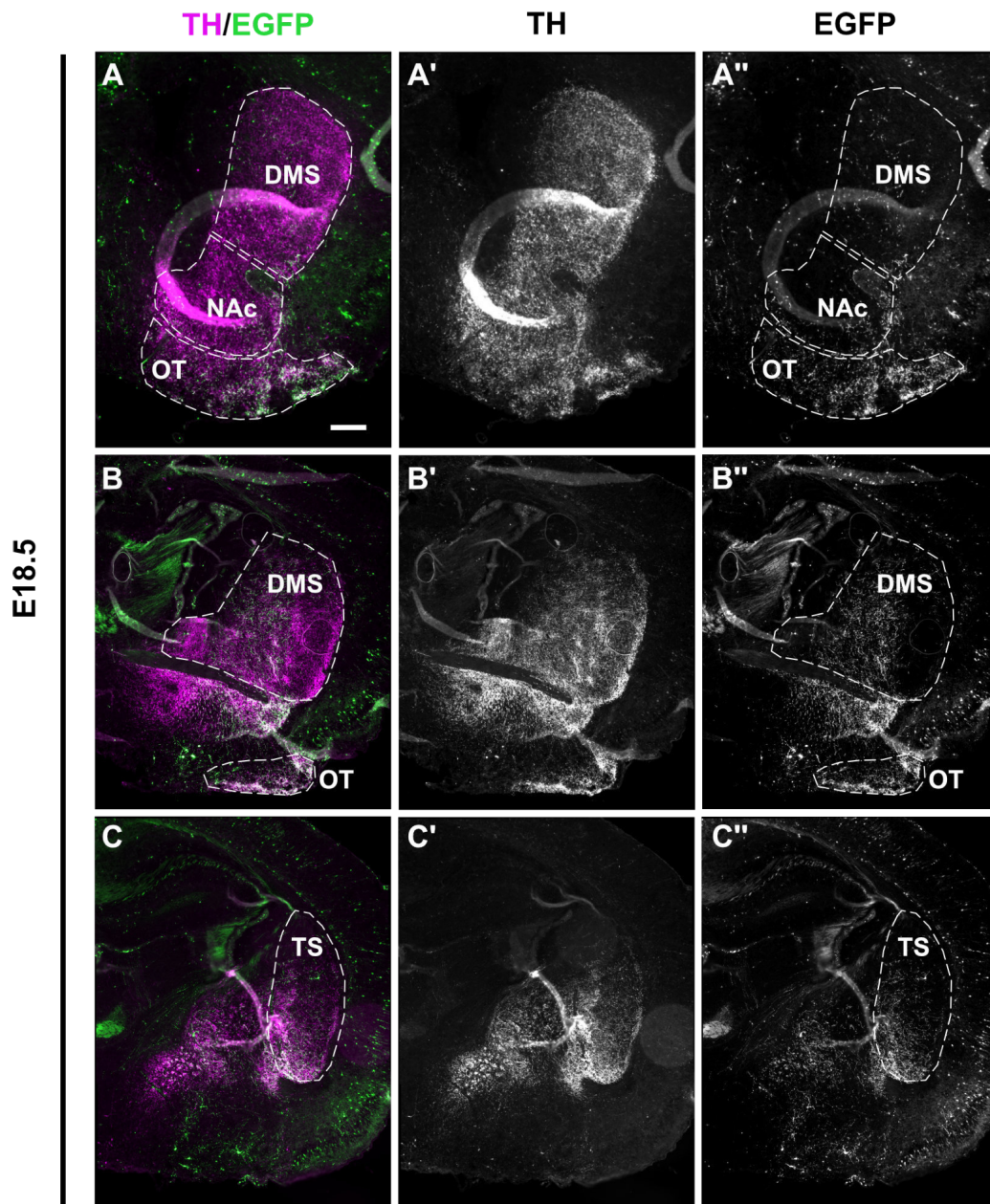

Figure 13. Projections of *Bcl11a*-expressing mDA neurons to the striatal region at E18.5. (A-C'') Immunostaining for TH and EGFP in rostrocaudal levels of the striatal region showing that *Bcl11a*-expressing mDA neurons innervate specific subdomains of DA projection targets including the olfactory tubercle (OT, **A-B''**), the dorsomedial striatum (DMS, **B-B''**) and the tail of the striatum (TS, **C-C''**). Mice analysed (n=4 mice). Scale bar: 500 μm **(C-F'')**. Scale bar: 200 μm **(A-C'')**.

In target areas of VTA mDA neurons (Morales & Margolis, 2017), the strongest innervation established by *Bcl11a*-expressing mDA neurons was found in the olfactory tubercle (OT) **(Figure 13A-B'')**. At this stage very few EFGP positive fibres were found in the ventral and lateral NAc **(Figure 13A-A'')**.

A   Experimental timeline

E15.5   P30

Tamoxifen administration

Perfusion & IHC

B

D
R – – – C
V

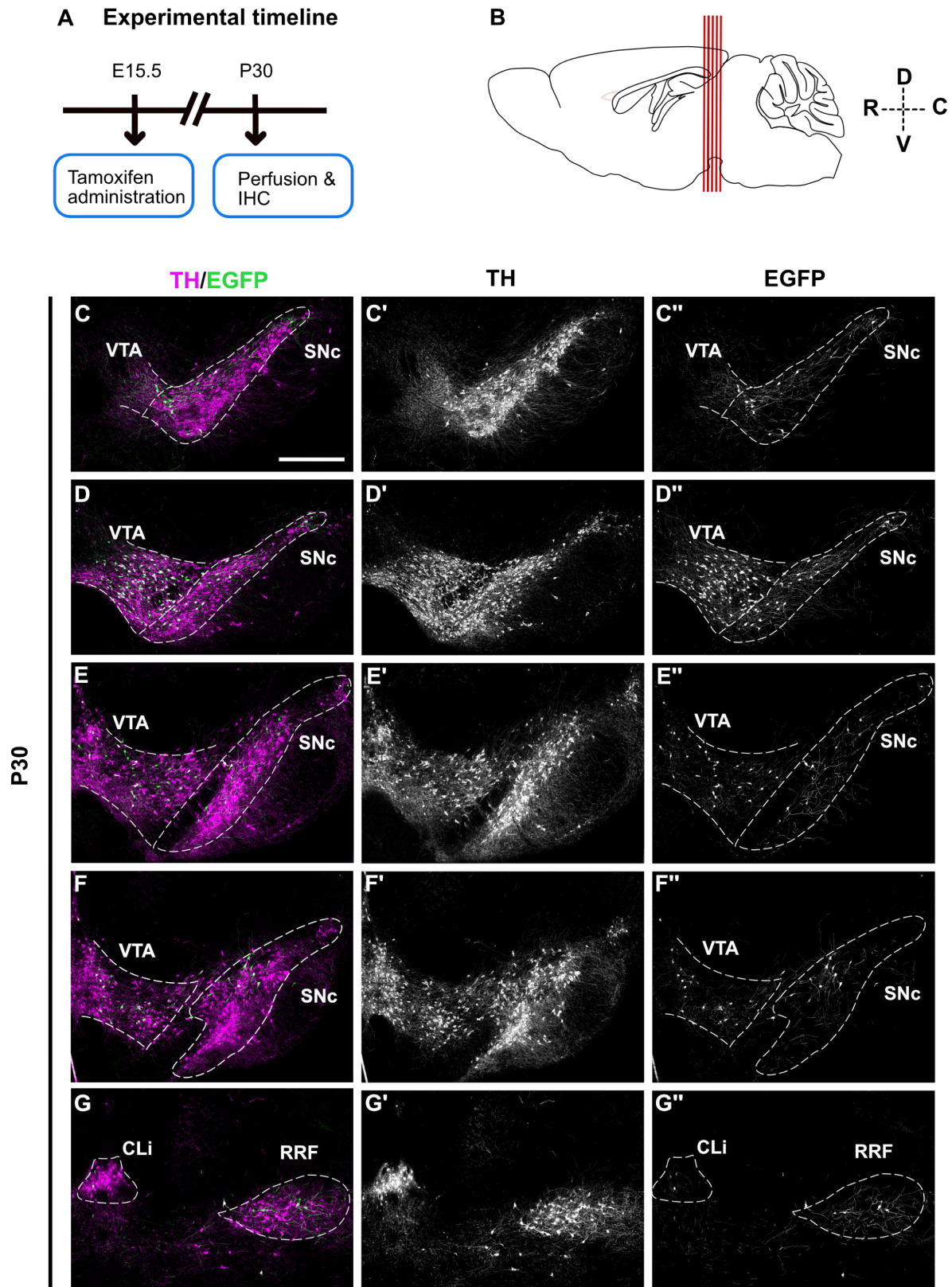TH/EGFP   TH   EGFP

P30

Figure 14. (Figure legend on next page)

Figure 14. Distribution of recombined neurons in the adult ventral midbrain after CreER induction at E15.5. (A) Schematic showing the experimental timeline. Tamoxifen was administered to pregnant mice at embryonic day E15.5. Brains were dissected and analysed at P30. (B) Schematic of a sagittal section through the adult mouse brain. Red lines indicate the rostrocaudal levels of the coronal sections shown in C-G''. **(C-G'')** Immunofluorescent staining for TH and EGFP on coronal sections of the midbrain at P30. Recombined neurons positive for EGFP were found in the VTA and SN **(C-F'')** as well as in the CLi and RRF **(G-G'')**. Mice analysed (n=7 mice). Scale bar: 500 μm **(C-G'')**.

No EGFP positive fibres were found in the NAc core, nor in the medial prefrontal cortex (mPFC) and the basolateral amygdala (BLA) **(Figure 13A-A''** and data not shown). In target areas of SN-mDA neurons, innervation originating from recombined mDA neurons was observed in the caudal dorsomedial striatum (DMS) **(Figure 13B-B'')** and in the ventral tail of the striatum **(Figure 13C-C'')**. The DMS is a known target of mDA neurons located in the medial SNc, while the TS is a target of SNl mDA neurons (Lerner et al., 2015; Menegas et al., 2018; Poulin et al., 2018). Very sparse innervation was found in the rostral DMS **(Figure 13A-A'')** and in the dorsolateral striatum **(Figure 13B-B'')**. The distribution of recombined EGFP positive neurons and their projections to the striatal area were also analysed in the adult brain at P30, after Tamoxifen administration to pregnant females at E15.5. Distribution of EGFP positive neurons in the adult brain was comparable to the distribution in E18.5 embryonic brains **(Figure 14C-G''**; compare with **Figure 12)**. Specifically, EFGP positive recombined neurons were found throughout the VTA at different rostrocaudal levels of the midbrain. Most of the recombined neurons were found in the parabrachial pigmented nucleus (PBP), while less double positive cells were found in the paranigral nucleus (PN) **(Figure 16C)**. Almost no recombination was found in the more medial interfascicular nucleus (IF) **(Figure 16B)**. In the SN, TH$^+$ EGFP$^+$ neurons were mostly located in both medial (m_SN) and lateral (l_SN) SNc **(Figure 16B)**. Recombined neurons were also found in the substantia nigra pars lateralis (SNl), but only at more posterior levels of the midbrain **(Figure 16B)**. Of note, the EGFP positive neurons distribution in the adult brain was similar to the distribution of *Bcl11a*-mRNA expressing mDA neurons or β-gal-expressing cells in *Bcl11a-lacZ* mice at P30 **(Figure 14C-G''**, compare with **Figure 3)**. Analysis of the projection pattern established by EGFP positive fibres confirmed the strong innervation in the OT **(Figure 15A-C''** and **Figure 16A)**. Moreover, the ventral and lateral shell of the NAc were as well strongly innervated by EGFP positive fibres, but not the NAc core **(Figure 15A-B''** and **Figure 16A)**. Note that the innervation of the ventral and lateral NAc was not so strong at E18.5 **(Figure 15A-B''**, compare with **Figure 13A-A''** and **Figure 16A)**. This might suggest that projections to the NAc raising from *Bcl11a*-expressing mDA neurons might develop later. In addition to the projections found in the striatal region, EGFP positive fibres were found also in the intermediate region of the lateral septum (LSI), which has been shown to be one of the target areas of VTA mDA neurons (S. Khan et al., 2017) **(Figure 17A-B'')**.

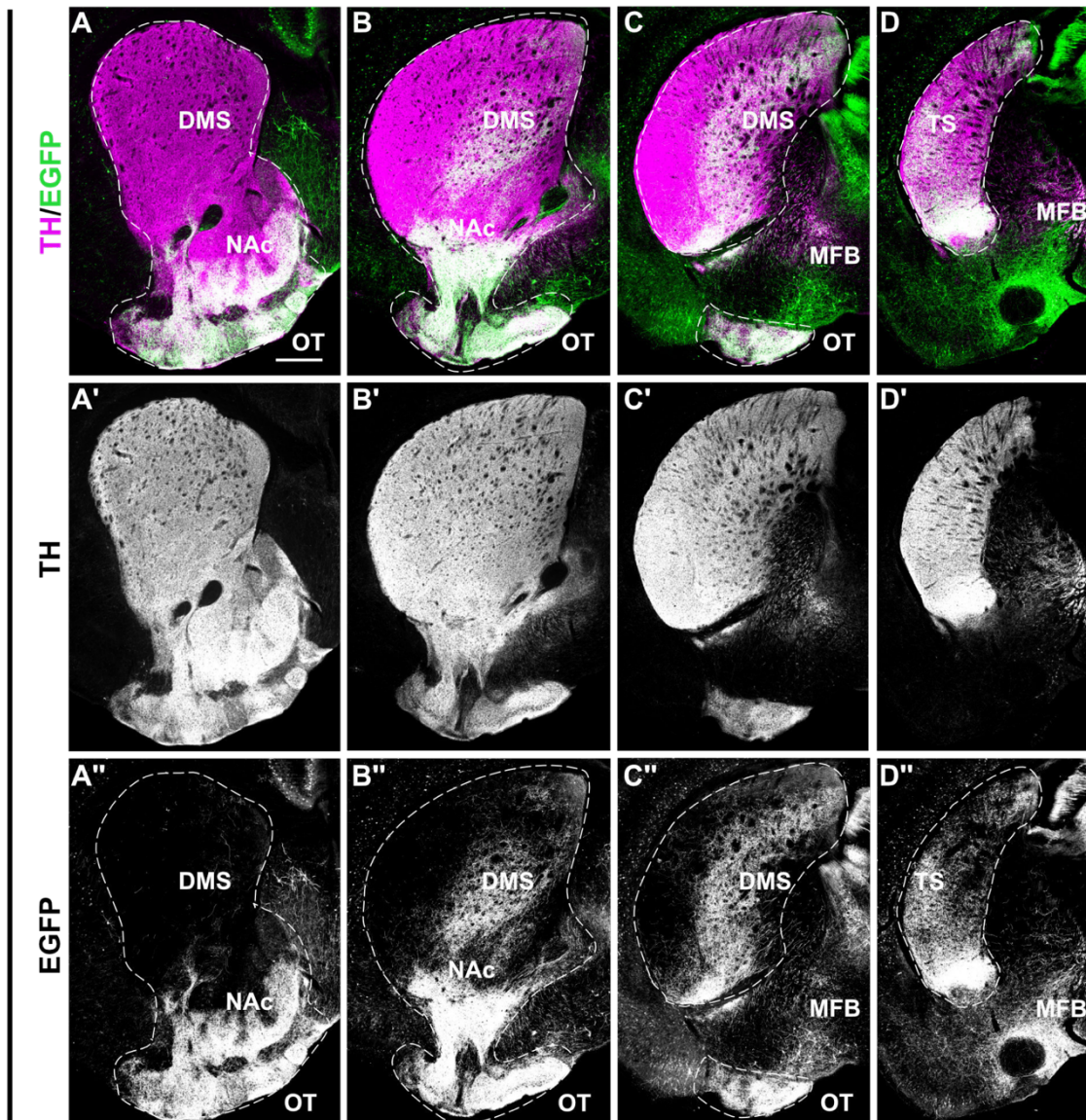**Bcl11a-mDA neurons projections to the striatal region**

Figure 15. *Bcl11a*-**expressing neurons contribute projections to subcircuits of the dopaminergic system. (A-D'')** Immunostaining for TH and GFP in rostrocaudal levels of the striatal region **(A-D')** showing that *Bcl11a*-expressing mDA neurons innervate specific subdomains of DA projection targets including the OT **(A-C'')**, the Nucleus Accumbens (NAc) shell **(A-B'')**, the DMS **(A-C'')** and the TS **(D-D'')**. Mice analysed (n=7 mice). Scale bar: 500 µm **(A-D'')**.

Interestingly, the dorsal region of the lateral septum (LSD), which is as well innervated by VTA mDA neurons, was lacking innervation coming from *Bcl11a*-expressing mDA neurons **(Figure 17A-B'')**. In addition to the above mentioned VTA-mDA neurons target areas, mPFC and BLA were analysed. These two areas were not innervated by EGFP positive neurons, confirming the data obtained in E18.5 brains (data not shown).
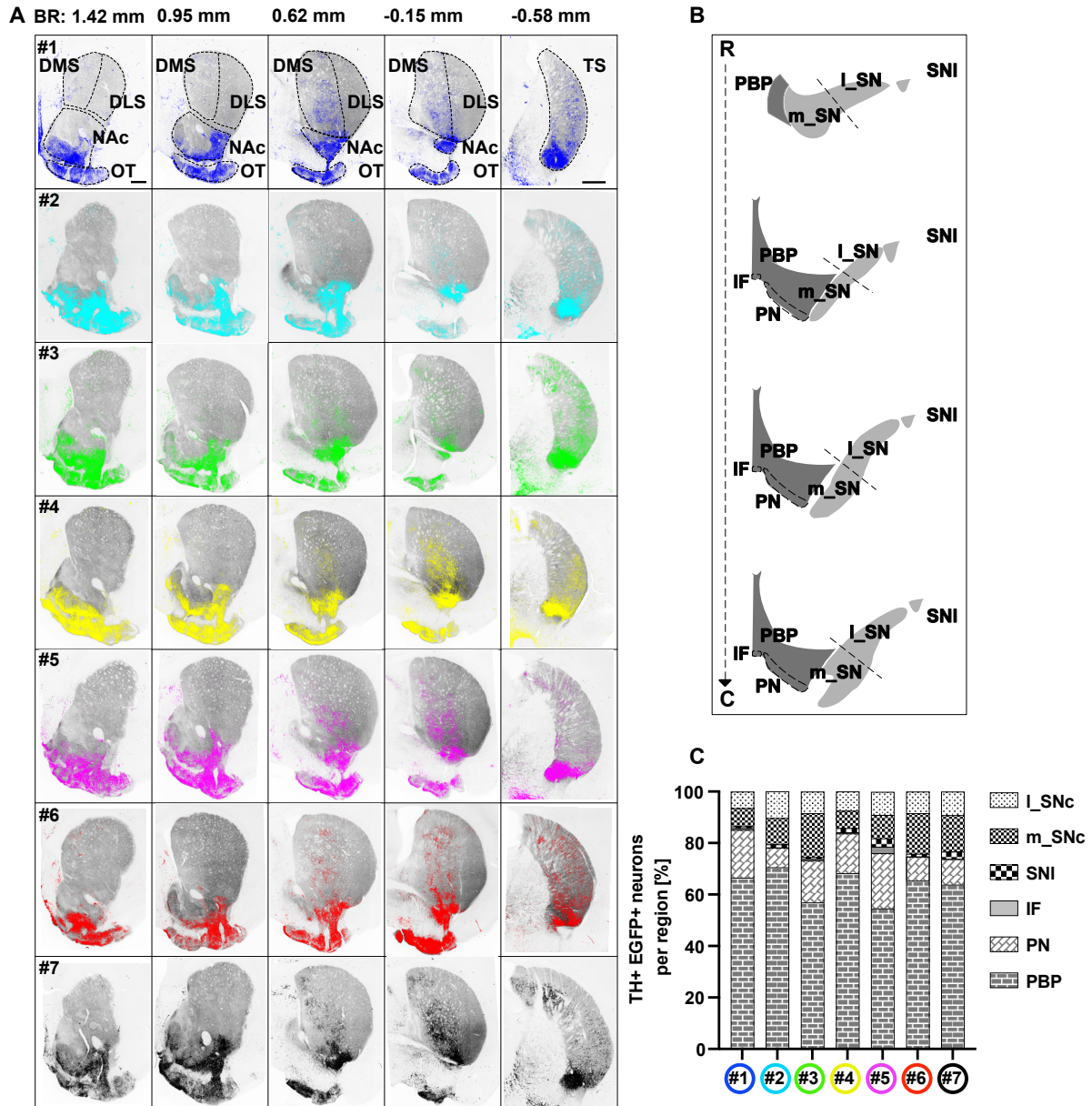
Figure 16. Distribution of *Bcl11a*-expressing mDA neurons labelled with the intersectional fate mapping approach and their projections to the striatal region shown for individual mice. (A) Projections of axons labelled with the intersectional fate mapping approach (EGFP+) in five rostro-caudal striatal coronal sections shown for individual mice. TH immunostaining is shown in grey. **(B)** Schematic showing the SN and VTA divided into subregions at four rostro-caudal midbrain levels. This subdivision was used to analyse the distribution of mDA neurons labelled with the intersectional fate mapping approach in the SN and VTA **(C)** Distribution of mDA neurons labelled with the intersectional fate mapping approach (EGFP+ and TH+) for individual mice (1-7). SN: medial SNc (m_SN), lateral SNc (l_SN), and substantia nigra pars lateralis (SNl); VTA: parabrachial pigmented nucleus (PBP), paranigral nucleus (PN) and interfascicular nucleus (IF). Scale bar: 500 µm **(A)**.

The innervation pattern established from *Bcl11a*-expressing mDA neurons of the SN was also confirmed in the adult brain (**Figure 15A-D''**, compare with **Figure 13**). The most ventral part of the TS shows the highest density of EGFP positive fibres **(Figure 15D-D'')**. A highly specific projection pattern to the caudal DMS was also confirmed **(Figure 15B-C'')**.

Very sparse innervation was observed in the dorsolateral **(Figure 15B-C'')** and rostral striatum **(Figure 16A-A'')**.

With this approach, EGFP positive fibres were found in areas of the forebrain that are not innervated by mDA neurons **(Figure 15 and Figure 17)**. These fibres were TH negative and are likely to originate from scarce recombined non mDA neurons that were found throughout the brain (e.g.: midbrain, cortex , data not shown). One reason that might explain this ectopic EGFP labelling could be leaky expression of the Ai82D allele, potentially occurring without tTa-mediated activation (Van Hove et al., 2020).
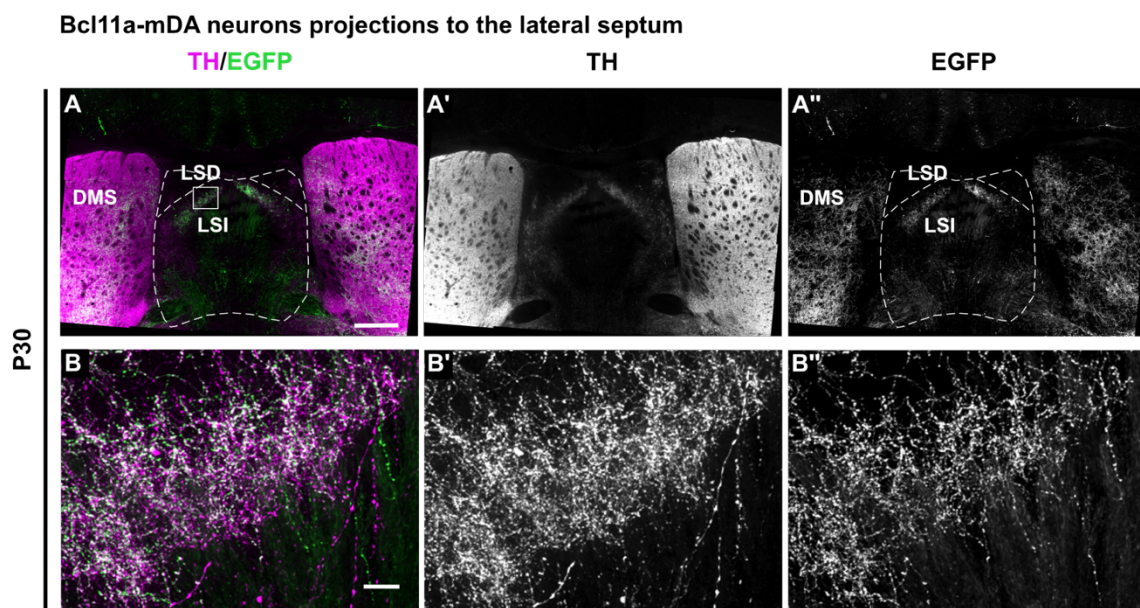

Figure 17. *Bcl11a*-expressing neurons innervate the intermediate part of the lateral septum. (A-B'') Immunostaining for TH and GFP in the lateral septum showing that *Bcl11a*-expressing mDA neurons innervate the intermediate lateral septum **(**LSI). **(B-B'')** Higher magnification of the boxed area in A. Mice analysed (n=8 mice). Scale bars: 50 μm **(B-B'')** and 500 μm **(A-A'')**

However, the leakiness of the Ai82 allele did not interfere with the *Bcl11a*-expressing mDA neurons projection analysis, because DA projections were always identified using antibody staining against TH.

Next, in order to assess whether projections of *Bcl11a*-expressing mDA neurons in the adult brain innervate the same projection target areas as in the embryonic brain, intersectional fate mapping experiments were carried out by administering Tamoxifen to adult mice. Specifically, P30 *Bcl11a*$^{CreER/+}$,Dat$^{tTA/+,}$*Ai82D*$^{TRE/+}$ mice were injected with a single dose of Tamoxifen to activate CreER. One week later, mice were perfused and their brains analysed **(Figure 18A)**. Only few EGFP positive recombined neurons were found in the VTA (Figure 13B-B''). Of note, recombined neurons were neither detected in the SN **(Figure 18B-B'** and data not shown**)**, nor were fibres observed in the striatal region. These results suggest that the CreER activation achieved with Tamoxifen injection at adult stages is not sufficient to label Bcl11a-expressing mDA neurons and their projections. Therefore, a different approach had to be used.
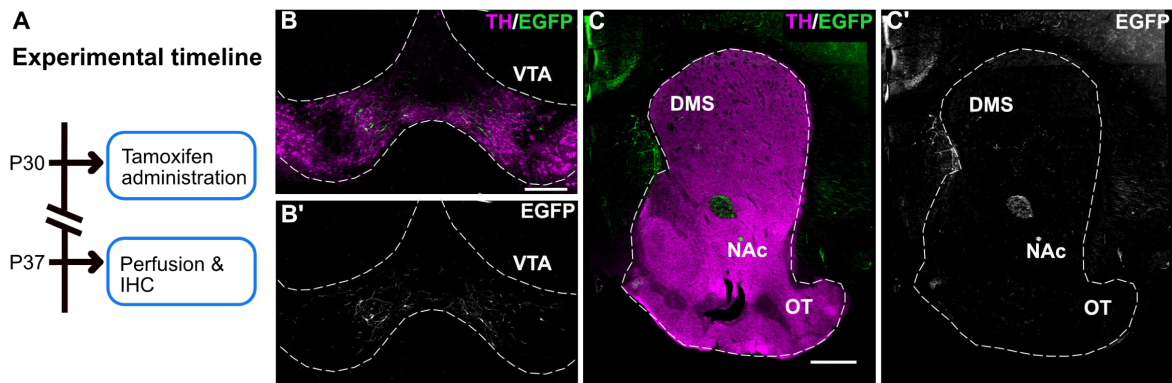
Figure 18. *CreER-DattTa* **mediated recombination of the intersectional reporter allele at adult stages is not strong enough to label *Bcl11a*-expressing mDA neurons projections. (A)** Schematic showing the experimental timeline. Tamoxifen was administered to adult mice at P30. One week after Tamoxifen administration, mice were perfused and the brain analysed. **(B-C')** Immunofluorescent staining for TH and EGFP showing only few recombined neurons positive for EGFP in the VTA. No recombined neurons were found in the SN **(B-B')** as well as no EGFP positive fibres were detected in the striatal region **(C-C')**. Scale bar: 500 µm **(C-C')** and 250 µm **(B-B')**.

4.3.3 Anterograde viral tracing approach to label *Bcl11a*-expressing mDA neurons and their projections in the adult brain

To understand/investigate if *Bcl11a* expression in the adult brain defines the same subset of mDA neurons as in the embryonic brain, an anterograde viral-based tracing approach was used. This method allows to clearly distinguish the projection targets of *Bcl11a*-expressing neurons in the SN versus those in the VTA. Reporter constructs were introduced by the injection of recombinant adeno-associated viruses (rAAV) into either the VTA or SN of adult animals, with the purpose of restricting the reporter activation only to *Bcl11a*-expressing neurons only to one of these two nuclei **(Figure 19A; Figure 20A)**. Eight days after the rAAV injection, CreER was activated through Tamoxifen administration for three consecutive days to achieve recombination. Two weeks after the last Tamoxifen administration the mice were perfused and the recombination analysed **(Figure 19B; Figure 20B)**. Co-staining for the reporter construct and TH allowed to characterize the projection pattern of *Bcl11a*-expressing mDA neurons. Two different approaches were used: a non-intersectional approach and an intersectional approach. In the non-intersectional approach, a Cre-dependent reporter construct was delivered into the midbrain of *Bcl11a^CreER^* mice **(Figure 20A)**. Labelling of *Bcl11a*-expressing mDA neurons obtained with this method was scarcer in the SN when compared to the VTA **(Figure 19C,D, Figure 19G,H)**.
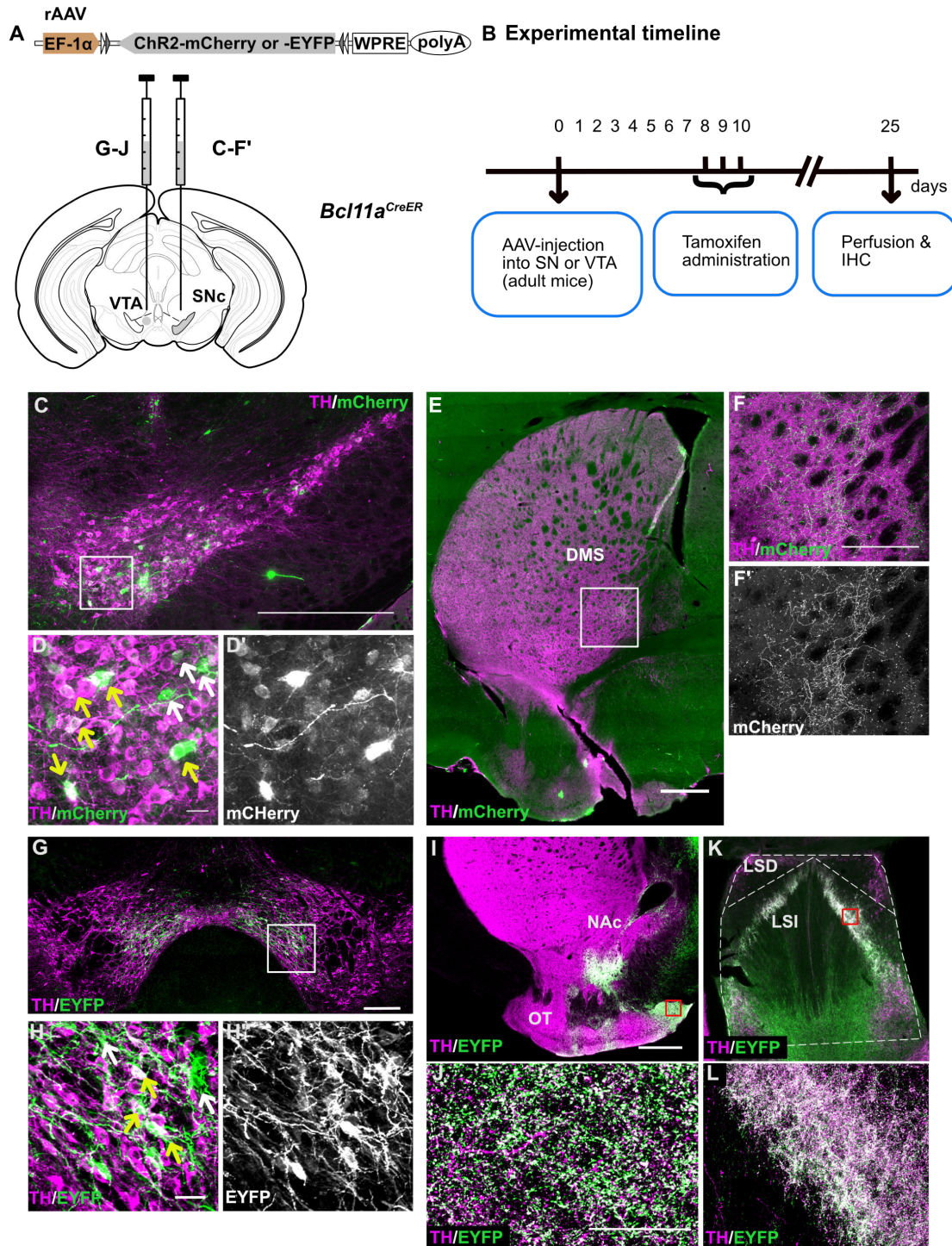
Figure 19. *Bcl11a*-**expressing neurons of the VTA and SN show a specific innervation pattern of forebrain targets. (A)** Schematic showing injection of rAAV:double floxed Channelrhodopsin2 (ChR2)-mCherry or rAAV:double floxed ChR2-EYFP into the SN or VTA of *Bcl11a*$^{CreER/+}$ mice. **(B)** Schematic showing the experimental timeline. Tamoxifen administration 8 days after the virus injection leads to sparse expression of the reporter protein (mCherry or EYFP) in *Bcl11a*-expressing neurons. **(C-F′)** Immunofluorescent staining for TH and mCherry in the SN **(C-D′)** and the striatum **(E-F′)**. **(E-F′)** A cluster of mCherry$^+$-fibers in the dorsomedial striatum (DMS). **(F-F′)** Higher magnification of the boxed area in E. **(G-J)** Immunofluorescent staining for TH and EYFP in the VTA **(G-H′)** and in the NAc and OT **(I-J)**. **(J,L)** Higher magnification of the boxed area in I,K. Yellow arrows indicate TH$^+$ reporter protein$^+$ neurons, white arrows indicate TH$^-$ reporter protein$^+$ neurons **(D,H)**. n=7 mice for VTA injections, n=1 mouse for SN injection. Scale bars: 500 µm **(C,E,I)**, 250 µm **(G)** and 25 µm **(F-F′,J)**.

These data are consistent with a lower percentage of *Bcl11a*-expressing neurons in the SN compared to the VTA **(Figure 6)**. The sparse labelling allowed to visualize patches of innervation restricted to the DMS **(Figure 19E,F)**. Characterization of the VTA projection targets revealed strong innervation of the OT in a stripe-like pattern and innervation of the ventral NAc shell, but not the NAc core **(Figure 19I).** When the lateral septal area was analysed, a strong innervation originating from *Bcl11a*-expressing VTA mDA neurons was found in the LSI, but not in the LSD **(Figure 19K-L)**. Of note, no projections to the PFC and BLA were found (data not shown). By using the non-intersectional viral based approach, recombined non-DA *Bcl11a*-expressing neurons were found in both the SN and VTA of *Bcl11a*^{CreER} mice **(Figure 19C,D, Figure 19G,H)**. These *Bcl11a*-expressing non-DA neurons might give rise to long range projections to the forebrain. Indeed, EYFP positive fibres negative for TH were found outside the striatal region containing projections from mDA neurons **(Figure 19I)** and in the area below the LSI devoid of TH positive fibres **(Figure 19K)**. These data are consistent with *Bcl11a* expression data in the adult brain, showing that half of them in both SN and VTA are not DA **(Figure 6)**. In the intersectional approach, a Cre-tTa dependent intersectional reporter construct was introduced into the midbrain of *Bcl11a*^{CreER}, *Dat*^{tTa} mice **(Figure 20A)**. Therefore, the viral construct expression was uniquely restricted to *Bcl11a*-expressing mDA neurons and their projections **(Figure 20C,D, Figure 20G,H)**. Of note, the labelling of *Bcl11a*-expressing mDA neurons was scarcer in the SN compared to the VTA, in line with the results obtained with the non-intersectional approach. Labelling of *Bcl11a*-expressing mDA neurons in the SN allowed to visualize patches of innervation in the ventral TS **(Figure 20E,F)**, while labelling of Bcl11a-expressing mDA neurons in the VTA showed strong innervation of the OT. These data confirmed the results obtained with the embryonically-induced intersectional labelling approach **(Figure 15)**. Taken together, these results show that Bcl11a-expressing mDA neurons form a subset of mDA neurons with highly specific subcircuit within the mDA system, in both in embryogenesis and adulthood.
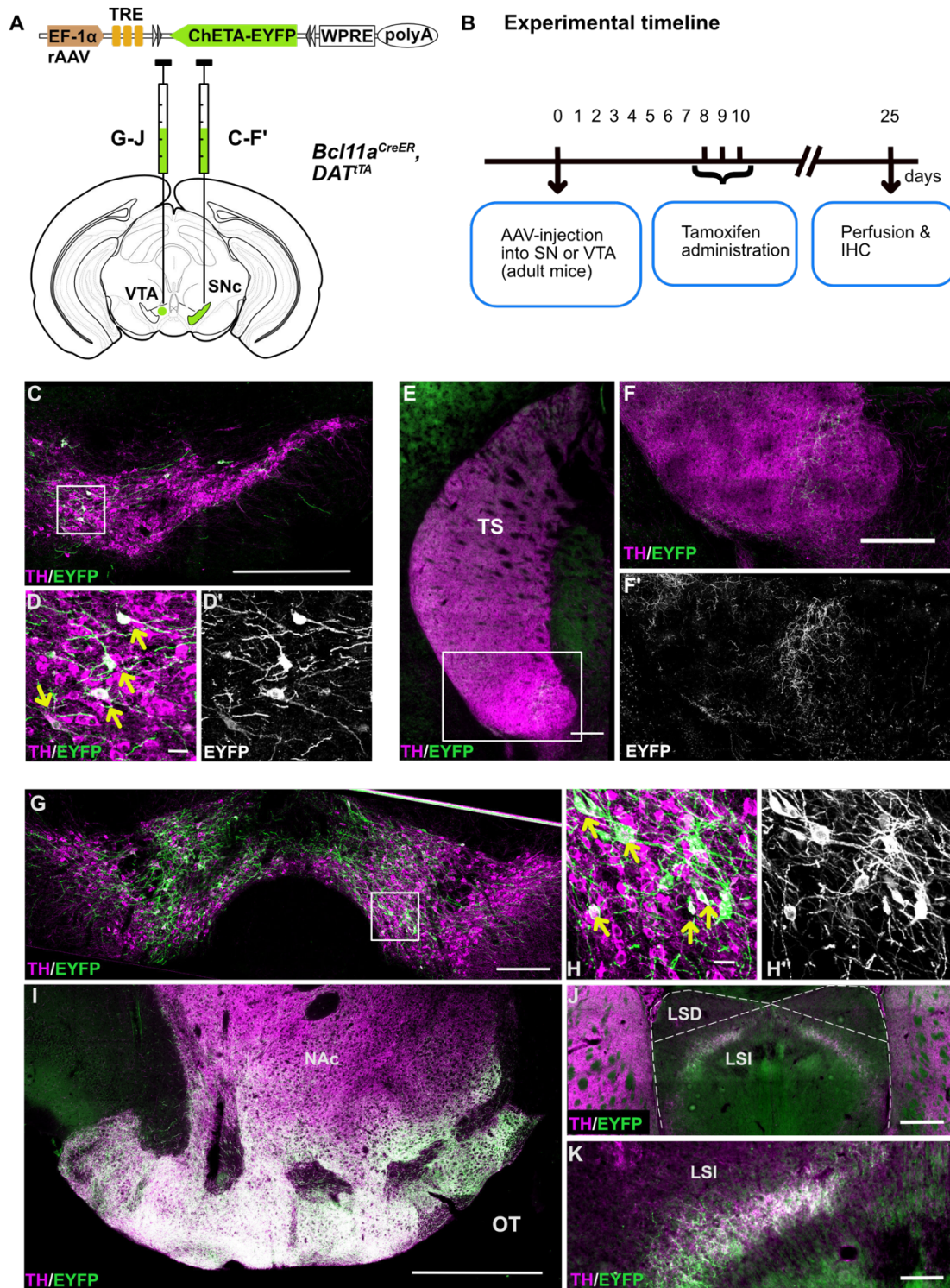
Figure 20. *Bcl11a*-expressing mDA neurons of the VTA and SN show a specific innervation pattern of forebrain targets. (A) Schematic showing injection of rAAV with an intersectional reporter construct into the SN or VTA of *Bcl11a*^{*CreER/+*}; *Dat*^{*tTA/+*} mice. **(B)** Schematic showing the experimental timeline. Tamoxifen administration 8 days after the virus injection results in expression of the reporter protein (EGFP) in *Bcl11a*-expressing mDA neurons. **(C-F')** Immunostaining for TH and EGFP in the SN **(C-D')** and the striatum **(E-F'). (E-F')** EGFP⁺ fibers in the TS. **(F,F')** Higher magnification of the boxed area in E. **(G-K)** Immunostaining for TH and the reporter protein in the VTA **(G-H'),** NAc and OT **(I-J)** and LSI **(J-K). (K)** Higher magnification of the boxed area in J. Yellow arrows indicate TH⁺ reporter protein⁺ neurons. Mice analysed (n=2 mice for SN injections, n=3 mice for VTA injections). Scale bars: 500 µm **(C,G,I,J)**, 250 µm **(E,F),** 100 µm (**K**) and 25 µm (**D,D′,H,H′**) .

73

4.3.4 Retrograde tracing approach to identify target regions of *Bcl11a*-expressing mDA neurons in the adult brain.

To assess the projections formed by *Bcl11a*-expressing mDA neurons, a retrograde tracing approach complementary to the intersectional fate mapping and anterograde viral approach was used as well. By using this neuroanatomical method, the location of cells from which a certain neuronal pathway originates can be determined after the injection of a tracer into a specific region of interest. The traced will be taken up by axons innervating the injection area and retrogradely transported to the cell bodies of those neurons that give rise to the projections being labelled.

For this purpose, the tracer choleratoxin subunit B conjugated with the fluorophore Alexa-488 (CTB-Alexa 488) was injected into different target regions of *Bcl11a*-expressing mDA neurons in adult *Bcl11a^lacZ^* mice (Conte et al., 2009). One week after the injection, mice were sacrificed and immunofluorescent staining for CTB-Alexa 488 and TH was performed on the projection target area, to examine whether CTB was expressed in the domain innervated by mDA neurons. Midbrain sections were stained for CTB, TH and β-gal and neurons that were triple positive for these markers were identified as Bcl11a-expressing mDA neurons projecting to the site of injection.

For this analysis, two main targets in the striatal region were chosen for projections originating from *Bcl11a*-expressing mDA neurons in the VTA: the ventral NAc and the OT **(Figure 21A-B, Figure 21E-F)**. After CTB-Alexa 488 injection into the NAc of Bcl11a^lacZ^ mice, retrogradely labelled cell bodies projecting to the injection site were found throughout the VTA **(Figure 21C-C')**. Of those, 19.09% +/- 5.911% were only positive for CTB, 56.24% +/- 2.672 % were double positive for CTB and TH but β-gal negative, 4.347 % +/- 2.796 % were double positive for CTB and β-gal but TH negative and 20.32 % +/- 6.035% were triple positive for these markers **(Figure 21D)**. The same analysis was performed in adult *Bcl11a^lacZ^* mice after injection of CTB-Alexa 488 into the OT. Retrogradely labelled cell bodies positive for CTB were found throughout the VTA **(Figure 21G-G')**. Of all the neurons retrogradely labelled with CTB, 18.10% +/- 9.014 were positive for CTB only, 36.67% +/- 4.854% were double positive for CTB and TH but β-gal negative, 10.79% +/- 7.396% were double positive for CTB and β-gal but TH negative and 34.44 % +/- 6.471 were triple positive for these markers **(Figure 21H)**. These data further suggest that, despite the variability in targeting the injection site of interest **(**see **Figure 21A,B** and **Figure 21E,F)** and a low number of mice analysed (n=2 for each injection site), the strongest projection of VTA *Bcl11a*-expressing mDA neurons in the striatal area may be the ones innervating the OT. Of note, almost half of the mDA neurons

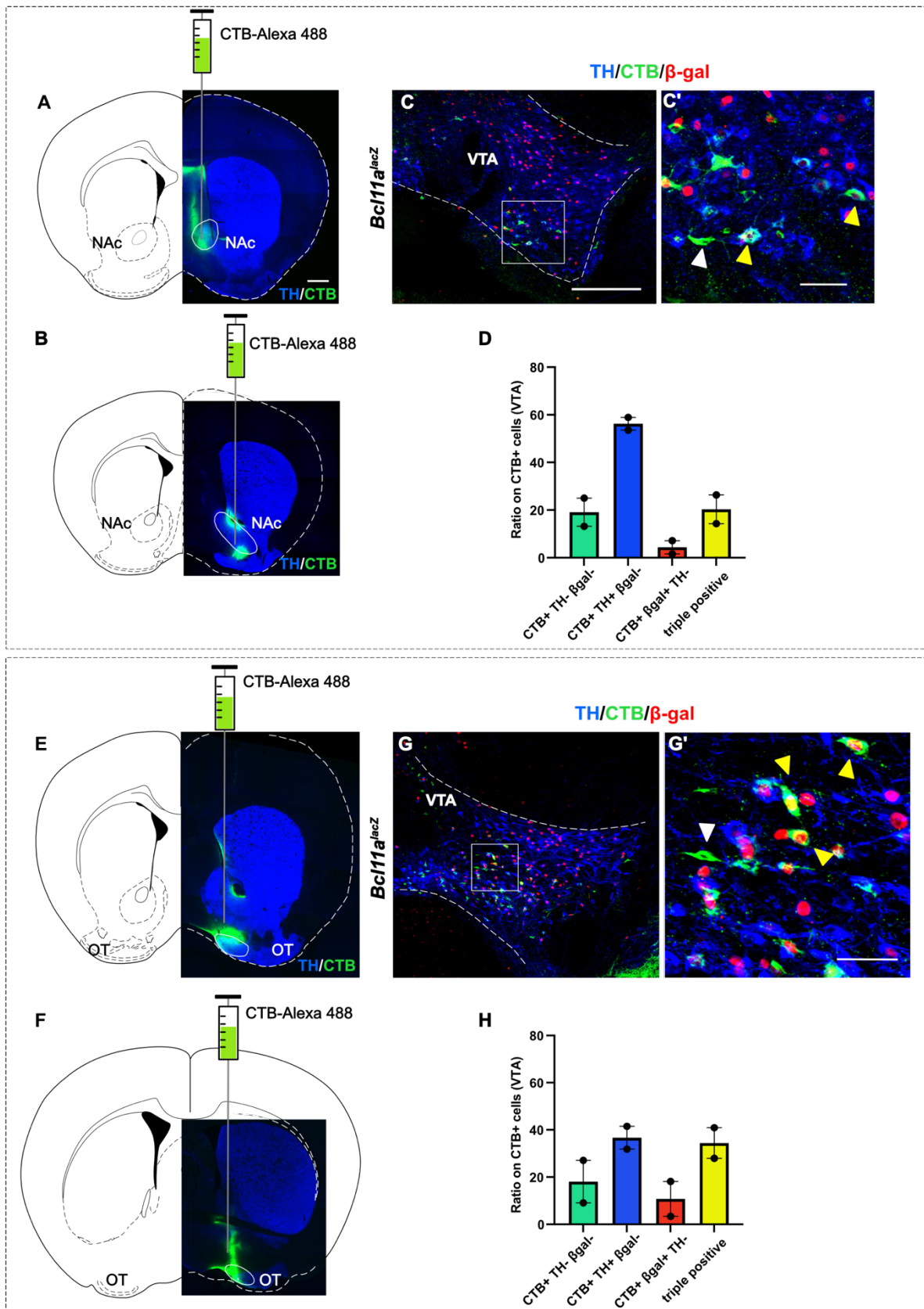retrogradely labelled after CTB injection into the OT were positive for β-gal and therefore expressed Bcl11a.

Figure 21. (Figure legend on next page)

Figure 21. Retrograde tracing of *Bcl11a*-expressing neurons mesocortical projections using cholera toxin subunit B (CTB). (A,B) Schematic showing the stereotactic injection of CTB conjugated with the fluorophore Alexa488 into the NAc of two *Bcl11a^lacz^* adult mice used for the analysis showed in D. The striatal region was immunostained for TH (blue) and CTB (green) in order to show the injection site. **(C,C')** Triple Immunostaining for TH (blue), β-gal (red) and CTB (green) in the VTA of *Bcl11a^lacZ^* mice injected with CTB into the NAc. CTB+ cells have been retrogradely labelled after CTB injection into the target area. **(D)** Percentage of CTB labelled neurons in the VTA that are only CTB+, CTB+ and TH+ but β-gal- , CTB+ and β-gal+ but TH- and CTB labelled neurons that are positive for both TH and β-gal after CTB injection into the NAc. **(E,F)** Schematic showing the stereotactic injection of CTB conjugated with the fluorophore Alexa488 into the OT of two *Bcl11a^lacz^* adult mice used for the analysis showed in H. The striatal region was immunostained for TH (blue) and CTB (green) in order to show the injection site. **(G,G')** Triple Immunostaining for TH (blue), β-gal (red) and CTB (green) in the VTA of *Bcl11a^lacZ^* mice injected with CTB into the OT. **(H)** Percentage of CTB labelled neurons in the VTA that are only CTB+, CTB+ and TH+ but β-gal- , CTB+ and β-gal+ but TH- and CTB labelled neurons that are positive for both TH and β-gal after CTB injection into the OT. **(C',G')** Higher magnification of the boxed are in C,G. White arrowheads indicate retrogradely labelled cells that are only positive for CTB, yellow arrowheads indicate retrogradely labelled cells that are positive for TH and β-gal. Mice analysed for each injection target site (n=2). Scale bars: 500 µm **(A,B,C,E,G,F)** and 25 µm **(C',G')**.

To assess projections from *Bcl11a*-expressing mDA neurons in the SN, CTB-Alexa 488 was injected in the TS of adult Bcl11a^lacZ^ mice **(Figure 22A-B)**. Retrogradely labelled neurons were found in the lateral and dorsal SNc and in the SNl **(Figure 22C)**. Of those, 14.98% +/- 10.33% were positive only for CTB, 53.23% +/- 1.422% were double positive for CTB and TH but β-gal negative, 4.672% +/- 3.467% were double positive for CTB and β-gal but TH negative and 27.12% +/- 5.436% were triple positive for all the markers **(Figure 22D)**. The majority of triple positive cells were located in the SNl. However, for one of the two mice analysed the CTB injection did not hit only the TS but, partially, also the more rostral part of the striatum (data not shown). This might explain the presence of a few triple labelled cells in the dorsolateral SNc as well (data not shown). Note that the CTB-Alexa 488 injections into the TS targeted the dorsal part of the tail, which is the part of the TS that is only sparsely innervated by *Bcl11a*-mDA neurons from the SN **(Figure 22A-B)**. Nevertheless, more than one third of the retrogradely labelled mDA neurons were positive for β-gal **(Figure 22D)**.
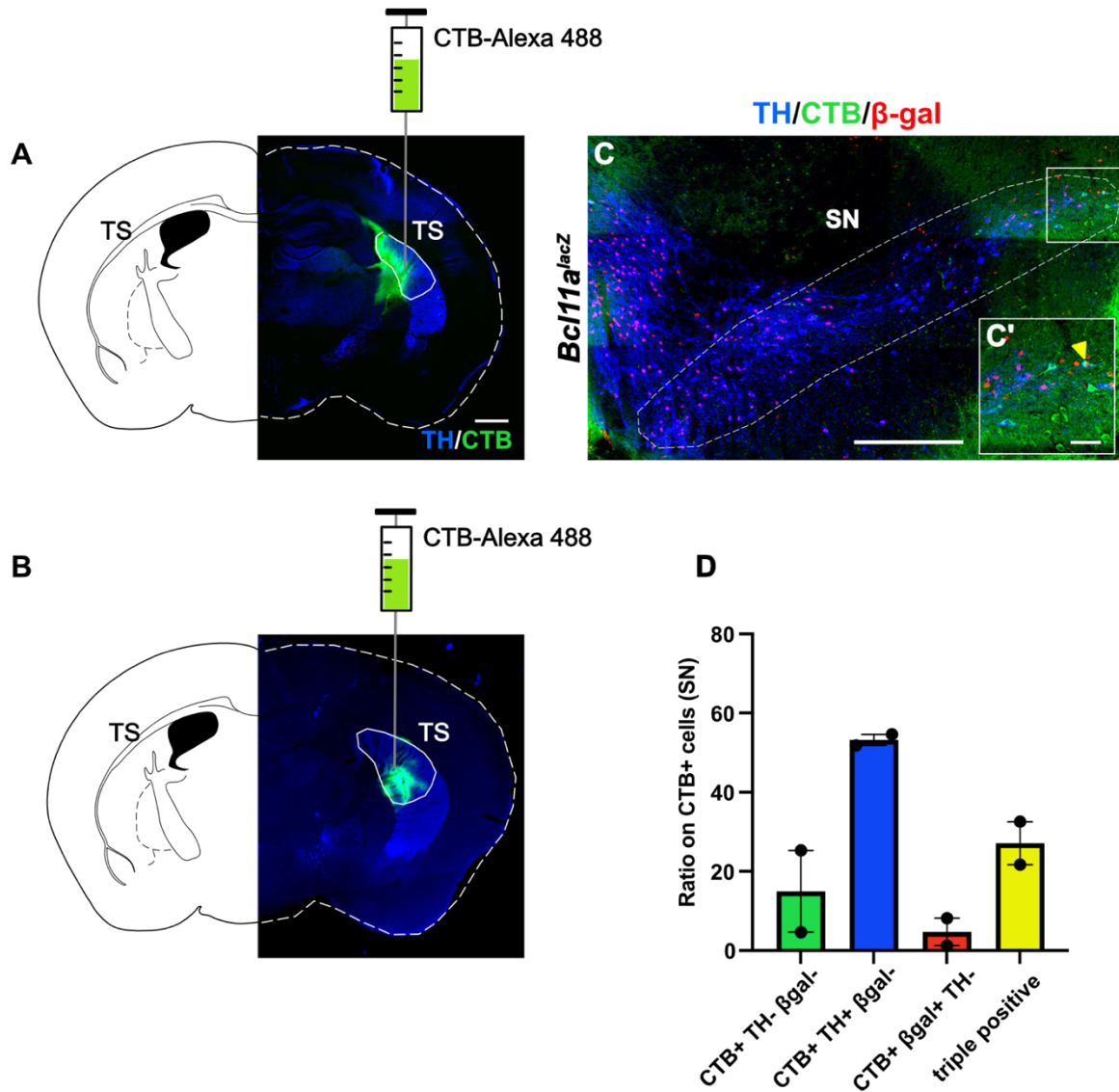
Figure 22. Retrograde tracing of *Bcl11a*-expressing neurons mesostriatal projections using cholera toxin subunit B (CTB). (A,B) Schematic showing the stereotactic injection of CTB conjugated with the fluorophore Alexa488 into the TS of two *Bcl11a^lacz^* adult mice used for the analysis showed in D . The striatal region was immunostained for TH (blue) and CTB (green) in order to show the injection site. **(C,C')** Triple Immunostaining for TH (blue), β-gal (red) and CTB (green) in the SN of *Bcl11a^lacZ^* mice injected with CTB into the TS. CTB+ cells have been retrogradely labelled after CTB injection into the target area. **(D)** Percentage of CTB labelled neurons in the SN that are only CTB+, CTB+ and TH+ but β-gal- , CTB+ and β-gal+ but TH- and CTB labelled neurons that are positive for both TH and β-gal after CTB injection into the TS. **(C')** Higher magnification of the boxed are in C. White arrowheads indicate retrogradely labelled cells that are only positive for CTB, yellow arrowhead indicates retrogradely labelled cells that are positive for TH and β-gal. Mice analysed (n=3). Scale bars: 500 μm **(A,B,C)** and 25 μm **(C')**.

4.4 Conditional gene inactivation of *Bcl11a* in mDA neurons

4.4.1 Conditional gene inactivation of *Bcl11a* in mDA neurons leads to a rostral-to-caudal shift of *Bcl11a*-mDA neurons from the VTA to the CLi and to a medial-to-lateral shift of Bcl11a-mDA neurons in the rostral SNc

BCL11a is a transcription factor that has been shown to influence neuronal fate, morphology and migration (Simon et al., 2020). BCL11A is expressed in a subset of mDA-neurons during development and its specific expression pattern is maintained into adulthood **(see Figure 6 and Figure 7)**. Thus, BCL11A might have a function in establishing and/or maintaining *Bcl11a*-expressing mDA neurons, their cell fate and their specific projection pattern. In order to assess this hypothesis, a conditional knock-out (cko) mouse line in which *Bcl11a* is specifically inactivated in mDA neurons already during development was generated. $Dat^{IRES-Cre}$ mice were crossed with $Bcl11a^{flox}$ mice ($Bcl11a$ cko^{flox}, genotype: $Dat^{IRES-Cre/+}$, $Bcl11a^{flox/flox}$) resulting in complete inactivation of *Bcl11a* in mDA neurons **(Figure 23A)**. Since BCL11A is expressed only in a subpopulation of mDA neurons, the $Bcl11a^{lacZ}$ allele was introduced in a subset of *Bcl11a* cko mice ($Bcl11a$ cko^{lacZ}, genotype: $Dat^{IRES-Cre/+}$, $Bcl11a^{flox/lacZ}$) to identify cells with a *Bcl11a* identity even after the genetic inactivation **(Figure 23A)**. Of note, the lacZ knock-in generates a *Bcl11a* null allele. In $Bcl11a$ cko^{lacZ} mice, neurons that would normally express BCL11A (termed: *Bcl11a*-mDA neurons) can still be marked with β-gal after BCL11A expression is abolished, thus facilitating the analysis of the phenotype if this subset of mDA neurons **(Figure 23B)**.
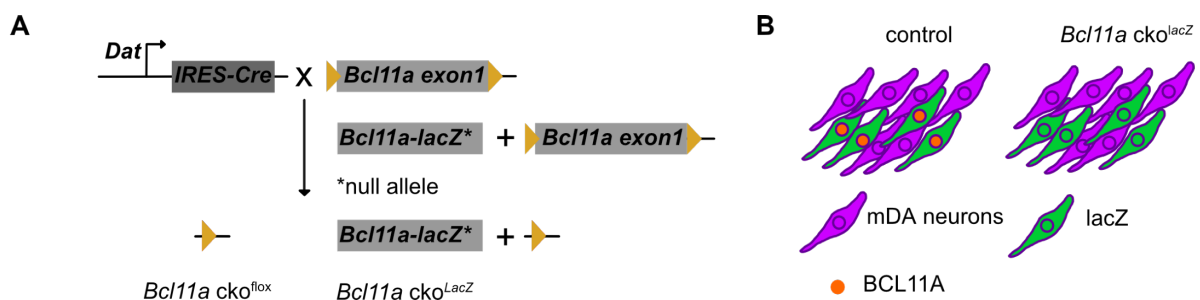

Figure 23. Inactivation of *Bcl11a* specifically in mDA neurons. (A) Schematic showing the conditional inactivation if *Bcl11a* in mDA neurons. *Bcl11a* cko mice were generated by crossing $DAT^{IRES-Cre}$ mice with either $Bcl11a^{flox/flox}$ mice (genotype: $DAT^{IRES-Cre/+}$, $Bcl11a^{flox/flox}$, termed $Bcl11a$ cko^{flox}) or $Bcl11a^{flox/lacZ}$ mice (genotype: $DAT^{IRES-Cre/+}$, $Bcl11a^{flox/lacZ}$, termed $Bcl11a$ cko^{lacZ}). **(B)** Schematic showing tha in $Bcl11a$ cko^{lacZ} mice β-gal is a marker for *Bcl11a*-mDA neurons, even after BCL11A expression is abolished.

To assess if BCL11A protein was no longer detectable in mDA neurons after *Bcl11a* inactivation, immunostaining for BCL11A was performed on midbrain sections of adult *Bcl11a*

cko[flox] mice. BCL11A expression is absent in mDA neurons of *Bcl11a* cko[flox] mice. Neurons positive for BCL11A but negative for TH were still found in the ventral midbrain of *Bcl11a* cko[flox] mice, confirming the expression of *Bcl11a* in non-DA neurons and the specific inactivation of *Bcl11a* in mDA neurons only **(Figure 24A-F)**. As expected, BCL11A expression in the cerebral cortex of *Bcl11a* cko[flox] mice was comparable to the control **(Figure 24G-H)**.
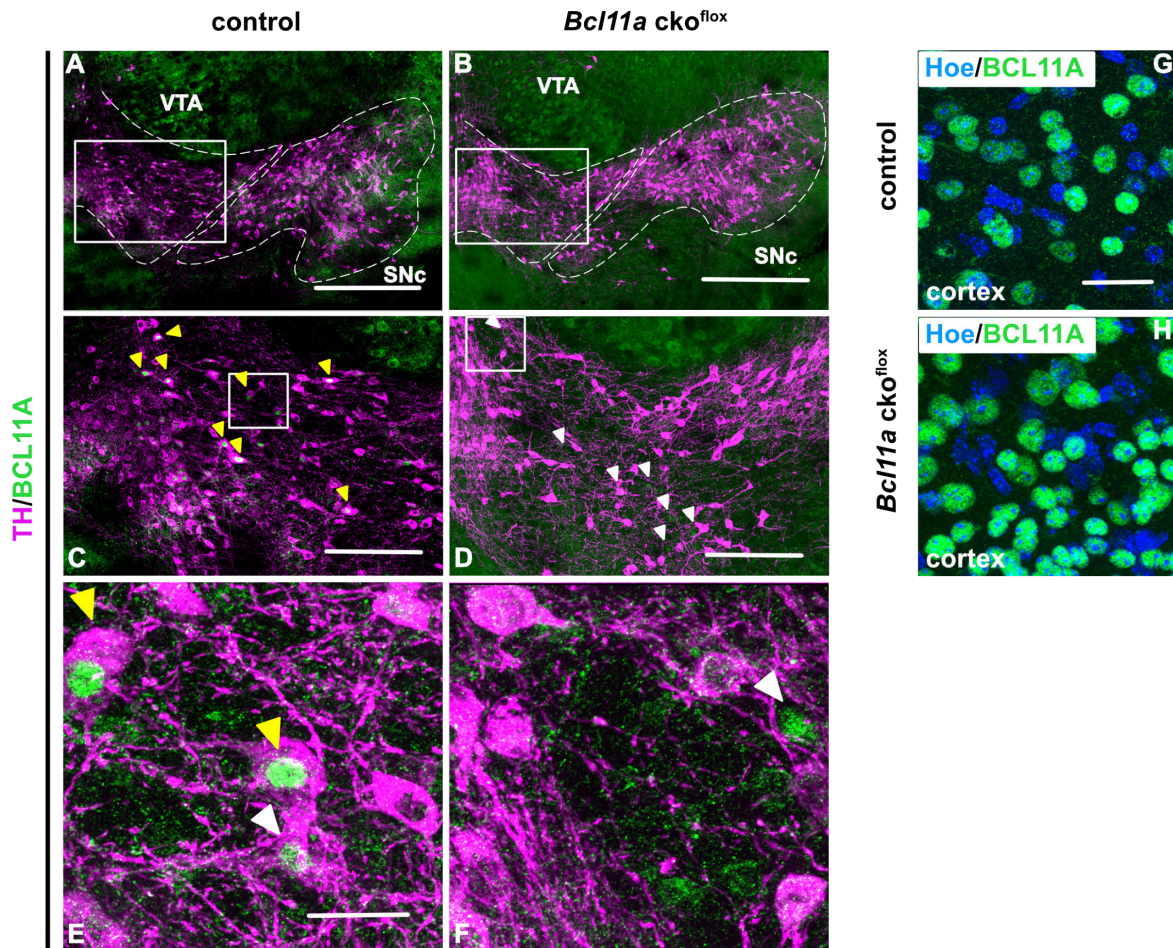

Figure 24. BCL11A expression is absent in mDA neurons of *Bcl11a* cko mice. (A-F) Immunofluorescent staining for BCL11A and TH on control **(A,C,E)** and *Bcl11a* cko[flox] **(B,D,F)** coronal sections of adult brain. BCL11A expression is present in mDA neurons of control mice **(A,C,E,** yellow arrowheads**)**, but is absent in mDA neurons of Bcl11a cko[flox] mice **(B,D,F)**. BCL11A is still expressed in non-DA neurons of Bcl11a cko[flox] mice midbrain **(B,D,F,** white arrowheads**)**. **(C-D)** Higher magnification of the boxed area in A-B. **(E-F)** Higher magnification of the boxed area in E-F. Yellow arrowheads indicate cells that are double positive for BCL11A and TH, white arrowheads indicate cells that are positive for BCL11A only. **(G-H)** Immunofluorescent staining for Hoechst and BCL11A in control **(G)** and *Bcl11a* cko[flox] **(H)** cerebral cortex. As expected, BCL11A is still expressed in cerebral cortex neurons of and *Bcl11a* cko[flox] mice **(H)**. Scale bars: 500 µm **(A-B)**, 250 µm **(C-D)** and 25 µm **(E-H)**.

The inactivation of *Bcl11a* in mDA neurons was also confirmed with multiplex fluorescent *in situ* hybridization experiments aimed to detect *Bcl11a* mRNA (experiments performed by Khondker Ushna Sameen Islam). In fact, *Bcl11a* mRNA was no longer expressed in mDA neurons of *Bcl11a* cko[flox] mice **(Figure 25A-D)**. Non-DA neurons expressing *Bcl11a* mRNA were found throughout the midbrain of *Bcl11a* cko[flox] mice, again confirming that in this model

Bcl11a was specifically inactivated in mDA neurons only **(Figure 25A-D)**. As expected, *Bcl11a* mRNA is still detectable in the cerebral cortex of *Bcl11a* cko^flox^ mice **(Figure 25E-E')**.
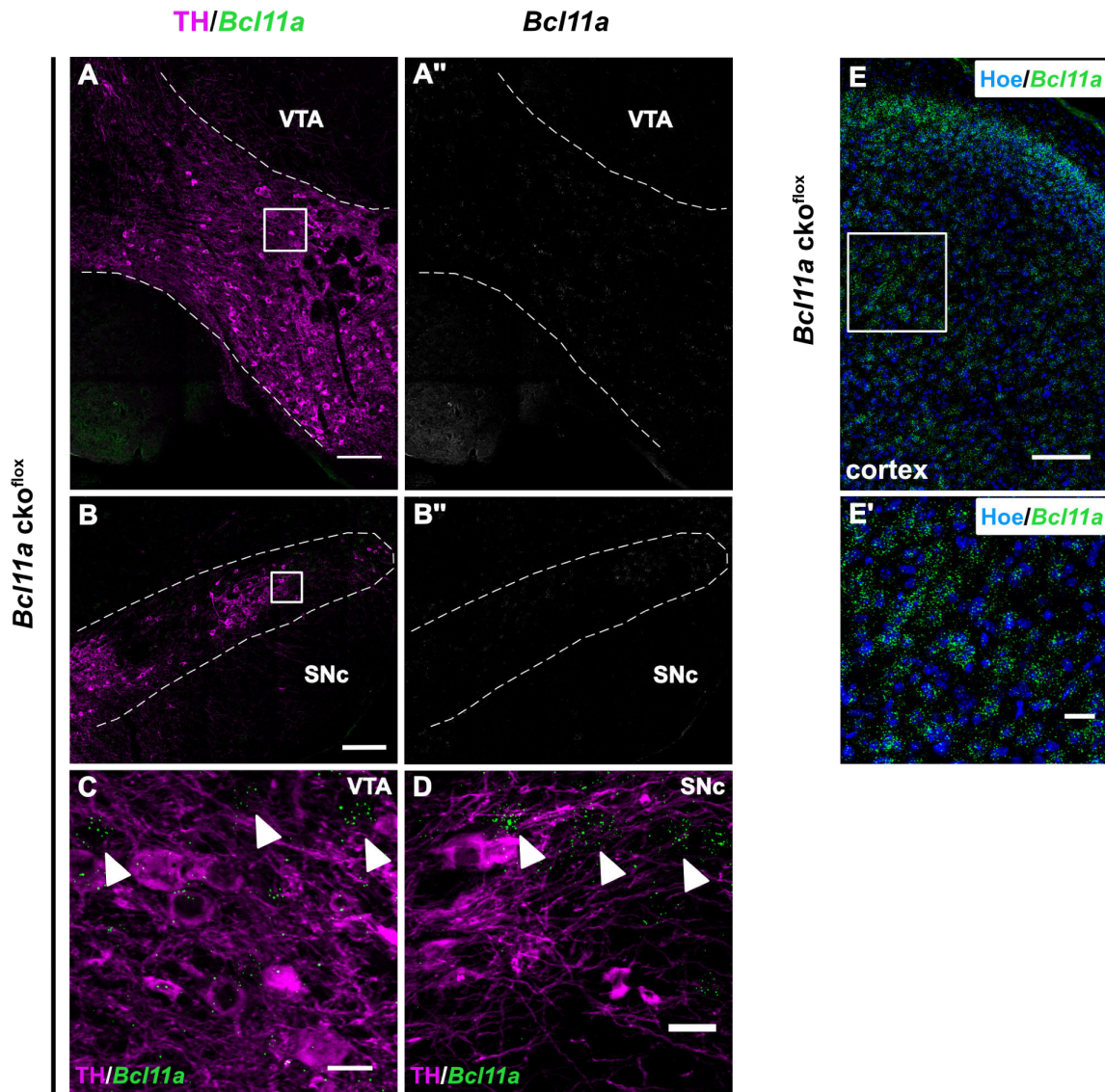

Figure 25. ***Bcl11a*** **mRNA is no longer expressed in mDA neurons of** ***Bcl11a*** **cko mice. (A-D)** Immunofluorescent staining for TH and multiplex fluorescent *in situ* hybridization for *Bcl11a* on *Bcl11a* cko^flox^ coronal sections of the adult brain. *Bcl11a* mRNA is still expressed in non-DA neurons of the *Bcl11a* cko^flox^ mice VTA **(C)** and SN **(D)**. **(C-D)** Higher magnification of the boxed area in A,B. White arrowheads indicate cells that are expressing *Bcl11a* mRNA but that are TH negative. **(E-E')** Immunofluorescent staining for Hoechst and RNAscope for *Bcl11a* in *Bcl11a* cko^flox^ cerebral cortex. As expected, cerebral cortex neurons of *Bcl11a* cko^flox^ mice are still expressing *Bcl11a* mRNA. **(E')** Higher magnification of the boxed area in E. Experiments performed by Khondker Ushna Sameen Islam. Scale bars: 250 μm **(A-B'')**, 200 μm **(E)** and 25 μm **(C,D,E')**.

Quantification of the percentage of TH neurons positive for β-gal showed a significant increase in the CLi of *Bcl11a* cko^lacZ^ mice compared to *Bcl11a-lacZ* controls **(Figure 26B)**.
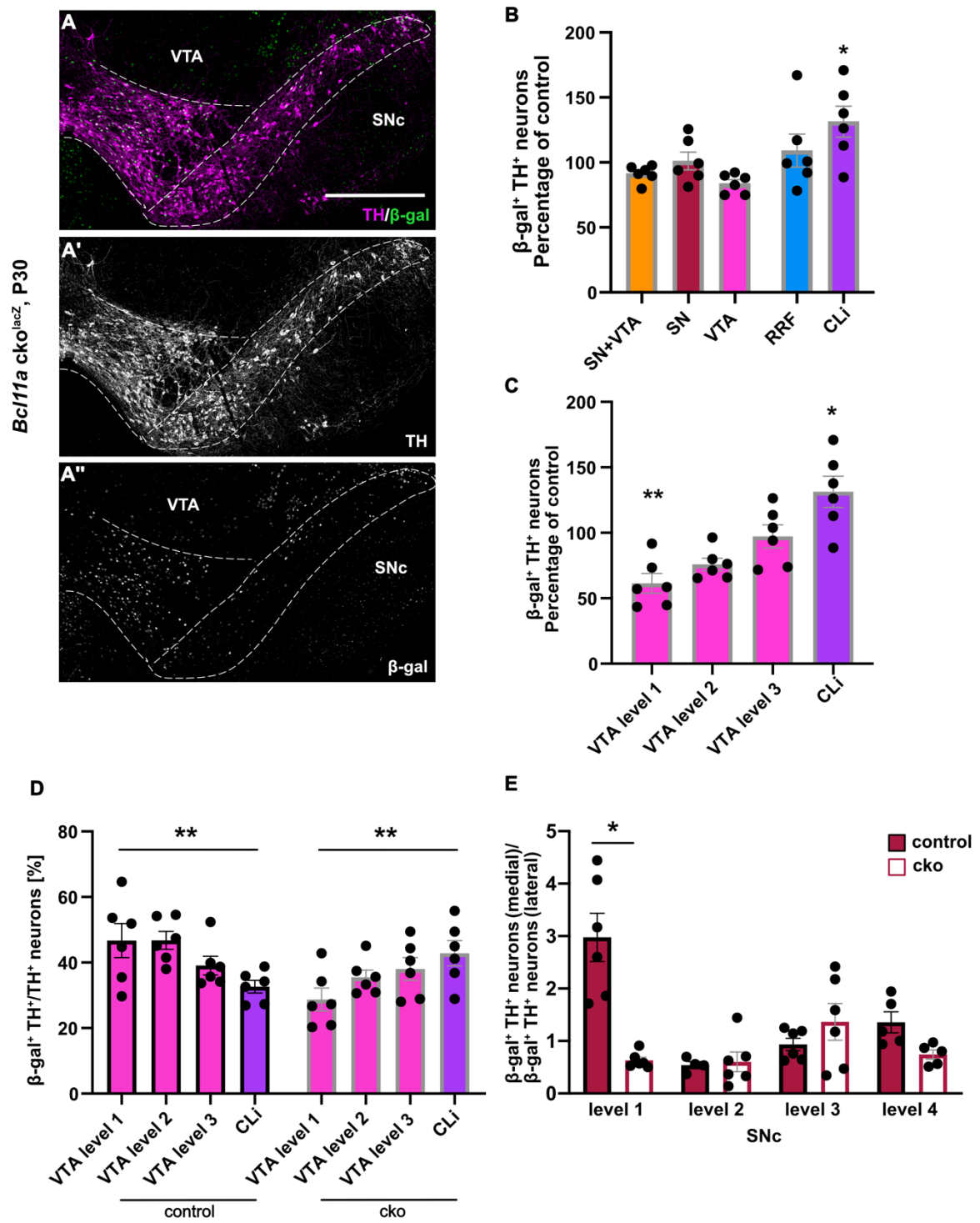
Figure 26. (Figure legend on next page)

Figure 26. BCL11A is necessary for establishing the correct rostro-caudal position of Bcl11a-expressing mDA neurons in the VTA and CLi and medial-lateral position in the SNc. (A-A'') Immunofluorescent staining for β-gal and TH on *Bcl11a* cko^{lacZ} coronal sections. **(B)** Quantification of TH⁺ β-gal⁺ neurons, expressed as percentage of control (*Bcl11a-lacZ mice*, control values are on Figure 3G). *Bcl11a*-mDA neurons are significantly increased in the CLi of *Bcl11a* cko^{lacZ} mice (n=6) indicating a shift in the distribution of Bcl11a-mDA neurons in absence of BCL11A. Statistical significance was determined by ANOVA followed by Šídák's multiple comparison test. *p < 0.05. **(C)** Percentage of β-gal⁺ TH neurons normalized to control in three rostrocaudal VTA levels and the CLi of *Bcl11a* cko^{lacZ} mice. The percentage of β-gal⁺ TH neurons at the most rostral VTA level (level 1) was significantly decreased in *Bcl11a* cko^{lacZ} compared to control mice, while there was a significant increase in the CLi. Statistical significance was determined by ANOVA followed by Šídák's multiple comparison test. *p < 0.05; **p < 0.01. **(D)** In *Bcl11a-lacZ* control animals, there is a systematic decrease in β-gal⁺ TH neurons from rostral-to-caudal (level1 to CLi), while there is a systematic increase in the percentage of β-gal⁺ TH neurons from rostral-to-caudal in *Bcl11a* cko^{lacZ} mice Statistical significance was determined by one-way ANOVA followed by a test for linear trend. **(E)** Relative contribution of β-gal positive TH neurons to the medial and lateral SNc at four different rostro-caudal midbrain levels at P30. In *Bcl11a* cko^{lacZ} mice there is a significant medial-to-lateral shift in the position of *Bcl11a*-mDA neurons in the most rostral level of the SNc. Statistical significance was determined by Welch's ANOVA followed by Dunnett's T3 multiple comparison test. *p < 0.05. Error bars indicate mean +/- SEM. Scale bar: 500 μm **(A-A')**.

When the percentage of β-gal positive TH neurons was examined in three different rostrocaudal VTA levels separately and in the CLi of *Bcl11a* cko^{lacZ} and control animals, a significant increase was again found in the CLi in addition to a reduction in the percentage of Bcl11a-mDA neurons in the most rostral VTA level (level 1) in *Bcl11a* cko^{lacZ} mice compared to controls **(Figure 26C)**.
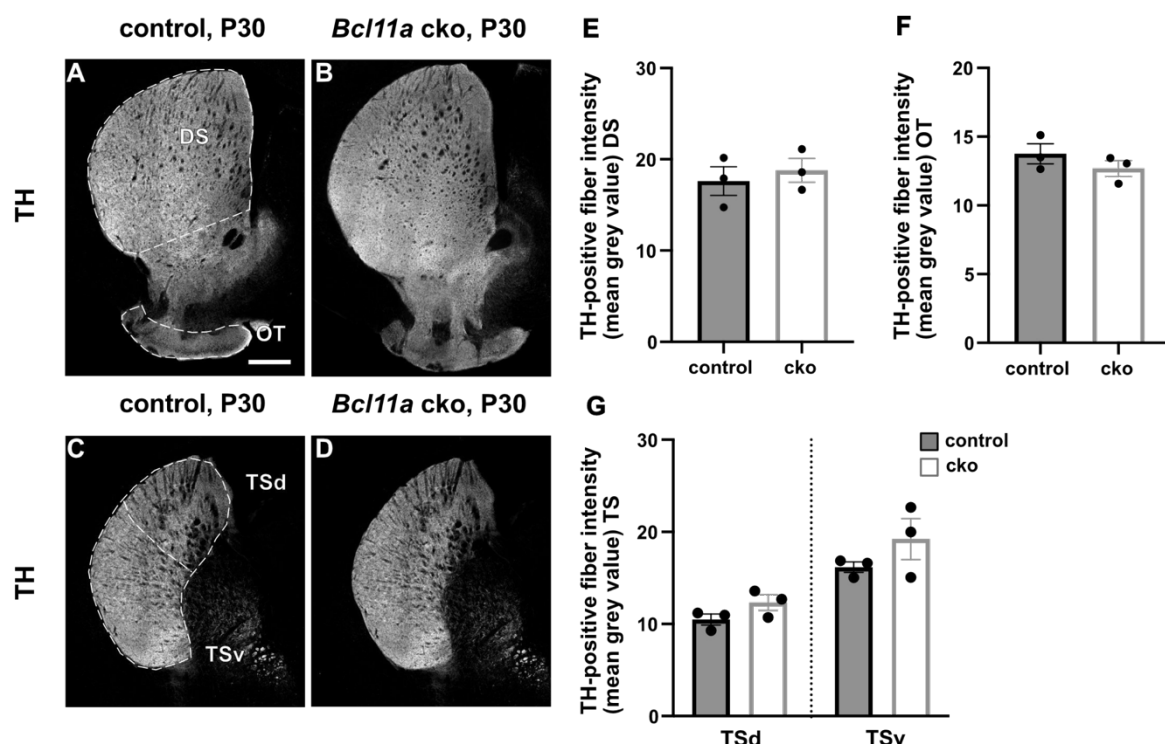
Figure 27. *Bcl11a* inactivation does not obviously affect the targeting of projections to areas innervated by *Bcl11a*-expressing mDA neurons. (D-G) Immunofluorescent staining for TH on striatal sections of control **(A,C)** and *Bcl11a* cko^{lacZ} **(B,D)** mice. **(E-G)** Quantification of TH-positive fibre density in dorsal striatum (DS) **(E)**, olfactory tubercle (OT) **(F)** and ventral (v) and dorsal (d) TS **(G)** of control (n=3 mice) and *Bcl11a* cko mice (n=3 mice) shows no difference in the density of TH innervation between the two groups. Statistical significance was determined by unpaired t-test. Error bars indicate mean +/- SEM. Scale bar: 500 μm **(A-D)**.

This resulted in a significant and systematic increase in the percentage of β-gal positive TH neurons from rostral-to-caudal in *Bcl11a* cko^lacZ mice, while there was a systematic decrease in the percentage of β-gal positive TH neurons from rostral-to-caudal in control animals **(Figure 26D)**. When combining the numbers of β-gal positive TH neurons for the CLi level and the three VTA levels, no significant difference in the percentage of β-gal positive TH neurons could be detected between *Bcl11a* cko^lacZ and *Bcl11-lacZ* animals (data not shown). Taken together, these data indicate that the reduction of β-gal positive TH neurons found in the VTA is likely due to a rostral-to-caudal shift in the position of Bcl11a-mDA neurons rather than a loss of neurons itself.

Of note, the comparison of rostral SNc and SNl levels did not show any significant difference in the percentage of β-gal positive TH neurons between *Bcl11a* cko^lacZ mice and controls (data not shown), suggesting that the rostro-caudal shift of Bcl11a-mDA neurons in *Bcl11a* cko^lacZ mice is specifically restricted to the VTA. However, in the rostral SNc, Bcl11a-mDA neurons were shifted from medial to lateral in *Bcl11a* cko^lacZ animals as compared to controls **(Figure 26E)**. These results suggest that the inactivation of *Bcl11a* in mDA neurons results in altered positioning of *Bcl11a*-mDA neurons in the VTA and SNc, without interfering with the generation or the survival of this neuronal population.

Next, in order to investigate whether the loss of *Bcl11a* affects the targeting of *Bcl11a*-mDA neurons projections, the density of TH innervation was examined in areas with the highest innervation density from *Bcl11a*-mDA neurons, the OT and the ventral TS, in both controls and *Bcl11a* cko^lacZ mice. Additionally, the density of TH innervation was analysed also in areas with a sparse innervation density form *Bcl11a*-mDA neurons, the DS and the dorsal TS. No significant difference was detected between *Bcl11a* cko^lacZ and control mice in the density of the TH innervation in any of the above-mentioned areas **(Figure 27A-G)**.

Taken together, these data suggest that despite the loss of Bcl11a results in a rostro-caudal shift in *Bcl11a*-mDA neurons it does not affect the anatomical arrangement of Bcl11a-mDA projections.

4.4.2 Conditional gene inactivation of *Bcl11a* in mDA neurons does not alter the subset markers expression of *Bcl11a*-mDA neurons

Since BCL11A is important for determining the localization of mDA neurons, it could also influence cell fate by regulating the expression of subset markers in *Bcl11a*-mDA neurons. In order to test this hypothesis, β-gal expression was analysed in combination with CALB1 and ALDH1A1 in *Bcl11a* cko^lacZ mice. Triple labelling for β-gal, TH and CALB1 **(Figure 28A-B)** and quantification of triple labelled cells did not reveal any significant difference in the number of

SN and VTA *Bcl11a*-mDA neurons co-expressing CALB1 in Bcl11a cko[lacZ] animals compared to controls **(Figure 28E)**. No difference was also found in the co-expression of ALDH1A1 in VTA and SN *Bcl11a*-mDA neurons of Bcl11a cko[lacZ] animals compared to controls **(Figure 28F).** These data suggest that the inactivation of *Bcl11a* and the resulting rostro-caudal shift in *Bcl11a*-mDA VTA neurons has no effect on the expression of known subset markers, such as CALB1 and ALDH1A1.
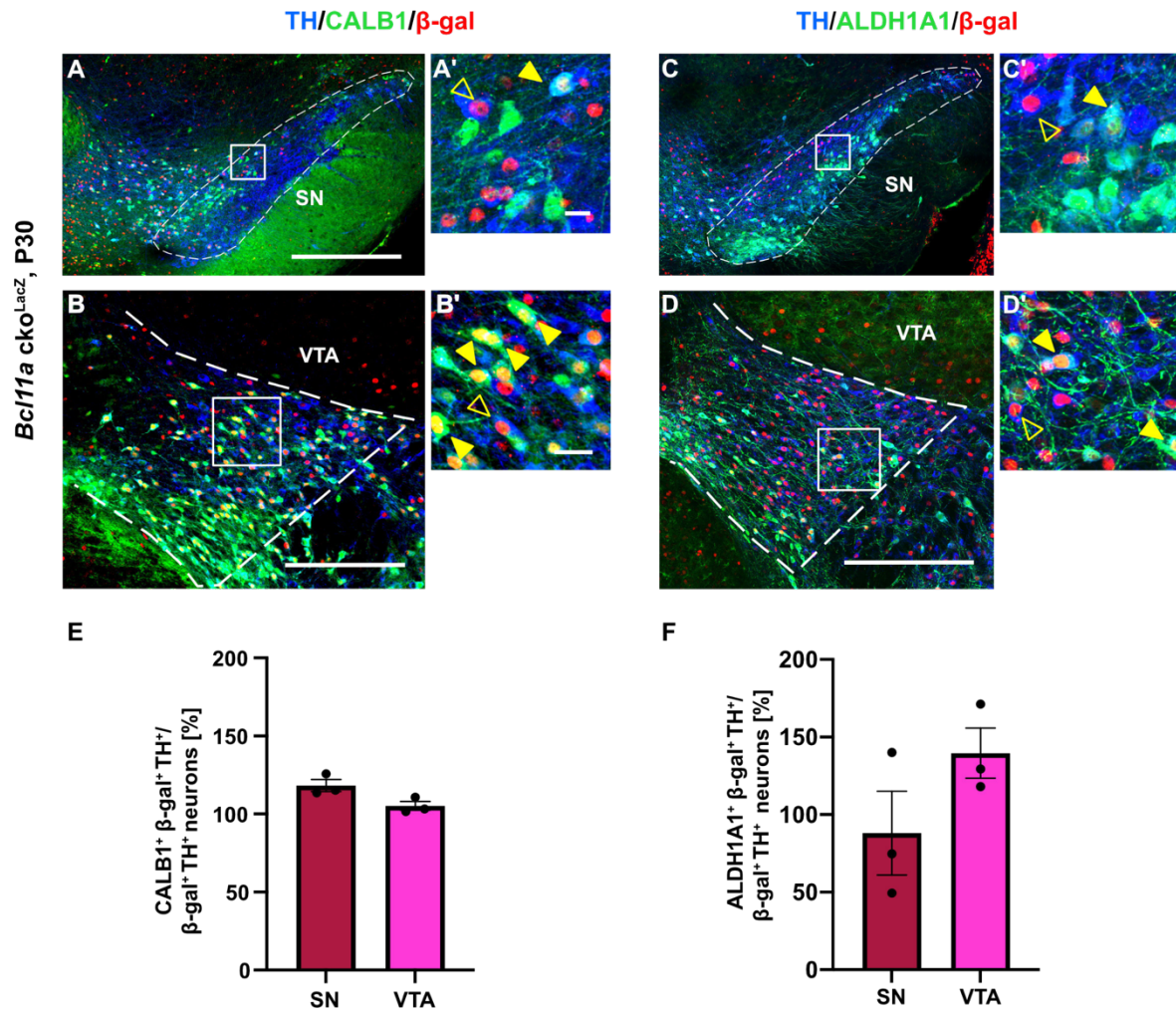

Figure 28. Expression of mDA subset markers in *Bcl11a*-expressing mDA neurons is not altered in absence of BCL11A. (A,B) Triple immunostaining for TH (blue), β-gal (red) and CALB1 (green) in the SN **(A-A')** and VTA **(B-B')** of P30 *Bcl11a* cko[lacZ] mice. **(A',B')** Higher magnification of the boxed area in A,B. **(C,D)** Triple immunostaining for TH (blue), β-gal (red) and ALDH1A1 (green) in the SN **(C-C')** and VTA **(D-D')** of *Bcl11a* cko[lacZ] mice. **(C',D')** Higher magnification of the boxed area in C,D. Filled arrowheads indicate TH[+] β-gal^{+} cells expressing the respective subset markers, unfilled arrowheads indicate TH[+] β-gal^{+} cells negative for the respective subset marker. **(E-F)** Percentage of TH[+] β-gal^{+} neurons that are positive for the respective subset marker in *Bcl11a* cko[lacZ] mice, expressed as percentage of control. Quantifications performed by Ece Ötzürk. Mice analysed (n=3 mice). Scale bars: 500 μm **(A,B,C,D),** 25 μm **(A',B',C',D').**

4.5 *Bcl11a* cko mice show behavioural impairments

The loss of *Bcl11a* results in a rostral-to-caudal and medial-to-lateral shift in the anatomical position of Bcl11a-mDA neurons. Inactivation of *Bcl11a* might lead to functional impairment in

the mDA system, either as a consequence if the subtle anatomical changes within the VTA and SN or by a direct impact on mDA function. To test this hypothesis, a range of behaviours was examined in *Bcl11a* cko and control mice using tests to assess potential mDA neuronal functions associated with VTA and/or SN. In the open field test, no significant difference was detected in the distance moved in *Bcl11a* cko mice compared to controls, indicating that spontaneous motor behaviour is not affected in *Bcl11a* cko mice **(**data analysis performed by Prof. Dr. Stephan Baader, **Figure 29A)**.
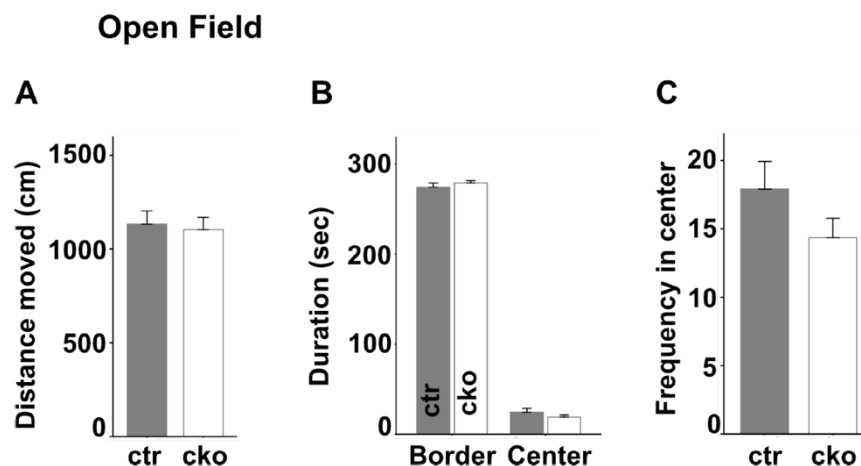
Open Field

Figure 29. Inactivation of *Bcl11a* in mDA neurons did not compromise the Bcl11a cko mice performance in the open field. (A-C) Open field test (5-minute time window) revealed no significant difference between *Bcl11a* cko^flox (cko) and control mice (ctr) in distance moved **(A)**, in time spent in the center or border area **(B)** or the frequency of entering the center **(C)**. Data analysis performed by Prof. Dr. Stephan Baader. *Bcl11a* cko (n= 12) and control mice (n= 13). Error bars indicate mean +/- SEM.

By monitoring the activity in the centre of an open field, anxiety-and depressive-like behaviour associated with decreased DA release from the VTA can be assessed (Yacoubi et al., 2003; Tye et al., 2013). No change was detected in the frequency of crossing into the centre and time spent in centre or border area in the open field between *Bcl11a* cko and control mice, indicating that mutant mice did not have an increased level of depressive behaviour or anxiety **(Figure 29B-C)**. Since inhibition of VTA-mDA neurons has been shown to lead to a decreased preference for social novelty (Bariselli et al., 2018), a social recognition test was performed to assess the ability of *Bcl11a* cko mice to distinguish familiar and unfamiliar mice. No significant alteration was found in the behaviour of *Bcl11a* cko mice compared to controls **(**data analysis performed by Prof. Dr. Stephan Baader, **Figure 30A-F)**. In particular, there was no difference between *Bcl11a* cko mice and controls in the time spent in each chamber when all the chambers were empty **(Figure 30A)**, when an intruder mouse was placed in one of the chambers **(Figure 30B)** and when both a familiar and unfamiliar mouse were placed in each

of the chambers **(Figure 30C)**. Accordingly, there was no difference in the transitions from the chambers containing familiar and unfamiliar mice between *Bcl11a* cko and control mice **(Figure 30D)**. The distance moved by *Bcl11a* cko and controls did not show any significant difference during the whole performance of the social recognition test **(Figure 30E)**. Moreover, no significant difference was detected between mutant and control mice in the time spent around the cages in which a familiar or stranger mouse was placed **(Figure 30F)**.
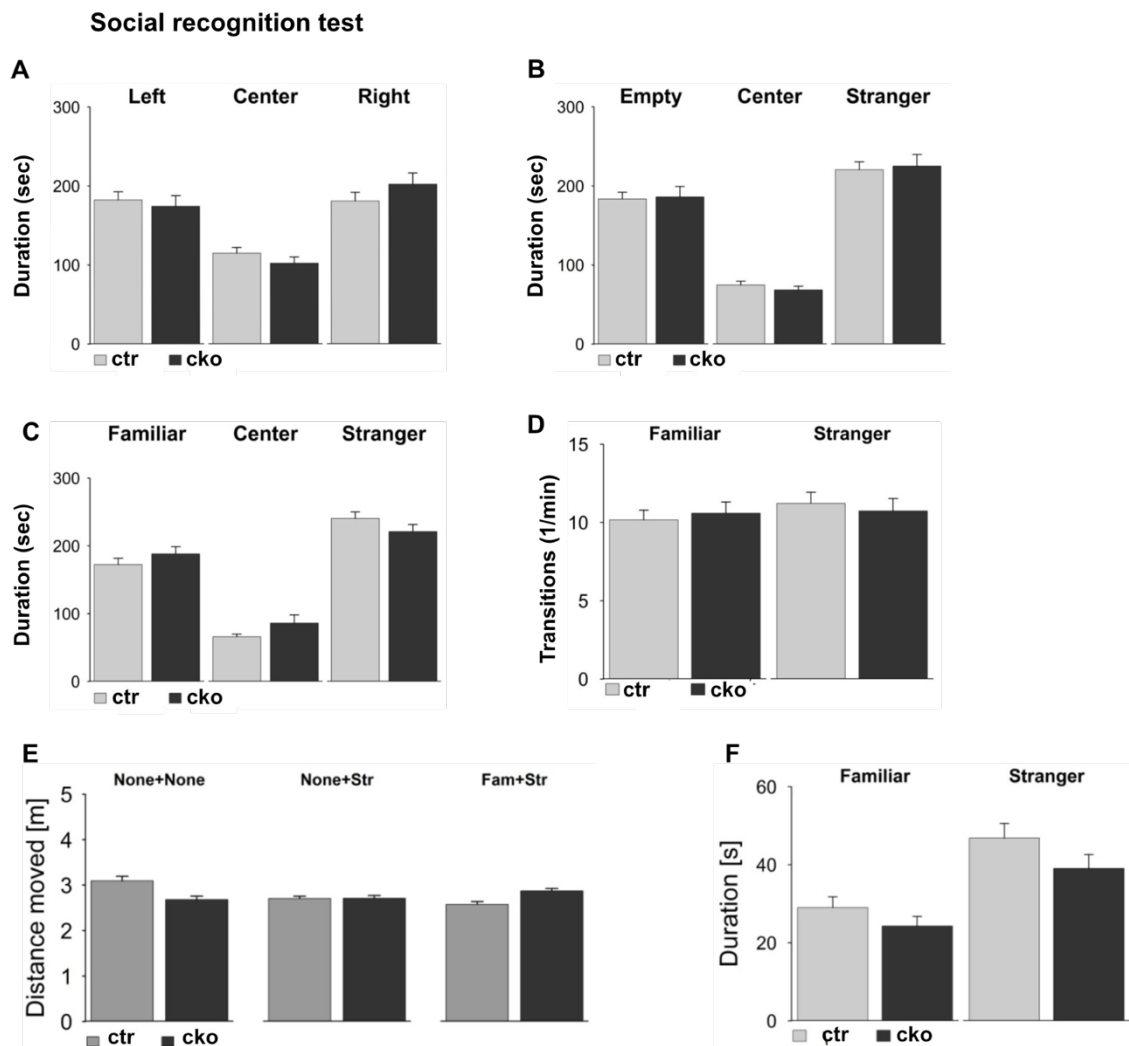
Figure 30. Inactivation of *Bcl11a* in mDA neurons did not compromise the *Bcl11a cko* mice performance in the social recognition tests. (A-F) Social recognition test revealed no significant difference between *Bcl11a* cko and control mice in duration of time spent in each chamber for every condition **(**empty chambers or in presence of familiar and stranger mice, **A-C)**, in the transitions between the chambers in which familiar and/or stranger mice were placed **(D)** as well as in the distance moved in every condition **(**no intruders or in presence of familiar and/or stranger mice, **E)**. The duration of time spent around cages with familiar and stranger mouse did not differ between *Bcl11a* cko and control mice **(F)**. Data analysis performed by Prof. Dr. Stephan Baader. *Bcl11a* cko (n= 12) and control mice (n= 13). Error bars indicate mean +/- SEM.

Tasks in which DA release from SN-mDA neurons is thought to play a prominent role where analysed as well. DA release in the striatum is crucial for voluntary movement and motor skill learning (Dodson et al., 2016; Wu et al., 2019). Motor coordination and balance were examined by monitoring the ability of mice to cross a balance beam (Luong et al., 2011). No difference was found in the time taken to cross the bar for *Bcl11a* cko and control mice **(data analysis performed by Prof. Dr. Stephan Baader, Figure 31A)**. An accelerating rotarod test was performed in order to examine whether motor skill learning was altered in *Bcl11a* cko mice (Costa et al., 2004). A continuous increase in the time to fall over a 5-day training period was found in control mice, indicating that they improved their performance over time. In contrast, *Bcl11a cko* mice did not show any improvement in their performance over time, indicating that they were not able to learn this motor task within the 5-days training period **(**data analysis performed by Prof. Dr. Stephan Baader, **Figure 31B)**. Taken together, these results show that the inactivation of *Bcl11a* in mDA neurons results in defects in skilled motor learning, suggesting that mDA neurons may be functionally impaired in the absence of *Bcl11a*.
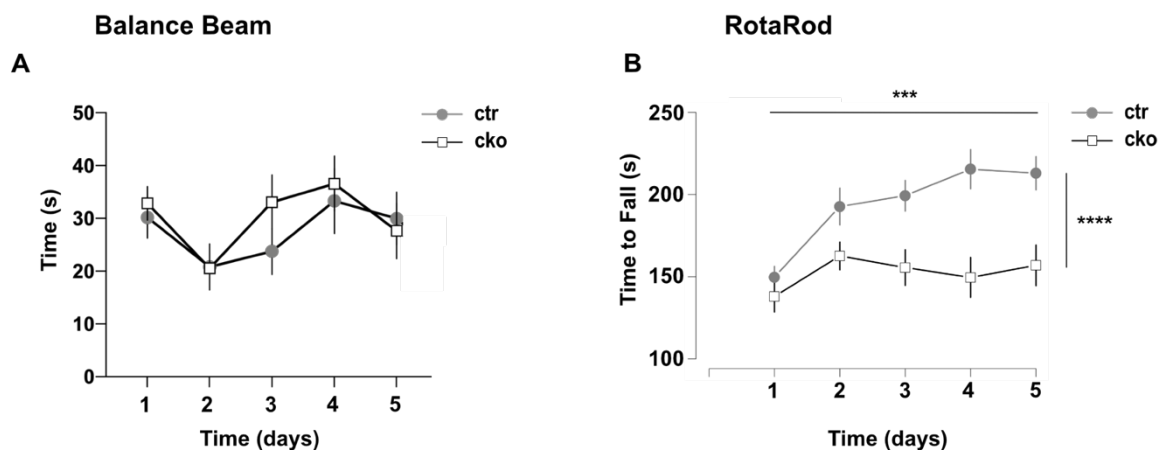
Figure 31. Inactivation of *Bcl11a* in mDA neurons results in specific defects in motor behaviour. (**A**) Mice had to balance on a beam towards a food reward. The test was performed on 5 consecutive days. There was no significant difference between *Bcl11a* cko and control mice in their ability to cross a balance beam in any of the trials. **(B)** The rotarod test revealed that *Bcl11a* cko mice were not able to learn the motor task, since unlike in control mice the time to fall did not increase in *Bcl11a* cko mice within the 5 days of the trial period. *Bcl11a* cko (n= 12) and control mice (n= 13). Significance was determined by two-way ANOVA. ***$p < 0.001$, **** $p < 0.0001$. p=7.226e-10 for genotype, p=0.0002017 for days and p=0.0076354 for interdependence between days and genotypes. Data analysis performed by Prof. Dr. Stephan Baader. Error bars indicate mean +/- SEM.

4.6 Loss of *Bcl11a* enhances vulnerability to α-synuclein toxicity

Next, the role that BCL11A might play in the context of neurodegenerative process and neuronal challenges affecting SNc-mDA neurons was investigated.

Figure 32. *Bcl11a* cko mice show increased neuronal vulnerability to α-synuclein toxicity. (A) Schematic showing the unilateral intraparenchymal injection of adeno-associated 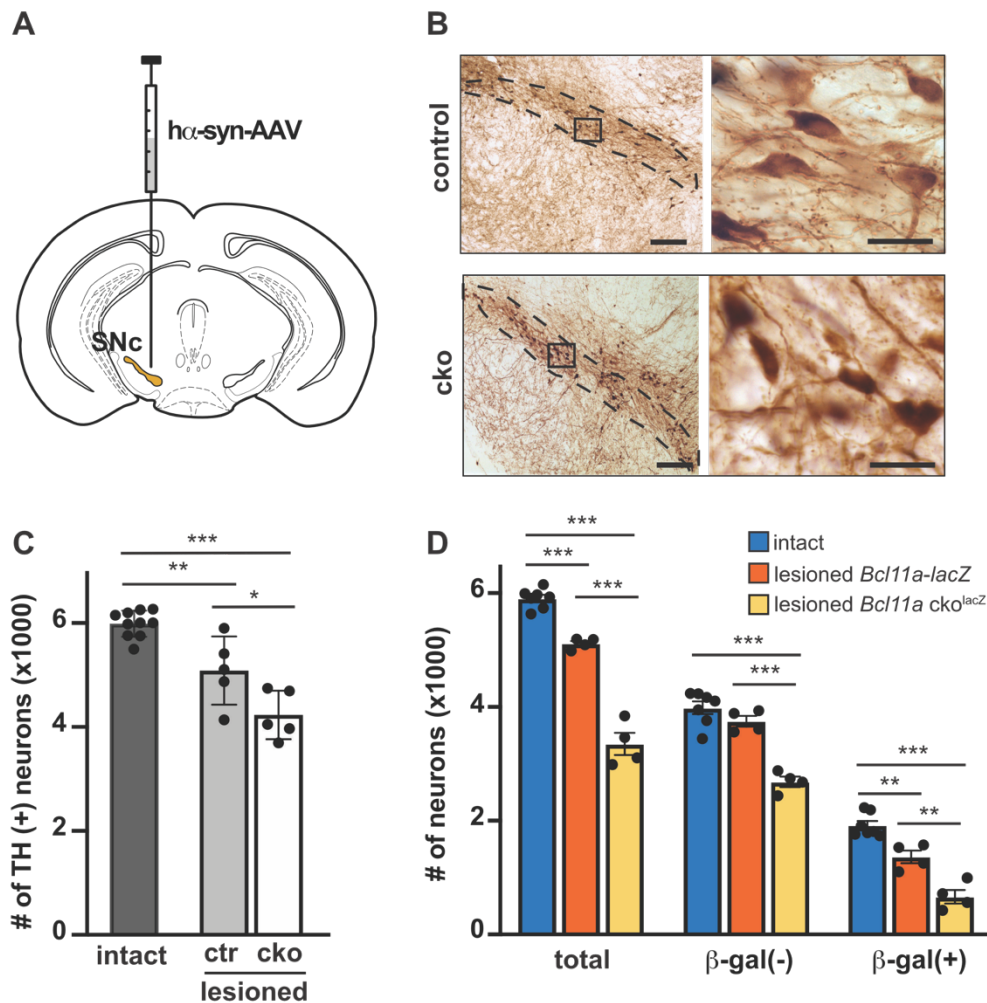viral vectors (AAVs) carrying the DNA for human α-synuclein (hα-syn) into the SNc. Animals were sacrificed 8 weeks after this treatment. **(B)** Immunostaining for human α-synuclein on midbrain coronal sections comprising the SNc (delineated with dotted lines at low magnification). Representative images from a control and a *Bcl11a* cko animal show neuronal expression of the transduced protein. The right panels show a higher magnification of the boxed areas in the left panels (low magnification). **(C)** Midbrain sections from control and *Bcl11a* cko mice were immunostained for TH and TH-immunoreactive neurons were counted stereologically in the intact and lesioned SNc of control (n=5) and *Bcl11a* cko (n=5) mice. Intact side values from control and cko animals were pooled together. A significant decrease in the number of TH positive neurons was found in the lesioned SNc of control mice. This decrease was even higher in the lesioned SNc of *Bcl11a* cko mice. **(D)** Midbrain sections from *Bcl11a-lacZ* control (n=4) and *Bcl11a* cko^{lacZ} (n=4) mice were stained with for TH and β-gal. Total neurons (β-gal negative and β-gal positive TH cells), β-gal(-) neurons (TH cells negative for β-gal)and β-gal(+) neurons (cells double positive for TH and β-gal) were counted using confocal stereology. Counts made in the intact SNc showed no difference between the two groups of animals and were therefore pooled together (total). A significant decrease in the number of TH$^+$ β-gal$^+$ neurons was found in the lesioned SNc of both control and *Bcl11a* cko mice, with the loss being significantly more pronounced in *Bcl11a* cko mice. In *Bcl11a* cko mice, a significant decrease in cell numbers was also found in Th positive neurons negative for β-gal. Experiments were performed by Dr. Ayse Ulusoy. Significance was determined by one-way ANOVA followed by Tukey's *post hoc* test for multiple comparisons. Error bars indicate mean +/- SEM. Scale bars: 100 µm **(**low magnification panels in **B)** and 20 µm **(**higher magnification panels in **B)**.

The protein α-synuclein plays a key role in the pathogenesis of Parkinson's and other human neurodegenerative diseases (Goedert et al., 2013). α-synuclein overexpression in animal

models is associated with Parkinson-like pathology, including the degeneration of SNc-mDA neurons (Ulusoy & Di Monte, 2013). Therefore, a single intraparenchimal injection of viral vectors (rAAV) carrying the DNA for human α-synuclein was performed into the right SNc of *Bcl11a* cko and control mice (adult mice, 5-8 months old) **(rAAV injections, immunostainings and stereological cell counts performed by Dr. Ayse Ulusoy, Figure 32A)**. Using this approach, a robust human α-synuclein overexpression was obtained within SNc-mDA neurons. Immunostaining for human α-synuclein on midbrain sections containing the SN did not reveal any difference in the overexpression between control and *Bcl11a* cko mice **(Figure 32B)**. Eight weeks after the rAAV injection mice were sacrificed and an immunostaining for TH was performed on midbrain sections containing both the intact (left side) and lesioned SNc (right side). Labelling was less robust in the lesioned right SNc, in both control and *Bcl11a* cko mice. Of note, the loss of TH immunoreactivity appeared to be more pronounced in *Bcl11a cko* mice (data not shown). The number of neurons positive for TH was counted using a stereological method. Cell counts in the intact SNc were similar between control and *Bcl11a* cko mice, consistent with previous quantifications in younger animals **(see Figure 26)**. For this reason, counts in the intact SNc of control and mutant mice were averaged together as normal values (5,988 ± 79.4 cells). As a consequence of human α-synuclein expression, a 15% reduction of TH positive cells was found in the lesioned SNc of control mice (5,086 ± 292.8 cells). Of note, this loss was significantly higher in the SNc of *Bcl11a cko* mice (4,231 ± 208.2 cells) **(Figure 32C)**. Cell counts of the total number of Nissl-stained neurons were also performed, in order to understand whether the decrease in TH positive cells after rAAV injection were due to a TH down-regulation rather than actual cell degeneration. This number was significantly decreased in the lesioned SNc of both control and cko mice (data not shown). The significantly higher loss of TH positive and Nissl positive neurons in the SNc of *Bcl11a* cko mice compared to controls was also confirmed in an older group of animals (aged mice, 14-16 months old) using the same experimental paradigm (data not shown). These results reveal that in the absence of *Bcl11a* the SNc-mDA neurons vulnerability to α-synuclein toxicity is markedly enhanced, supporting the notion that *Bcl11a* expression is associated with transcription of genetic information involved in neuroprotective pathways. In order to understand whether the α-synuclein induced neuronal loss occurs preferentially in *Bcl11a*-expressing (β-gal positive) SNc-mDA neurons, experiments using the same paradigm of rAAV-induced human α-synuclein overexpression were carried out in *Bcl11a* cko[lacZ] and *Bcl11a*[flox/lacZ] control mice (both adult and aged mice). Human α-synuclein toxicity caused a more severe loss of TH-positive neurons in the SNc of *Bcl11a* cko[lacZ] mice (from 5,906 ± 64.4 to 3,349 ± 193.3 cells) as compared to *Bcl11a*[flox/lacZ] controls (from 5,906 to 5,114 ± 47.9 cells) **(Figure 32D**, "total" values**)**, confirming the results obtained in *Bcl11a* animals without the lacZ allele **(Figure 32C)**. In *Bcl11a*[flox/lacZ] control mice, confocal stereological counts were able to

distinguish the effects of α-synuclein overexpression on *Bcl11a*-expressing SNc-mDA neurons (positive for both TH and β-gal) and SNc-mDA neurons that did not show *Bcl11a* expression (positive for TH, but β-gal negative). In control mice, counts of β-gal-positive cells revealed that 29% of *Bcl11a*-expressing mDA neurons degenerated (from 1,919 ± 78.3 to 1,365 ± 113.1 cells), whereas only 6% of β-gal-negative neurons were lost as a result of α-synuclein overexpression (from 3,986 ± 111.5 to 3,748 ± 95.1 cells) **(Figure 32D)**. These data indicate that *Bcl11a* expression characterizes a subpopulation of nigral DA neurons highly susceptible to α-synuclein-induced damage. In *Bcl11a* cko[lacZ] animals, α-synuclein toxicity killed almost 65% of β-gal-positive cells (from 1,919 to 664 ± 117.0 cells) and 33% of β-gal-negative cells (from 3,986 to 2,685 ± 91.4 cells) **(Figure 32D)** resulting in a more dramatic toxic effect. These data suggest that, in the absence of *Bcl11a* expression, β-gal-positive cells became even more vulnerable to neurodegeneration, consistent with a protective role of *Bcl11a*. Interestingly, a more severe neurodegenerative effect was observed in *Bcl11a* cko[lacZ] mice, not only on β-gal-positive but also β-gal-negative neurons. This latter finding suggests that inactivation of *Bcl11a* expression may have cell non-autonomous effects and result in widespread deleterious consequences for nigral tissue integrity.

The next set of experiments were conducted to investigate whether the severe loss of SNc *Bcl11a*-mDA neurons in α-synuclein overexpression model results in reduced TH density in the areas innervated by this subpopulation. SNc mDA neurons send their axons to the dorsal striatum, while the projections to most areas of the TS originate from the SNl (Menegas et al., 2015; Menegas et al., 2018). However, the precise anatomical location of mDA neurons projecting to the most ventral part of the TS has not been determined (Menegas et al., 2015; Menegas et al., 2018). Thus, these neurons could be localized in the SNc rather than the SNl. Indeed, based on our anterograde viral tracing studies, Bcl11a-mDA neurons in the medial and lateral SNc are sending projections to the ventral part of the TS **(**see **Figure 20C-F)**. Thus, for this analysis the intensity of TH immunostaining was analysed in the ventral (TSv) and dorsal part (TSd) of the tail of the striatum **(Figure 33A-B)** and in the rostral dorsal striatum **(Figure 33E-F)** on the intact side and compared it to the intensity on the contralateral injected site. This analysis was performed in two different groups of animals, referred as adult (5-8 months old) and aged mice (14-16 months old). A significant decrease in the TH intensity was detected in the TSv, but not in the TSd, of *Bcl11a* cko mice, in both the adult **(Figure 33C)** and aged group **(Figure 33D)**. There was no reduction in the TH fibre intensity in control adult **(Figure 33C)** and aged mice **(Figure 33D)**, for both the TSv and the TSd. This could be likely due to the less severe loss of *Bcl11a*-mDA neurons in control mice compared to *Bcl11a* cko mice.TH intensity was not reduced in the anterior dorsal striatum, in controls as well as in *Bcl11a* cko mice of both adult **(Figure 33G)** and aged group **(Figure 33H)**. These data confirm

a severe and largely specific reduction of the *Bcl11a*-mDA population in *Bcl11a* cko mice upon α-synuclein overexpression and suggest that the projections to the TSv might originate from mDA neurons in the SNc.
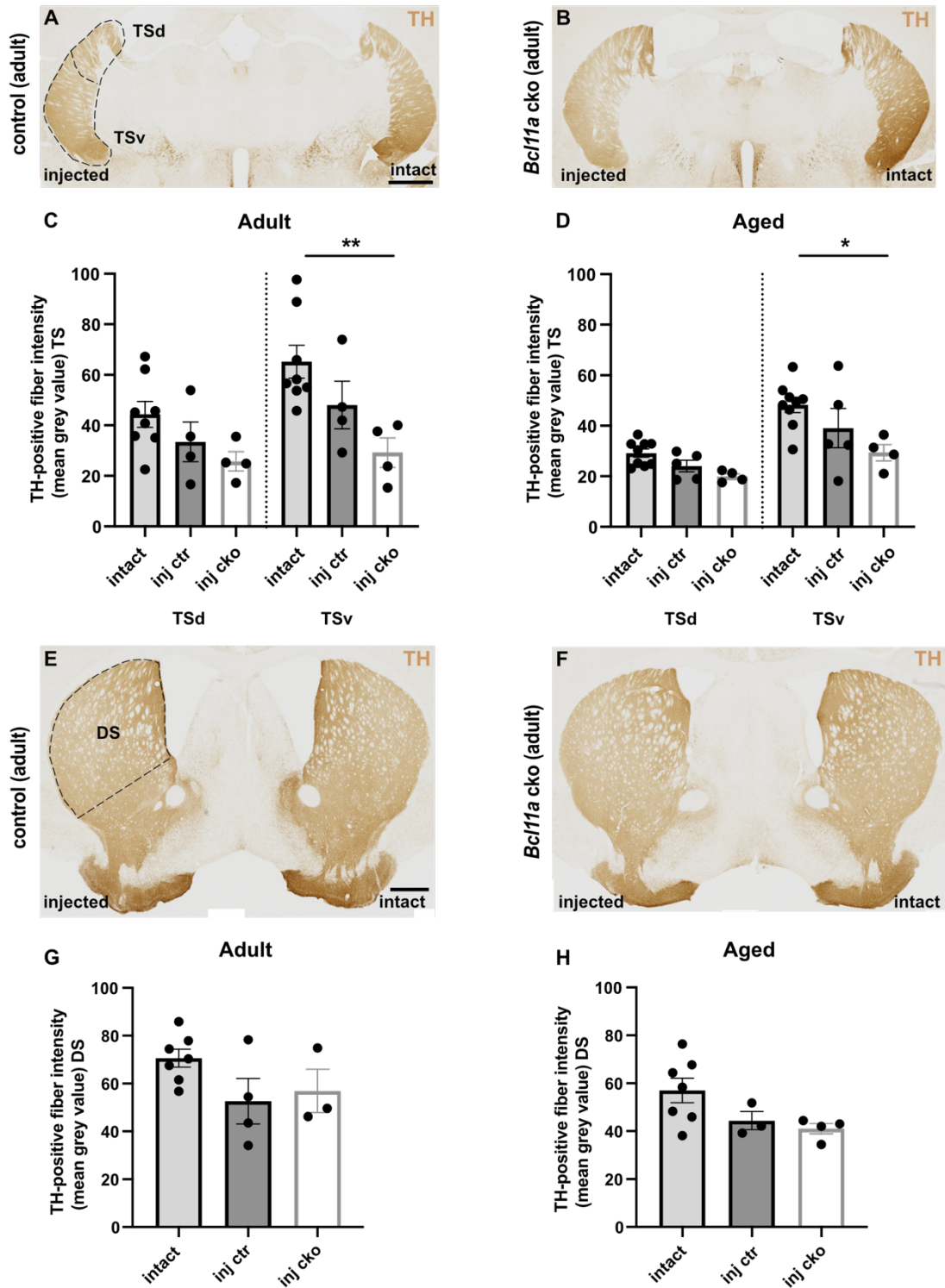

Figure 33. (Figure legend on next page)

Figure 33. *Bcl11a* cko mice show a significant decrease in the TH intensity in the ventral part of the tail of the striatum after α-synuclein overexpression into the SNc. (A,B) Immunostaining for TH on forebrain sections comprising the TS (both injected and intact side) of control **(A)** and *Bcl11a* cko mice **(B)** in which human α-synuclein was unilaterally overexpressed in the SNc. **(C,D)** Quantification of TH fibre intensity in the intact and injected dorsal (TSd) and ventral part of the TS (TSv) of adult **(C)** and aged **(D)** *Bcl11a* cko and control mice. Intact side values from control and *Bcl11a* cko animals were pooled together. A significant reduction in TH immunoreactivity was detected in the injected TSv compared to the intact side, in both adult **(C)** and aged *Bcl11a* cko mice **(D)**. Mice analysed (adult group: control n=4 mice and cko n=4 mice; aged group: control n=5 mice and cko n=4 mice). Significance was determined with ordinary one-way ANOVA followed by Turkey´s *post hoc* test for multiple comparisons. *p < 0.05, ** < 0.01. **(E,F)** Immunostaining for TH on forebrain sections comprising the DS (both injected and intact side) of control **(E)** and *Bcl11a* cko mice **(F)** in which human α-synuclein was unilaterally overexpressed in the SNc. **(G,H)** Quantification of TH fibre intensity in the intact and injected DS of adult **(G)** and aged **(H)** *Bcl11a* cko and control mice. Intact side values from control and *Bcl11a* cko animals were pooled together. No significant reduction in TH immunoreactivity was detected in the injected DS compared to the intact side, in both adult **(G)** and aged *Bcl11a* cko mice **(H)**. Mice analysed (adult group: control n=4 mice and cko n=3 mice; aged group: control n=3 mice and cko n=4 mice). Error bars indicate mean +/- SEM. Scale bar: 500 µm **(A,B,E,F).**

5. DISCUSSION

5.1 *Bcl11a* is expressed in subpopulations of mDA neurons

mDA neurons are a heterogeneous group of neurons differing in their anatomical location, their projection targets, their gene expression profiles, their electrophysiological properties and their influence on multiple aspects of behaviour (Farassat et al., 2019; Morales & Margolis, 2017; Poulin et al., 2020; Roeper, 2013). How these different levels of mDA neurons diversity are related to each other is largely unknown but it has been the subject of extensive research in the last decade. In fact, several recent studies have provided detailed characterisation of the expression of specific markers in the midbrain that define functionally relevant subsets of mDA neurons with specific projection targets in the forebrain (Bimpisidis et al., 2019; Heymann et al., 2020; Khan et al., 2017; Kramer et al., 2018). For example, the combinatorial expression of the neurogenic differentiation factor-6 (*Neurod6*) and of the gastrin-releasing peptide (*Grp*) defines an mDA neurons subpopulation residing in the ventromedial VTA that sends projections to the medial shell of the NAc and has noncanonical physiological properties (Kramer et al., 2018). *Neurod6* identifies a subset of VTA-mDA neurons expressing *Otx2*, *Aldh1a1* and *Calbindin* and projecting to the intermediate and dorsal region of the LS (Khan et al., 2017). Based on the currently available single-cell gene expression studies, at least 7 different molecularly defined mDA subgroups have been identified. Of those, one circumscribes neurons located in the SNc, lateral VTA and RRF, one is restricted to the linear nucleus, two are restricted to the SN and three are located within the medioventral VTA (Poulin et al., 2020). However, how and whether this cellular diversity is generated during development is not yet fully understood.

In this thesis the expression of the transcription factor *Bcl11a* has been analysed in the ventral midbrain starting in embryogenesis and throughout adulthood. BCL11A starts to be expressed in some differentiated mDA neurons starting at E12.5 and its expression is detected in a larger mDA neurons subpopulation of the forming VTA and SN at E14.5 and E15.5. In the adult mouse brain *Bcl11a* expression defines subsets of mDA neurons in the SN, VTA, RRF and CLi. About 20% and 40% of SN- and VTA-mDA neurons are *Bcl11a*-positive, respectively. In the more caudal RRF and CLi nuclei, *Bcl11a* is expressed in about 30% of DA neurons. Of note, about 50% of the *Bcl11a*-positive cells found within SN, VTA and RRF and about 60% in the CLi are TH-negative, indicating the presence of a large number of non-DA neurons within the ventral midbrain expressing this transcription factor. These cells might be glutamatergic or GABAergic neurons distributed within the different mDA nuclei. However, it

is not possible to confirm this hypothesis based on the data shown in this thesis and a more detailed analysis would have to be performed to assess the molecular profile of these cells. *BCL11A* expression was also analysed in data obtained from droplet-based single cell RNA sequencing of human induced pluripotent stem cell (hiPSC)-derived mDA neurons generated by our collaborators (Fernandes et al., 2020). In these cultures, *BCL11A* expression defines a subset within SNc-like and VTA-like mDA neurons, thus confirming the results obtained from the developing and adult mouse brain (Tolve et al., 2021).

5.2 The *Bcl11a*-mDA subpopulation contributes to several known molecularly defined mDA populations

In this study, *Bcl11a* expression was analysed within the previously identified ALDH1A1- and CALB1-expressing mDA subpopulations of the adult mouse brain (Liu et al., 2014; Poulin et al., 2014). ALDH1A1-expressing mDA neurons are located in the ventral VTA and in the ventral tier of the SNc. CALB1-expressing neurons are found throughout the VTA and in the dorsal tier of the SNc (Thompson, 2005; Wu et al., 2019). When analysed in both SN and VTA, ALDH1A1 expression was detected in about 20% of *Bcl11a*-expressing mDA neurons. Within the VTA, 70% of *Bcl11a*-expressing mDA neurons co-express the subtype marker CALB1. Of note, even if *Bcl11a* expression is mainly detected in the SNl and the dorsal tier of the SNc, where also CALB1-positive mDA neurons are found, less than half of the *Bcl11a*-expressing neurons express CALB1 in the adult brain. These results indicate that *Bcl11a*-expressing mDA neurons constitute a distinct mDA subpopulation that does not correspond to already known mDA neuronal subpopulations (Poulin et al., 2020).

These data were also confirmed by a differential expression analysis in hiPSC-derived mDA neurons performed by our collaborators (Tolve et al., 2021). In fact, in these cultures SNc-like and VTA-like hiPSC-derived mDA neurons expressing *BCL11A* have a distinct gene expression profile that does not fall within any of the seven previously characterised mDA subclasses (Poulin et al., 2020).

5.3 *Bcl11a*-mDA neurons form a highly specific subcircuit in the midbrain dopaminergic system

Recent studies have shown that specific subcircuits within the DA system modulate specific aspects of behaviour, thus suggesting that the targeting of a set of substructures within the DA projection targets by specific DA subcircuits may encode a precise behavioural output (Engelhard et al., 2019; Heymann et al., 2020; Menegas et al., 2018). Whether genetically

determined populations of mDA neurons are consistent with such specific behaviours has started to be examined only recently (Heymann et al., 2020).

In this study, projections of *Bcl11a*-expressing mDA neurons have been examined using an intersectional fate mapping approach together with a viral-based anterograde tracing and CTB-based retrograde tracing techniques. The results obtained indicate that despite the broad distribution of *Bcl11a*-mDA neurons across different anatomical and molecularly defined mDA subpopulations, *Bcl11a*-expressing mDA neurons establish a highly selective innervation pattern within the known mDA projection targets.

With the intersectional fate mapping approach, *Bcl11a*-expressing mDA neurons and their projections to forebrain target areas were labelled at E15.5 with a reporter allele expressing EGFP (Ai82D) and later analysed in the adult mouse brain. EGFP-positive cells were found throughout the VTA, in the medial and dorsal SNc, as well as in the SNI, CLi and RRF, thus reflecting the endogenous BCL11A expression. *Bcl11a*-expressing mDA neurons of the VTA are sending the strongest projections to the OT. Moreover, they are innervating the ventral and lateral portion of the NAc shell and the intermediate part of the LS. Interestingly, the NAc core is devoid of projections arising from *Bcl11a*-expressing mDA neurons of the VTA. Lack of projections from this subset of VTA-mDA neurons was also found in the mPFC and BLA. *Bcl11a*-mDA neurons of the SN show a strikingly selective innervation of the caudal DMS and of the ventral TS. The rostral DMS and the DLS are devoid of projections, while the dorsal TS is innervated by a smaller number of fibres arising from *Bcl11a*-expressing SN-mDA neurons. Of note, the specificity of the innervation pattern observed in the adult brain has also been confirmed in E18.5 embryonic brains for all the areas targeted by *Bcl11a*-expressing mDA neurons. The only exception is the NAc shell that does not show such a strong innervation at this time point, thus suggesting that these projections might develop later. Although with this approach the EGFP expression in the midbrain is restricted to mDA neurons, EGFP positive fibres negative for TH are also found in brain regions that are not innervated by mDA neurons. Most likely, this is due to leakiness of the Ai82D reported allele that can lead to the expression of the EGFP protein in neurons (and therefore in their projections) that are positive for *Bcl11a* but are not DA. However, this did not interfere with the characterisation performed in this study since only projections that were double positive for EGFP and the DA marker TH were analysed. Although the intersectional fate mapping is an accurate and reliable tool to label *Bcl11a*-expressing mDA neurons projections during embryogenesis, it failed to label enough *Bcl11a*-expressing mDA neurons when performed in adult mice. Therefore, the specificity of *Bcl11a*-mDA surcircuits was confirmed by viral-based anterograde tracing approaches that allowed to visualise separately the innervation patterns established by *Bcl11a*-expesing mDA neurons located in the VTA and SN.

A complementary retrograde tracing approach has been used in this study to confirm the connectivity of *Bcl11a*-expressing mDA neurons. For this purpose, fluorophore-conjugated CTB has been injected in different forebrain target areas and its retrograde transport from the injection site has allowed to label the cell bodies of neurons projecting to these areas, including *Bcl11a*-expressing mDA neurons. However, like most conventional tracers, CTB transport is to some extent bidirectional (Noseda et al., 2010). Moreover, it does not allow the monosynaptic tracing of genetically defined neuronal subpopulations in a Cre-dependent manner. Therefore, a different experimental approach needs to be used to confirm the *Bcl11a*-mDA subpopulation connectivity in a retrograde-like manner. For example, one possibility would be to use rabies viral vectors that allow the mapping of neurons (in this case, Bcl11a-expressing mDA neurons) that are directly presynaptic to the selected target region (e.g. NAc, OT, TS) in a Cre-dependent manner.

This specific innervation pattern established by the *Bcl11a*-expressing mDA subpopulation suggests that this genetically defined subgroup may modulate a specific subset of DA-modulated behaviours. From an evolutionary standpoint, the mDA system may consist of different modules with different functions that were built on top of a basic DA system mainly concerned with basic behaviour just as food-seeking and reward behaviour (Schultz, 2019). If there are such modules one would expect that they are genetically defined by the expression of specific transcription factors or sets of transcription factors. Bcl11a could potentially define such a behavioural-anatomical module and it will be interesting to investigate in the future whether mDA neurons that are characterized by *Bcl11a*-expression in the SN and VTA form such a functional module within the mDA system.

5.4 Function of BCL11A in developing and mature mDA neurons

BCL11A is expressed throughout the CNS in many different neuronal types (Allen Brain Atlas), but its function has been studied only in the spinal cord and in the cortex so far (Simon et al., 2020). BCL11A is required in dorsal spinal neurons for terminal differentiation and morphogenesis (John et al., 2012). In the cortex, BCL11A regulates polarity and migration of upper layer cortical projection neurons and it specifies the subtype identity in deep-layer cortical neurons (Wiegreffe et al., 2015; Woodworth et al., 2016). Furthermore, BCL11A is important for the acquisition of sub-cerebral fate and it controls the acquisition of sensory area identity and the establishment of sensory input fields in the developing neocortex (Canovas et al., 2015; Greig et al., 2016). It is still not clear whether BCL11A exerts its role as transcriptional repressor or if it acts as part of the chromatin remodelling complex in these neurons.

In this study, *Bcl11a* has been specifically knocked-out in mDA neurons and its inactivation led to a medial-to-lateral and rostral-to-caudal shift of Bcl11a-mDA cell bodies in the SN and VTA, respectively. Despite changes in the anatomical positioning of *Bcl11a*-mDA cell bodies in the VTA and SN, no difference was detected in the innervation of *Bcl11a*-mDA neurons forebrain target region. However, the methods used in this study might be not precise enough to detect eventual changes in the innervation patter caused by the difference in positioning of this relatively small mDA subpopulation. These data suggest that BCL11A might regulate the expression of factors that control the migration of SN- and VTA-mDA neurons. BCL11A has been shown to control migration of cortical projection neurons through regulation of the cell adhesion molecule Sema3c (Wiegreffe et al., 2015). In fact, BCL11A is a direct negative regulator of Sema3c transcription. In *Bcl11a*-deficient neurons the expression of Sema3c is increased as they fail to switch from multipolar to bipolar morphology, thus resulting in impaired radial migration (Wiegreffe et al., 2015). However, the expression of Sema3c has not been detected in mDA neurons (Kolk et al., 2009). The analysis of the scRNAseq data carried out by our colleagues for both *BCL11A*-positive and *BCL11A*-negative cells in the SNc-like and VTA-like hiPSC-derived mDA neurons revealed differential expression of genes encoding for components of the cytoskeleton or cytoskeleton-associated proteins (Tolve et al., 2021). For example, genes encoding doublecortin-like kinase, neuronal navigator 1 and tubulin beta 2 chain were found to be differentially expressed in *BCL11A*-positive SNc-like human iPSC derived mDA neurons. Tubulin beta 2 chain is also differentially expressed in VTA-like neurons from the same cultures, together with Rac1 and the microtubule associated protein 1B. All the above-mentioned molecules have been shown to be involved in different aspect of neuronal migration (Breuss et al., 2017; Deuel et al., 2006; Kawauchi, 2015; Koizumi et al., 2006; Sánchez-Huertas et al., 2020; Villarroel-Campos & Gonzalez-Billault, 2014). Thus, one hypothesis is that the inactivation of *Bcl11a* in mDA neurons results in altered neuronal migration and positioning of mDA neurons in the adult mouse brain due to changes in cytoskeleton dynamics.

5.5 Consequences of *Bcl11a*-inactivation in mDA neurons on behaviour

While changes in cell body positioning in the absence of *Bcl11a* affected both mDA neurons in the SN and VTA, behavioural changes in *Bcl11a* cko mice were detected exclusively in tasks in which DA release from SN mDA neurons plays a prominent role.
The assessment through the open field test of depressive- and anxiety-like behaviour associated with DA release from the VTA revealed no difference between control and *Bcl11a*

cko mice. Moreover, mice from both groups showed no difference in the distance moved indicating that the general locomotor activity is not affected in the absence of *Bcl11a*.

The chemogenetic inhibition of VTA-mDA neurons has been shown to attenuate exploration towards non-familiar conspecifics and to interfere with the reinforcing properties of non-familiar confamiliar interaction in mice (Bariselli et al., 2018). The inactivation of *Bcl11a* in mDA neurons did not compromise the *Bcl11a cko* mice performance in a social recognition test, indicating that DA release from the VTA modulating this aspect of behaviour is not affected by the loss of *Bcl11a*.

Dopamine release from SN-mDA neurons in the striatum is crucial for both voluntary movement and motor skill learning (Dodson et al., 2016; Wu et al., 2019). In this study, motor coordination was examined by monitoring the ability of mice to cross a balance beam. The results obtained show that motor coordination and balance are not affected in *Bcl11a* cko mice. However, the rotarod performance revealed a specific behavioural impairment in skilled motor learning in the absence of *Bcl11a*. Motor skill learning occurs in two sets of loop circuits: cortex-basal ganglia and cortex-cerebellum (Hikosaka et al., 2002). Since *Bcl11a* is specifically inactivated in mDA neurons in the mouse model used in this study, this behavioural phenotype must be caused by functional changes in SN-mDA neurons rather than by deficits in other motor circuits areas like the cerebellum or motor cortex. Learning of motor skills is thought to be mediated by DA release from SN-mDA neurons into the dorsal striatum.

It has been proposed that DA release in the associative DMS is necessary for early motor learning, while DA release in the sensorimotor DLS is required for gradual motor skills acquisition (Durieux et al., 2012). Based on this model and the highly specific innervation of the DMS by SN-mDA neurons expressing *Bcl11a* that was found in this study, the deficit in motor learning observed in *Bcl11a* cko mice might be due to their inability to initiate the learning of skilled motor behaviour. Strikingly, impairment in motor skill learning in the rotarod test performance was also found in mice lacking the expression of *Aldh1a1* specifically in mDA neurons (Wu et al., 2019). Of note, *Aldh1a1* expression is restricted to mDA neurons localised in the ventral tier of the SNc that innervate exclusively the DLS. These data indicate the possibility that a reduced DA release in both DLS and DMS, and thus defects in both phases of motor learning lead to similar defects in skilled motor learning. Moreover, the inability of *Bcl11a* cko mice to learn the rotarod task might be also due to a deficit in motivated behaviour. However, since these mice did not show any other altered behavioural performance (open field, social recognition test, balance beam), this possibility is unlikely to be the cause of impaired skill learning.

Due to the highly specific innervation pattern of *Bcl11a*-mDA neurons in the forebrain and the fact that *Bcl11a*-mDA neurons comprise only a subset of mDA neurons, it was not possible to address in this study the nature of these functional changes. One possible scenario would be

that altered neuronal activity results in decreased dopamine release in the target areas of *Bcl11a*-mDA neurons and that these alterations are severe enough to elicit a behavioural phenotype.

So far, a role of BCL11A in the regulation if neuronal activity has not been described. However, studies on the closely related transcription factor BCL11B have shown that its inactivation in the adult brain causes changes in hippocampal synapse formation and maintenance as well as electrophysiological impairments (De Bruyckere et al., 2018; Simon et al., 2016). Another line of evidence supporting a function of BCL11A in the regulation of neuronal activity comes from the fact that haploinsufficiency for *BCL11A* in humans causes intellectual disabilities and that *BCL11A* is a risk gene for autism spectrum disorders. Thus, BCL11A might influence neuronal activity by affecting brain development as well as by regulating the expression of important genes regulating neuronal functions in mature neurons.

5.6 Vulnerability of *Bcl11a*-neurons to degeneration

The ventral tier of the SNc is the most affected subregion of the ventral midbrain in terms of mDA neuronal cell loss in animal models of Parkinson´s disease and in human PD patients (Kordower et al., 2013). Studies on MPTP mouse models of PD have identified this vulnerable mDA population located in the SNc ventral tier as being positive for ALDH1A1 (Poulin et al., 2014). On the other hand, in α-synuclein transgenic mice (another PD model), degeneration of SNc-mDA neurons occurs mainly in the ALDH1A1-negative subpopulation located in the dorsal SNc that is also prone to cytotoxic α-synuclein aggregation (Liu et al., 2014). Of note, the topographic pattern established by *Aldh1a1* in the α-synuclein mouse model has been shown to be conserved in the human SNc (Liu et al., 2014).

In this study an α-synuclein overexpression mouse model was used to mimic PD. As a result, *Bcl11a*-expressing mDA neurons of the SNc have been shown to be highly susceptible to neurodegeneration. Interestingly, BCL11A is mainly expressed in the dorsal tier of the SNc and only 20% of these neurons overlap with the ALDH1A1 mDA positive subpopulation. These results are indicating a difference in vulnerability to neurodegeneration in neurons located within the SNc dorsal tier and that BCL11A is labelling the more vulnerable population that is projecting to the caudal DMS and to the ventral TS. Of note, as a result of α-synuclein overexpression in the SNc, a decrease in the TS innervation was observed in *Bcl11a* cko mice confirming the high specificity of *Bcl11a*-expressing SNc-mDA neurons to this target region. The DMS corresponds roughly to the caudate nucleus in the human brain (Burton et al., 2015). DA deficits within the striatum are unevenly distributed in Parkinson's disease patients and in general, neuroimaging studies show that the posterior putamen (corresponding to the DLS in rodents) has a more severe dopamine dysfunction than the caudate nucleus (Kish et al.,

1998). This gradient of DA deficiency has been reported to be already apparent at early disease stages and to be largely maintained over the course of the disease (Nandhagopal et al., 2009). Nevertheless, some of the early symptoms associated with Parkinson's disease, such as gait problems or REM sleep disorders, are most likely based on functional deficits of the caudate nucleus and the most dorsal and rostral part of the caudate nucleus has been reported to have a strong reduction in DA levels in Parkinson's disease patients. A recent study thus re-examined the involvement of DA deficiencies in the early stage of Parkinson's disease and found a significant DA de-innervation of the caudate nucleus in about half of the patients (Pasquini et al., 2019). *BCL11A* is expressed in human mDA neurons (La Manno et al., 2016; Tolve et al 2021 in press), but further studies will be necessary to evaluate which subpopulations is positive for *BCL11A* and whether a specific loss of *BCL11A*-expressing mDA neurons in PD patients might be associated with the reduced DA innervation of the caudate nucleus.

Results obtained in *Bcl11a* cko^lacZ mice show that the loss of *Bcl11a*-mDA neurons in these mice is significantly more severe compared to *Bcl11a-lacZ* control mice, thus indicating that BCL11A acts also as a neuroprotective factor in this population. A similar phenomenon has been observed for the ALDH1A1 expressing population. In fact, deletion of *Aldh1a1* exacerbates α-synuclein-mediated DA neurodegeneration and α-synuclein aggregation (Liu et al., 2014). This could be due to the particularly high vulnerability of these populations rather than to a specific function of these factors: any additional insult (i.e. loss of ALDH1A1 or BCL11A function) during development or in the adult brain increases their vulnerability even further. Alternatively, BCL11A could be modulating cell survival more directly. In fact, it regulates the expression of the anti-apoptotic factor Bcl2 in early B-lymphocytes and its inactivation in cortical projections neurons results in increased cell death in addition to deficits in migration and cell fate specification (Wiegreffe et al., 2015; Yu et al., 2012).

As described in section 5.4, the analysis of scRNAseq data in *BCL11A*-positive and *BCL11A*-negative cells in the SN-like population of hiPSC-derived mDA neurons revealed the differential expression of genes encoding for microtubule associated protein (Tolve et al., 2021). These genes have been previously shown to be implicated in neurodegenerative processes. Therefore, is it possible that BCL11A might have an impact on the balance between stable and dynamic microtubules thus acting as a neuroprotective factor against perturbances in microtubule dynamics that might contribute to degeneration. Another upregulated gene in human iPSC derived SN-like mDA neurons is the neuronal Ca^{2+} sensor 1 (NSC1) (Tolve et al., 2021). Several studies have shown that NCS1 acts as a protective factor by preventing calcium overload in SNc-mDA neurons. Inactivation of NSC1 in mice exacerbates degeneration of SNc-mDA neurons. In addition, NCS1 levels are reduced in an

hiPSC-model of familiar PD (Benkert et al., 2019). One possible mechanism by which BCL11A could act as neuroprotective factor for SNc-mDA neurons would be by positive regulation of NCS1 expression. Therefore, loss of *Bcl11a* in mDA neurons could lead to reduced NSC1 levels, which could contribute to increased susceptibility of these neurons to neurodegeneration.

The deficits in SN-mDA neurons demonstrate a novel role for BCL11A in regulating neuronal function and vulnerability that appears to be independent of its previously characterized role in cell fate specification (Simon et al., 2020). Whether the effect of BCL11A on SN-mDA neurons is a consequence of BCL11A acting during the development of mDA neurons by altering their molecular and functional profile and/or whether BCL11A regulates the function and vulnerability of mDA neurons acutely in the adult brain cannot be discerned from the current study. Given that BCL11A appears to be continuously expressed in the same mDA subpopulation starting soon after mDA differentiation and throughout adulthood, a role of BCL11A during mDA development seems likely. However, only the analysis of a mouse model, in which *Bcl11a* is inactivated in mDA neurons during adulthood, will address this point conclusively.

6. CONCLUSIONS

This study identified a zinc finger transcription factor, BCL11A (B-cell lymphoma 11a), which is expressed in about 20% and 40% of mDA neurons in the SN and VTA, respectively, and in 30% of RRF- and CLi-mDA neurons in the developing and adult brain.

Bcl11a-expressing mDA neurons, despite being broadly distributed across the different midbrain dopaminergic nuclei, form a highly specific subcircuit within the dopaminergic system. *Bcl11a*-expressing VTA-mDA neurons strongly innervate the OT and send their projections to the ventrolateral shell of the NAc and to the LS. *Bcl11a*-expressing SN-mDA neurons specifically innervate the medial DS and the ventral TS. Mice, in which *Bcl11a* is specifically inactivated in mDA neurons, show a rostral-to-caudal shift in the positioning of *Bcl11a*-mDA neurons of the VTA, a medial-to lateral shift in the positioning of *Bcl11a*-mDA neurons in the SNc and deficiencies in motor learning. These data suggest that loss of Bcl11a results in a functional impairment of mDA neurons. By challenging mDA neurons with α-synuclein overexpression, a model of Parkinson's disease, *Bcl11a*-expressing SN neurons are particularly vulnerable to neurodegeneration. Furthermore, loss of *Bcl11a* in this population increases their susceptibility to α-synuclein-induced degeneration.

For the first time, this study links the developmental origin of a specific subset of mDA neurons to their vulnerability phenotype and functional and circuit specialization. Thus, the results of this thesis demonstrate that a better understanding of the genetically defined developmental history of mDA neurons is most likely essential to understand the functional organization of the dopaminergic system and its susceptibility to neurodegeneration in the adult brain.

7. REFERENCES

Alves dos Santos, M. T., & Smidt, M. P. (2011). En1 and Wnt signaling in midbrain dopaminergic neuronal development. *Neural Development*, *6*(1), 23. https://doi.org/10.1186/1749-8104-6-23

Andersson, E., Tryggvason, U., Deng, Q., Friling, S., Alekseenko, Z., Robert, B., Perlmann, T., & Ericson, J. (2006). Identification of Intrinsic Determinants of Midbrain Dopamine Neurons. *Cell*, *124*(2), 393–405. https://doi.org/10.1016/j.cell.2005.10.037

Ang, S.-L. (2006). Transcriptional control of midbrain dopaminergic neuron development. *Development*, *133*(18), 3499–3506. https://doi.org/10.1242/dev.02501

Antonopoulos, J., Dinopoulos, A., Dori, I., & Parnavelas, G. J. (1997). *Distribution and synaptology of dopaminergic fibers in the mature and developing lateral septum of the rat. 102*, 135–141.

Arenas, E., Denham, M., & Villaescusa, J. C. (2015). How to make a midbrain dopaminergic neuron. *Development*, *142*(11), 1918–1936. https://doi.org/10.1242/dev.097394

AU - Luong, T. N., AU - Carlisle, H. J., AU - Southwell, A., & AU - Patterson, P. H. (2011). Assessment of Motor Balance and Coordination in Mice using the Balance Beam. *JoVE*, *49*, e2376. https://doi.org/10.3791/2376

Bäckman, C. M., Malik, N., Zhang, Y., Shan, L., Grinberg, A., Hoffer, B. J., Westphal, H., & Tomac, A. C. (2006). Characterization of a mouse strain expressing Cre recombinase from the 3′ untranslated region of the dopamine transporter locus. *Genesis*, *44*(8), 383–390. https://doi.org/10.1002/dvg.20228

Bariselli, S., Hörnberg, H., Prévost-Solié, C., Musardo, S., Hatstatt-Burklé, L., Scheiffele, P., & Bellone, C. (2018). Role of VTA dopamine neurons and neuroligin 3 in sociability traits related to nonfamiliar conspecific interaction. *Nature Communications*, *9*(1), 3173. https://doi.org/10.1038/s41467-018-05382-3

Basak, A., Hancarova, M., Ulirsch, J. C., Balci, T. B., Trkova, M., Pelisek, M., Vlckova, M., Muzikova, K., Cermak, J., Trka, J., Dyment, D. A., Orkin, S. H., Daly, M. J., Sedlacek, Z., & Sankaran, V. G. (2015). BCL11A deletions result in fetal hemoglobin persistence and neurodevelopmental alterations. *Journal of Clinical Investigation*, *125*(6), 2363–2368. https://doi.org/10.1172/JCI81163

Beier, K. T., Gao, X. J., Xie, S., DeLoach, K. E., Malenka, R. C., & Luo, L. (2019). Topological Organization of Ventral Tegmental Area Connectivity Revealed by Viral-Genetic Dissection of Input-Output Relations. *Cell Reports*, *26*(1), 159-167.e6. https://doi.org/10.1016/j.celrep.2018.12.040

Beier, K. T., Steinberg, E. E., DeLoach, K. E., Xie, S., Miyamichi, K., Schwarz, L., Gao, X. J., Kremer, E. J., Malenka, R. C., & Luo, L. (2015). Circuit Architecture of VTA Dopamine Neurons Revealed by Systematic Input-Output Mapping. *Cell*, *162*(3), 622–634. https://doi.org/10.1016/j.cell.2015.07.015

Benkert, J., Hess, S., Roy, S., Beccano-Kelly, D., Wiederspohn, N., Duda, J., Simons, C., Patil, K., Gaifullina, A., Mannal, N., Dragicevic, E., Spaich, D., Müller, S., Nemeth, J., Hollmann, H., Deuter, N., Mousba, Y., Kubisch, C., Poetschke, C., … Liss, B. (2019). Cav2.3 channels contribute to dopaminergic neuron loss in a model of Parkinson's disease. *Nature Communications*, *10*(1), 5094. https://doi.org/10.1038/s41467-019-12834-x

Bentivoglio, M., & Morelli, M. (2005). Chapter I The organization and circuits of mesencephalic dopaminergic neurons and the distribution of dopamine receptors in the brain. In *Handbook of Chemical Neuroanatomy* (Vol. 21, pp. 1–107). Elsevier. https://doi.org/10.1016/S0924-8196(05)80005-3

Bimpisidis, Z., König, N., Stagkourakis, S., Zell, V., Vlcek, B., Dumas, S., Giros, B., Broberger, C., Hnasko, T. S., & Wallén-Mackenzie, Å. (2019). The NeuroD6 Subtype of VTA Neurons Contributes to Psychostimulant Sensitization and Behavioral Reinforcement. *Eneuro*, *6*(3), ENEURO.0066-19.2019. https://doi.org/10.1523/ENEURO.0066-19.2019

Björklund, A., & Dunnett, S. B. (2007). Dopamine neuron systems in the brain: An update. *Trends in Neurosciences*, *30*(5), 194–202. https://doi.org/10.1016/j.tins.2007.03.006

Blaess, S., & Ang, S.-L. (2015). Genetic control of midbrain dopaminergic neuron development: Dopaminergic neuron development. *Wiley Interdisciplinary Reviews: Developmental Biology*, *4*(2), 113–134. https://doi.org/10.1002/wdev.169

Blaess, S., Bodea, G. O., Kabanova, A., Chanet, S., Mugniery, E., Derouiche, A., Stephen, D., & Joyner, A. L. (2011). Temporal-spatial changes in Sonic Hedgehog expression and signaling reveal different potentials of ventral mesencephalic progenitors to populate distinct ventral midbrain nuclei. *Neural Development*, *6*(1), 29. https://doi.org/10.1186/1749-8104-6-29

Bodea, G. O., Spille, J.-H., Abe, P., Andersson, A. S., Acker-Palmer, A., Stumm, R., Kubitscheck, U., & Blaess, S. (2014). Reelin and CXCL12 regulate distinct migratory behaviors during the development of the dopaminergic system. *Development*, *141*(3), 661–673. https://doi.org/10.1242/dev.099937

Breuss, M. W., Leca, I., Gstrein, T., Hansen, A. H., & Keays, D. A. (2017). Tubulins and brain development – The origins of functional specification. *Molecular and Cellular Neuroscience*, *84*, 58–67. https://doi.org/10.1016/j.mcn.2017.03.002

Burton, A. C., Nakamura, K., & Roesch, M. R. (2015). From ventral-medial to dorsal-lateral striatum: Neural correlates of reward-guided decision-making. *Neurobiology of Learning and Memory*, *117*, 51–59. https://doi.org/10.1016/j.nlm.2014.05.003

Cai, Y., & Ford, C. P. (2018). Dopamine Cells Differentially Regulate Striatal Cholinergic Transmission across Regions through Corelease of Dopamine and Glutamate. *Cell Reports*, *25*(11), 3148-3157.e3. https://doi.org/10.1016/j.celrep.2018.11.053

Cai, Y., Nielsen, B. E., Boxer, E. E., Aoto, J., & Ford, C. P. (2021). Loss of nigral excitation of cholinergic interneurons contributes to parkinsonian motor impairments. *Neuron*, S089662732100074X. https://doi.org/10.1016/j.neuron.2021.01.028

Canovas, J., Berndt, F. A., Sepulveda, H., Aguilar, R., Veloso, F. A., Montecino, M., Oliva, C., Maass, J. C., Sierralta, J., & Kukuljan, M. (2015). The Specification of Cortical Subcerebral Projection Neurons Depends on the Direct Repression of TBR1 by CTIP1/BCL11a. *Journal of Neuroscience*, *35*(19), 7552–7564. https://doi.org/10.1523/JNEUROSCI.0169-15.2015

Chaudhury, D., Walsh, J. J., Friedman, A. K., Juarez, B., Ku, S. M., Koo, J. W., Ferguson, D., Tsai, H.-C., Pomeranz, L., Christoffel, D. J., Nectow, A. R., Ekstrand, M., Domingos, A., Mazei-Robison, M. S., Mouzon, E., Lobo, M. K., Neve, R. L., Friedman, J. M., Russo, S. J., … Han, M.-H. (2013). Rapid regulation of depression-related behaviours by control of midbrain dopamine neurons. *Nature*, *493*(7433), 532–536. https://doi.org/10.1038/nature11713

Chen, L., Xie, Z., Turkson, S., & Zhuang, X. (2015). A53T Human -Synuclein Overexpression in Transgenic Mice Induces Pervasive Mitochondria Macroautophagy Defects Preceding Dopamine Neuron Degeneration. *Journal of Neuroscience*, *35*(3), 890–905. https://doi.org/10.1523/JNEUROSCI.0089-14.2015

Chenu, F., Mansari, M. E., & Blier, P. (2009). Long-term administration of monoamine oxidase inhibitors alters the firing rate and pattern of dopamine neurons in the ventral tegmental area. *The International Journal of Neuropsychopharmacology*, *12*(04), 475. https://doi.org/10.1017/S1461145708009218

Chuhma, N., Mingote, S., Yetnikoff, L., Kalmbach, A., Ma, T., Ztaou, S., Sienna, A.-C., Tepler, S., Poulin, J.-F., Ansorge, M., Awatramani, R., Kang, U. J., & Rayport, S. (2018). Dopamine neuron glutamate cotransmission evokes a delayed excitation in lateral dorsal striatal cholinergic interneurons. *ELife*, *7*, e39786. https://doi.org/10.7554/eLife.39786

Chung, C. Y., Seo, H., Sonntag, K. C., Brooks, A., Lin, L., & Isacson, O. (2005). Cell type-specific gene expression of midbrain dopaminergic neurons reveals molecules involved in their vulnerability and protection. *Human Molecular Genetics*, *14*(13), 1709–1725. https://doi.org/10.1093/hmg/ddi178

Cohen, J. Y., Haesler, S., Vong, L., Lowell, B. B., & Uchida, N. (2012). Neuron-type-specific signals for reward and punishment in the ventral tegmental area. *Nature*, *482*(7383), 85–88. https://doi.org/10.1038/nature10754

Conte, W. L., Kamishina, H., & Reep, R. L. (2009). Multiple neuroanatomical tract-tracing using fluorescent Alexa Fluor conjugates of cholera toxin subunit B in rats. *Nature Protocols*, *4*(8), 1157–1166. https://doi.org/10.1038/nprot.2009.93

Cooper, G. M., Coe, B. P., Girirajan, S., Rosenfeld, J. A., Vu, T. H., Baker, C., Williams, C., Stalker, H., Hamid, R., Hannig, V., Abdel-Hamid, H., Bader, P., McCracken, E., Niyazov, D., Leppig, K., Thiese, H., Hummel, M., Alexander, N., Gorski, J., … Eichler, E. E. (2011). A copy number variation morbidity map of developmental delay. *Nature Genetics*, *43*(9), 838–846. https://doi.org/10.1038/ng.909

Costa, R. M., Cohen, D., & Nicolelis, M. A. L. (2004). Differential Corticostriatal Plasticity during Fast and Slow Motor Skill Learning in Mice. *Current Biology*, *14*(13), 1124–1134. https://doi.org/10.1016/j.cub.2004.06.053

Dahlström, A., & Fuxe, K. (1964). Localization of monoamines in the lower brain stem. *Experientia*, *20*(7), 398–399. https://doi.org/10.1007/BF02147990

Dahlström, A., & Fuxe, K. (1965). *Monoamine neuron A B C groups original dopamine serotonin noradrenalin brain stem, Dalhstom Fuxe (Acta Physiol Scand 62).pdf*.

Dailly, E., Chenu, F., Renard, C. E., & Bourin, M. (2004). Dopamine, depression and antidepressants. *Fundamental and Clinical Pharmacology*, *18*(6), 601–607. https://doi.org/10.1111/j.1472-8206.2004.00287.x

De Bruyckere, E., Simon, R., Nestel, S., Heimrich, B., Kätzel, D., Egorov, A. V., Liu, P., Jenkins, N. A., Copeland, N. G., Schwegler, H., Draguhn, A., & Britsch, S. (2018). Stability and Function of Hippocampal Mossy Fiber Synapses Depend on Bcl11b/Ctip2. *Frontiers in Molecular Neuroscience*, *11*, 103. https://doi.org/10.3389/fnmol.2018.00103

de Jong, J. W., Afjei, S. A., Pollak Dorocic, I., Peck, J. R., Liu, C., Kim, C. K., Tian, L., Deisseroth, K., & Lammel, S. (2019). A Neural Circuit Mechanism for Encoding Aversive Stimuli in the Mesolimbic Dopamine System. *Neuron*, *101*(1), 133-151.e7. https://doi.org/10.1016/j.neuron.2018.11.005

Deuel, T. A. S., Liu, J. S., Corbo, J. C., Yoo, S.-Y., Rorke-Adams, L. B., & Walsh, C. A. (2006). Genetic Interactions between Doublecortin and Doublecortin-like Kinase in Neuronal Migration and Axon Outgrowth. *Neuron*, *49*(1), 41–53. https://doi.org/10.1016/j.neuron.2005.10.038

Deutch, A. Y., Goldstein, M., Baldino, F., & Roth, R. H. (1988). Telencephalic Projections of the A8 Dopamine Cell Group. *Annals of the New York Academy of Sciences*, *537*(1 The Mesocorti), 27–50. https://doi.org/10.1111/j.1749-6632.1988.tb42095.x

Di Salvio, M., Di Giovannantonio, L. G., Acampora, D., Prosperi, R., Omodei, D., Prakash, N., Wurst, W., & Simeone, A. (2010). Otx2 controls neuron subtype identity in ventral tegmental area and antagonizes vulnerability to MPTP. *Nature Neuroscience*, *13*(12), 1481–1488. https://doi.org/10.1038/nn.2661

Dias, C., Estruch, S. B., Graham, S. A., McRae, J., Sawiak, S. J., Hurst, J. A., Joss, S. K., Holder, S. E., Morton, J. E. V., Turner, C., Thevenon, J., Mellul, K., Sánchez-Andrade, G., Ibarra-Soria, X., Deriziotis, P., Santos, R. F., Lee, S.-C., Faivre, L., Kleefstra, T., … Logan, D. W. (2016). BCL11A Haploinsufficiency Causes an Intellectual Disability Syndrome and Dysregulates Transcription. *The American Journal of Human Genetics*, *99*(2), 253–274. https://doi.org/10.1016/j.ajhg.2016.05.030

Dodson, P. D., Dreyer, J. K., Jennings, K. A., Syed, E. C. J., Wade-Martins, R., Cragg, S. J., Bolam, J. P., & Magill, P. J. (2016). Representation of spontaneous movement by dopaminergic neurons is cell-type selective and disrupted in parkinsonism. *Proceedings of the National Academy of Sciences*, *113*(15), E2180–E2188. https://doi.org/10.1073/pnas.1515941113

Dumas, S., & Wallén-Mackenzie, Å. (2019). Developmental Co-expression of Vglut2 and Nurr1 in a Mes-Di-Encephalic Continuum Preceeds Dopamine and Glutamate Neuron

Specification. *Frontiers in Cell and Developmental Biology*, *7*, 307. https://doi.org/10.3389/fcell.2019.00307

Durieux, P. F., Schiffmann, S. N., & de Kerchove d'Exaerde, A. (2012). Differential regulation of motor control and response to dopaminergic drugs by D1R and D2R neurons in distinct dorsal striatum subregions: Dorsal striatum D1R- and D2R-neuron motor functions. *The EMBO Journal*, *31*(3), 640–653. https://doi.org/10.1038/emboj.2011.400

Edwards, N. J., Tejeda, H. A., Pignatelli, M., Zhang, S., McDevitt, R. A., Wu, J., Bass, C. E., Bettler, B., Morales, M., & Bonci, A. (2017). Circuit specificity in the inhibitory architecture of the VTA regulates cocaine-induced behavior. *Nature Neuroscience*, *20*(3), 438–448. https://doi.org/10.1038/nn.4482

El Yacoubi, M., Bouali, S., Popa, D., Naudon, L., Leroux-Nicollet, I., Hamon, M., Costentin, J., Adrien, J., & Vaugeois, J.-M. (2003). Behavioral, neurochemical, and electrophysiological characterization of a genetic mouse model of depression. *Proceedings of the National Academy of Sciences*, *100*(10), 6227–6232. https://doi.org/10.1073/pnas.1034823100

Engelhard, B., Finkelstein, J., Cox, J., Fleming, W., Jang, H. J., Ornelas, S., Koay, S. A., Thiberge, S. Y., Daw, N. D., Tank, D. W., & Witten, I. B. (2019). Specialized coding of sensory, motor and cognitive variables in VTA dopamine neurons. *Nature*, *570*(7762), 509–513. https://doi.org/10.1038/s41586-019-1261-9

Fallon, J. H., & Moore, R. Y. (1978). Catecholamine innervation of the basal forebrain IV. Topography of the dopamine projection to the basal forebrain and neostriatum. *The Journal of Comparative Neurology*, *180*(3), 545–579. https://doi.org/10.1002/cne.901800310

Farassat, N., Costa, K. M., Stojanovic, S., Albert, S., Kovacheva, L., Shin, J., Egger, R., Somayaji, M., Duvarci, S., Schneider, G., & Roeper, J. (2019). In vivo functional diversity of midbrain dopamine neurons within identified axonal projections. *ELife*, *8*, e48408. https://doi.org/10.7554/eLife.48408

Fernandes, H. J. R., Patikas, N., Foskolou, S., Field, S. F., Park, J.-E., Byrne, M. L., Bassett, A. R., & Metzakopian, E. (2020). Single-Cell Transcriptomics of Parkinson's Disease Human In Vitro Models Reveals Dopamine Neuron-Specific Stress Responses. *Cell Reports*, *33*(2), 108263. https://doi.org/10.1016/j.celrep.2020.108263

Ford, C. P. (2006). Properties and Opioid Inhibition of Mesolimbic Dopamine Neurons Vary according to Target Location. *Journal of Neuroscience*, *26*(10), 2788–2797. https://doi.org/10.1523/JNEUROSCI.4331-05.2006

Franklin, K. B., & Paxinos, G. (2007). *The Mouse Brain in Stereotaxic Coordinates, Third Edition.* (3rd ed.). Academic Press.

Fu, Y., Yuan, Y., Halliday, G., Rusznák, Z., Watson, C., & Paxinos, G. (2012). A cytoarchitectonic and chemoarchitectonic analysis of the dopamine cell groups in the substantia nigra, ventral tegmental area, and retrorubral field in the mouse. *Brain Structure and Function*, *217*(2), 591–612. https://doi.org/10.1007/s00429-011-0349-2

Gasbarri, A., Verney, C., Innocenzi, R., Campana, E., & Pacitti, C. (1994). Mesolimbic dopaminergic neurons innervating the hippocampal formation in the rat: A combined retrograde tracing and immunohistochemical study. *Brain Research*, *668*(1–2), 71–79. https://doi.org/10.1016/0006-8993(94)90512-6

German, D. C., Nelson, E. L., Liang, C.-L., Speciale, S. G., Sinton, C. M., & Sonsalla, P. K. (1996). The Neurotoxin MPTP Causes Degeneration of Specific Nucleus A8, A9 and A10 Dopaminergic Neurons in the Mouse. *Neurodegeneration*, *5*(4), 299–312. https://doi.org/10.1006/neur.1996.0041

Goedert, M., Spillantini, M. G., Del Tredici, K., & Braak, H. (2013). 100 years of Lewy pathology. *Nature Reviews Neurology*, *9*(1), 13–24. https://doi.org/10.1038/nrneurol.2012.242

Greene, J. G., Dingledine, R., & Greenamyre, J. T. (2005). Gene expression profiling of rat midbrain dopamine neurons: Implications for selective vulnerability in parkinsonism. *Neurobiology of Disease*, *18*(1), 19–31. https://doi.org/10.1016/j.nbd.2004.10.003

Greig, L. C., Woodworth, M. B., Greppi, C., & Macklis, J. D. (2016). Ctip1 Controls Acquisition of Sensory Area Identity and Establishment of Sensory Input Fields in the Developing Neocortex. *Neuron*, *90*(2), 261–277. https://doi.org/10.1016/j.neuron.2016.03.008

Grimm, J., Mueller, A., Hefti, F., & Rosenthal, A. (2004). Molecular basis for catecholaminergic neuron diversity. *Proceedings of the National Academy of Sciences*, *101*(38), 13891–13896. https://doi.org/10.1073/pnas.0405340101

Gunaydin, L. A., Grosenick, L., Finkelstein, J. C., Kauvar, I. V., Fenno, L. E., Adhikari, A., Lammel, S., Mirzabekov, J. J., Airan, R. D., Zalocusky, K. A., Tye, K. M., Anikeeva, P., Malenka, R. C., & Deisseroth, K. (2014). Natural Neural Projection Dynamics Underlying Social Behavior. *Cell*, *157*(7), 1535–1551. https://doi.org/10.1016/j.cell.2014.05.017

Hayes, L., Zhang, Z., Albert, P., Zervas, M., & Ahn, S. (2011). Timing of Sonic hedgehog and Gli1 expression segregates midbrain dopamine neurons. *The Journal of Comparative Neurology*, *519*(15), 3001–3018. https://doi.org/10.1002/cne.22711

Helwig, M., Klinkenberg, M., Rusconi, R., Musgrove, R. E., Majbour, N. K., El-Agnaf, O. M. A., Ulusoy, A., & Di Monte, D. A. (2016). Brain propagation of transduced α-synuclein involves non-fibrillar protein species and is enhanced in α-synuclein null mice. *Brain*, *139*(3), 856–870. https://doi.org/10.1093/brain/awv376

Heymann, G., Jo, Y. S., Reichard, K. L., McFarland, N., Chavkin, C., Palmiter, R. D., Soden, M. E., & Zweifel, L. S. (2020). Synergy of Distinct Dopamine Projection Populations in Behavioral Reinforcement. *Neuron*, *105*(5), 909-920.e5. https://doi.org/10.1016/j.neuron.2019.11.024

Hikosaka, O., Nakamura, K., Sakai, K., & Nakahara, H. (2002). Central mechanisms of motor skill learning. *Current Opinion in Neurobiology*, *12*(2), 217–222. https://doi.org/10.1016/S0959-4388(02)00307-0

Hnasko, T. S., Chuhma, N., Zhang, H., Goh, G. Y., Sulzer, D., Palmiter, R. D., Rayport, S., & Edwards, R. H. (2010). Vesicular Glutamate Transport Promotes Dopamine Storage and Glutamate Corelease In Vivo. *Neuron*, *65*(5), 643–656. https://doi.org/10.1016/j.neuron.2010.02.012

Hökfelt, T., Martensson, R., Björklund, A., Kleinau, S., & Goldtein, M. (1984). Distributional maps of tyrosine-hydroxylase- immunoreactive neurons in the rat brain. In A. Björklund & T. Hökfelt, *Handbook of Chemical Neuroanatomy*.

Hook, P. W., McClymont, S. A., Cannon, G. H., Law, W. D., Morton, A. J., Goff, L. A., & McCallion, A. S. (2018). Single-Cell RNA-Seq of Mouse Dopaminergic Neurons Informs Candidate Gene Selection for Sporadic Parkinson Disease. *The American Journal of Human Genetics*, *102*(3), 427–446. https://doi.org/10.1016/j.ajhg.2018.02.001

Ikemoto, S. (2007). Dopamine reward circuitry: Two projection systems from the ventral midbrain to the nucleus accumbens–olfactory tubercle complex. *Brain Research Reviews*, *56*(1), 27–78. https://doi.org/10.1016/j.brainresrev.2007.05.004

Iossifov, I., Ronemus, M., Levy, D., Wang, Z., Hakker, I., Rosenbaum, J., Yamrom, B., Lee, Y., Narzisi, G., Leotta, A., Kendall, J., Grabowska, E., Ma, B., Marks, S., Rodgers, L., Stepansky, A., Troge, J., Andrews, P., Bekritsky, M., … Wigler, M. (2012). De Novo Gene Disruptions in Children on the Autistic Spectrum. *Neuron*, *74*(2), 285–299. https://doi.org/10.1016/j.neuron.2012.04.009

John, A., Brylka, H., Wiegreffe, C., Simon, R., Liu, P., Juttner, R., Crenshaw, E. B., Luyten, F. P., Jenkins, N. A., Copeland, N. G., Birchmeier, C., & Britsch, S. (2012). Bcl11a is required for neuronal morphogenesis and sensory circuit formation in dorsal spinal cord development. *Development*, *139*(10), 1831–1841. https://doi.org/10.1242/dev.072850

Joksimovic, M., Anderegg, A., Roy, A., Campochiaro, L., Yun, B., Kittappa, R., McKay, R., & Awatramani, R. (2009). Spatiotemporally separable *Shh* domains in the midbrain define distinct dopaminergic progenitor pools. *Proceedings of the National Academy of Sciences*, *106*(45), 19185–19190. https://doi.org/10.1073/pnas.0904285106

Kadoch, C., Hargreaves, D. C., Hodges, C., Elias, L., Ho, L., Ranish, J., & Crabtree, G. R. (2013). Proteomic and bioinformatic analysis of mammalian SWI/SNF complexes identifies extensive roles in human malignancy. *Nature Genetics*, *45*(6), 592–601. https://doi.org/10.1038/ng.2628

Kawauchi, T. (2015). Cellullar insights into cerebral cortical development: Focusing on the locomotion mode of neuronal migration. *Frontiers in Cellular Neuroscience*, *9*. https://doi.org/10.3389/fncel.2015.00394

Khan, M. Z. (2017). Ionotropic glutamate receptors (iGluRs) of the delta family (GluD1 and GluD2) and synaptogenesis. *Alexandria Journal of Medicine*, *53*(3), 201–206. https://doi.org/10.1016/j.ajme.2016.09.003

Khan, S., Stott, S. R. W., Chabrat, A., Truckenbrodt, A. M., Spencer-Dene, B., Nave, K.-A., Guillemot, F., Levesque, M., & Ang, S.-L. (2017). Survival of a Novel Subset of Midbrain Dopaminergic Neurons Projecting to the Lateral Septum Is Dependent on NeuroD Proteins. *The Journal of Neuroscience*, *37*(9), 2305–2316. https://doi.org/10.1523/JNEUROSCI.2414-16.2016

Kim, J.-I., Ganesan, S., Luo, S. X., Wu, Y.-W., Park, E., Huang, E. J., Chen, L., & Ding, J. B. (2015). Aldehyde dehydrogenase 1a1 mediates a GABA synthesis pathway in midbrain dopaminergic neurons. *Science*, *350*(6256), 102–106. https://doi.org/10.1126/science.aac4690

Kish, S., Shannak, K., & Hornykiewicz, O. (1998). *Uneven Pattern of Dopamine Loss in the Striatum of Patients with Idiopathic Parkinson's Disease*. *318*(14), 876–880. https://doi.org/10.1056/NEJM199804073181402.

Koizumi, H., Tanaka, T., & Gleeson, J. G. (2006). Doublecortin-like kinase Functions with doublecortin to Mediate Fiber Tract Decussation and Neuronal Migration. *Neuron*, *49*(1), 55–66. https://doi.org/10.1016/j.neuron.2005.10.040

Kolk, S. M., Gunput, R.-A. F., Tran, T. S., van den Heuvel, D. M. A., Prasad, A. A., Hellemons, A. J. C. G. M., Adolfs, Y., Ginty, D. D., Kolodkin, A. L., Burbach, J. P. H., Smidt, M. P., & Pasterkamp, R. J. (2009). Semaphorin 3F Is a Bifunctional Guidance Cue for Dopaminergic Axons and Controls Their Fasciculation, Channeling, Rostral Growth, and Intracortical Targeting. *Journal of Neuroscience*, *29*(40), 12542–12557. https://doi.org/10.1523/JNEUROSCI.2521-09.2009

Kordower, J. H., Olanow, C. W., Dodiya, H. B., Chu, Y., Beach, T. G., Adler, C. H., Halliday, G. M., & Bartus, R. T. (2013). Disease duration and the integrity of the nigrostriatal system in Parkinson's disease. *Brain*, *136*(8), 2419–2431. https://doi.org/10.1093/brain/awt192

Kramer, D. J., Risso, D., Kosillo, P., Ngai, J., & Bateup, H. S. (2018). Combinatorial Expression of *Grp* and *Neurod6* Defines Dopamine Neuron Populations with Distinct Projection Patterns and Disease Vulnerability. *Eneuro*, *5*(3), ENEURO.0152-18.2018. https://doi.org/10.1523/ENEURO.0152-18.2018

La Manno, G., Gyllborg, D., Codeluppi, S., Nishimura, K., Salto, C., Zeisel, A., Borm, L. E., Stott, S. R. W., Toledo, E. M., Villaescusa, J. C., Lönnerberg, P., Ryge, J., Barker, R. A., Arenas, E., & Linnarsson, S. (2016). Molecular Diversity of Midbrain Development in Mouse, Human, and Stem Cells. *Cell*, *167*(2), 566-580.e19. https://doi.org/10.1016/j.cell.2016.09.027

Lammel, S., Hetzel, A., Häckel, O., Jones, I., Liss, B., & Roeper, J. (2008). Unique Properties of Mesoprefrontal Neurons within a Dual Mesocorticolimbic Dopamine System. *Neuron*, *57*(5), 760–773. https://doi.org/10.1016/j.neuron.2008.01.022

Lammel, S., Lim, B. K., & Malenka, R. C. (2014). Reward and aversion in a heterogeneous midbrain dopamine system. *Neuropharmacology*, *76*, 351–359. https://doi.org/10.1016/j.neuropharm.2013.03.019

Lammel, S., Lim, B. K., Ran, C., Huang, K. W., Betley, M. J., Tye, K. M., Deisseroth, K., & Malenka, R. C. (2012). Input-specific control of reward and aversion in the ventral tegmental area. *Nature*, *491*(7423), 212–217. https://doi.org/10.1038/nature11527

Lerner, T. N., Shilyansky, C., Davidson, T. J., Evans, K. E., Beier, K. T., Zalocusky, K. A., Crow, A. K., Malenka, R. C., Luo, L., Tomer, R., & Deisseroth, K. (2015). Intact-Brain

Analyses Reveal Distinct Information Carried by SNc Dopamine Subcircuits. *Cell*, *162*(3), 635–647. https://doi.org/10.1016/j.cell.2015.07.014

Li, X., Qi, J., Yamaguchi, T., Wang, H.-L., & Morales, M. (2013). Heterogeneous composition of dopamine neurons of the rat A10 region: Molecular evidence for diverse signaling properties. *Brain Structure and Function*, *218*(5), 1159–1176. https://doi.org/10.1007/s00429-012-0452-z

Liang, C.-L., Sinton, C. M., Sonsalla, P. K., & German, D. C. (1996). Midbrain Dopaminergic Neurons in the Mouse that Contain Calbindin-D28kExhibit Reduced Vulnerability to MPTP-induced Neurodegeneration. *Neurodegeneration*, *5*(4), 313–318. https://doi.org/10.1006/neur.1996.0042

Lindvall, O., & Björklund, A. (1974). *The organisation of the ascending catecholamine neuron system in the rat brain as revealed by the glyoxylic acid fluorescence method. 412*, 1–48.

Lindvall, O., Björklund, A., & Divac, I. (1977). *Organization of mesencephalic dopamine neurons projecting to neocortex and septum. 16*, 39–46.

Liss, B., Haeckel, O., Wildmann, J., Miki, T., Seino, S., & Roeper, J. (2005). K-ATP channels promote the differential degeneration of dopaminergic midbrain neurons. *Nature Neuroscience*, *8*(12), 1742–1751. https://doi.org/10.1038/nn1570

Liu, G., Yu, J., Ding, J., Xie, C., Sun, L., Rudenko, I., Zheng, W., Sastry, N., Luo, J., Rudow, G., Troncoso, J. C., & Cai, H. (2014). Aldehyde dehydrogenase 1 defines and protects a nigrostriatal dopaminergic neuron subpopulation. *Journal of Clinical Investigation*, *124*(7), 3032–3046. https://doi.org/10.1172/JCI72176

Liu, H., Ippolito, G. C., Wall, J. K., Niu, T., Probst, L., Lee, B.-S., Pulford, K., Banham, A. H., Stockwin, L., Shaffer, A. L., Staudt, L. M., Das, C., Dyer, M. J., & Tucker, P. W. (2006). Functional studies of BCL11A: characterization of the conserved BCL11A-XL splice variant and its interaction with BCL6 in nuclear paraspeckles of germinal center B cells. *Molecular Cancer*, *5*(1), 18. https://doi.org/10.1186/1476-4598-5-18

Madisen, L., Garner, A. R., Shimaoka, D., Chuong, A. S., Klapoetke, N. C., Li, L., van der Bourg, A., Niino, Y., Egolf, L., Monetti, C., Gu, H., Mills, M., Cheng, A., Tasic, B., Nguyen, T. N., Sunkin, S. M., Benucci, A., Nagy, A., Miyawaki, A., … Zeng, H. (2015). Transgenic Mice for Intersectional Targeting of Neural Sensors and Effectors with High Specificity and Performance. *Neuron*, *85*(5), 942–958. https://doi.org/10.1016/j.neuron.2015.02.022

Madisen, L., Zwingman, T. A., Sunkin, S. M., Oh, S. W., Zariwala, H. A., Gu, H., Ng, L. L., Palmiter, R. D., Hawrylycz, M. J., Jones, A. R., Lein, E. S., & Zeng, H. (2010). A robust and high-throughput Cre reporting and characterization system for the whole mouse brain. *Nature Neuroscience*, *13*(1), 133–140. https://doi.org/10.1038/nn.2467

Margolis, E. B., Lock, H., Hjelmstad, G. O., & Fields, H. L. (2006). The ventral tegmental area revisited: Is there an electrophysiological marker for dopaminergic neurons?: Electrophysiological properties of VTA neurons. *The Journal of Physiology*, *577*(3), 907–924. https://doi.org/10.1113/jphysiol.2006.117069

Margolis, E. B., Mitchell, J. M., Ishikawa, J., Hjelmstad, G. O., & Fields, H. L. (2008). Midbrain Dopamine Neurons: Projection Target Determines Action Potential Duration and Dopamine D2 Receptor Inhibition. *Journal of Neuroscience*, *28*(36), 8908–8913. https://doi.org/10.1523/JNEUROSCI.1526-08.2008

Matsumoto, M., & Hikosaka, O. (2009). Two types of dopamine neuron distinctly convey positive and negative motivational signals. *Nature*, *459*(7248), 837–841. https://doi.org/10.1038/nature08028

Menegas, W., Akiti, K., Amo, R., Uchida, N., & Watabe-Uchida, M. (2018). Dopamine neurons projecting to the posterior striatum reinforce avoidance of threatening stimuli. *Nature Neuroscience*, *21*(10), 1421–1430. https://doi.org/10.1038/s41593-018-0222-1

Menegas, W., Bergan, J. F., Ogawa, S. K., Isogai, Y., Umadevi Venkataraju, K., Osten, P., Uchida, N., & Watabe-Uchida, M. (2015). Dopamine neurons projecting to the posterior striatum form an anatomically distinct subclass. *ELife*, *4*, e10032. https://doi.org/10.7554/eLife.10032

Morales, M., & Margolis, E. B. (2017). Ventral tegmental area: Cellular heterogeneity, connectivity and behaviour. *Nature Reviews Neuroscience*, *18*(2), 73–85. https://doi.org/10.1038/nrn.2016.165

Nakamura, T., Yamazaki, Y., Saiki, Y., Moriyama, M., Largaespada, D. A., Jenkins, N. A., & Copeland, N. G. (2000). Evi9 Encodes a Novel Zinc Finger Protein That Physically Interacts with BCL6, a Known Human B-Cell Proto-Oncogene Product. *MOL. CELL. BIOL.*, *20*, 9.

Nandhagopal, R., Kuramoto, L., Schulzer, M., Mak, E., Cragg, J., Lee, C. S., McKenzie, J., McCormick, S., Samii, A., Troiano, A., Ruth, T. J., Sossi, V., de la Fuente-Fernandez, R., Calne, D. B., & Stoessl, A. J. (2009). Longitudinal progression of sporadic Parkinson's disease: A multi-tracer positron emission tomography study. *Brain*, *132*(11), 2970–2979. https://doi.org/10.1093/brain/awp209

Nelson, E. L., Liang, C. L., Sinton, C. M., & German, D. C. (1996). Midbrain dopaminergic neurons in the mouse: Computer-assisted mapping. *Journal of Comparative Neurology*, *369*(3), 361–371. https://doi.org/10.1002/(SICI)1096-9861(19960603)369:3<361::AID-CNE3>3.0.CO;2-3

Neuhoff, H., Neu, A., Liss, B., & Roeper, J. (2002). I_h Channels Contribute to the Different Functional Properties of Identified Dopaminergic Subpopulations in the Midbrain. *The Journal of Neuroscience*, *22*(4), 1290–1302. https://doi.org/10.1523/JNEUROSCI.22-04-01290.2002

Noseda, R., Kainz, V., Jakubowski, M., Gooley, J. J., Saper, C. B., Digre, K., & Burstein, R. (2010). A neural mechanism for exacerbation of headache by light. *Nature Neuroscience*, *13*(2), 239–245. https://doi.org/10.1038/nn.2475

Panman, L., Papathanou, M., Laguna, A., Oosterveen, T., Volakakis, N., Acampora, D., Kurtsdotter, I., Yoshitake, T., Kehr, J., Joodmardi, E., Muhr, J., Simeone, A., Ericson, J., & Perlmann, T. (2014). Sox6 and Otx2 Control the Specification of Substantia Nigra and Ventral Tegmental Area Dopamine Neurons. *Cell Reports*, *8*(4), 1018–1025. https://doi.org/10.1016/j.celrep.2014.07.016

Pasquini, J., Durcan, R., Wiblin, L., Gersel Stokholm, M., Rochester, L., Brooks, D. J., Burn, D., & Pavese, N. (2019). Clinical implications of early caudate dysfunction in Parkinson's disease. *Journal of Neurology, Neurosurgery & Psychiatry*, *90*(10), 1098–1104. https://doi.org/10.1136/jnnp-2018-320157

Peron, A., Bradbury, K., Viskochil, D. H., & Dias, C. (n.d.). *BCL11A-Related Intellectual Disability*. 17.

Phillips, R. A., Tuscher, J. J., Black, S. L., Ianov, L., & Day, J. J. (2021). *An atlas of transcriptionally defined cell populations in the rat ventral tegmental area* [Preprint]. Neuroscience. https://doi.org/10.1101/2021.06.02.446737

Poulin, J.-F., Caronia, G., Hofer, C., Cui, Q., Helm, B., Ramakrishnan, C., Chan, C. S., Dombeck, D. A., Deisseroth, K., & Awatramani, R. (2018). Mapping projections of molecularly defined dopamine neuron subtypes using intersectional genetic approaches. *Nature Neuroscience*, *21*(9), 1260–1271. https://doi.org/10.1038/s41593-018-0203-4

Poulin, J.-F., Gaertner, Z., Moreno-Ramos, O. A., & Awatramani, R. (2020). Classification of Midbrain Dopamine Neurons Using Single-Cell Gene Expression Profiling Approaches. *Trends in Neurosciences*, *43*(3), 155–169. https://doi.org/10.1016/j.tins.2020.01.004

Poulin, J.-F., Zou, J., Drouin-Ouellet, J., Kim, K.-Y. A., Cicchetti, F., & Awatramani, R. B. (2014). Defining Midbrain Dopaminergic Neuron Diversity by Single-Cell Gene Expression Profiling. *Cell Reports*, *9*(3), 930–943. https://doi.org/10.1016/j.celrep.2014.10.008

Roeper, J. (2013). Dissecting the diversity of midbrain dopamine neurons. *Trends in Neurosciences*, *36*(6), 336–342. https://doi.org/10.1016/j.tins.2013.03.003

Sánchez-Huertas, C., Bonhomme, M., Falco, A., Fagotto-Kaufmann, C., van Haren, J., Jeanneteau, F., Galjart, N., Debant, A., & Boudeau, J. (2020). The +TIP Navigator-1

is an actin–microtubule crosslinker that regulates axonal growth cone motility. *Journal of Cell Biology*, *219*(9), e201905199. https://doi.org/10.1083/jcb.201905199

Satterwhite, E., Sonoki, T., Willis, T. G., Harder, L., Nowak, R., Arriola, E. L., Liu, H., Price, H. P., Gesk, S., Steinemann, D., Schlegelberger, B., Oscier, D. G., Siebert, R., Tucker, P. W., & Dyer, M. J. S. (2001). The BCL11 gene family: Involvement of BCL11A in lymphoid malignancies. *Blood*, *98*(12), 3413–3420. https://doi.org/10.1182/blood.V98.12.3413

Saunders, A., Macosko, E. Z., Wysoker, A., Goldman, M., Krienen, F. M., de Rivera, H., Bien, E., Baum, M., Bortolin, L., Wang, S., Goeva, A., Nemesh, J., Kamitaki, N., Brumbaugh, S., Kulp, D., & McCarroll, S. A. (2018). Molecular Diversity and Specializations among the Cells of the Adult Mouse Brain. *Cell*, *174*(4), 1015-1030.e16. https://doi.org/10.1016/j.cell.2018.07.028

Schultz, W. (1997). Dopamine neurons and their role in reward mechanisms. *Current Opinion in Neurobiology*, *7*(2), 191–197. https://doi.org/10.1016/S0959-4388(97)80007-4

Schwamborn, J. C. (2018). Is Parkinson's Disease a Neurodevelopmental Disorder and Will Brain Organoids Help Us to Understand It? *Stem Cells and Development*, *27*(14), 968–975. https://doi.org/10.1089/scd.2017.0289

Silm, K., Yang, J., Marcott, P. F., Asensio, C. S., Eriksen, J., Guthrie, D. A., Newman, A. H., Ford, C. P., & Edwards, R. H. (2019). Synaptic Vesicle Recycling Pathway Determines Neurotransmitter Content and Release Properties. *Neuron*, *102*(4), 786-800.e5. https://doi.org/10.1016/j.neuron.2019.03.031

Simon, R., Baumann, L., Fischer, J., Seigfried, F. A., De Bruyckere, E., Liu, P., Jenkins, N. A., Copeland, N. G., Schwegler, H., & Britsch, S. (2016). Structure-function integrity of the adult hippocampus depends on the transcription factor Bᴄʟ11ʙ / Cᴛɪᴘ2. *Genes, Brain and Behavior*, *15*(4), 405–419. https://doi.org/10.1111/gbb.12287

Simon, R., Wiegreffe, C., & Britsch, S. (2020). Bcl11 Transcription Factors Regulate Cortical Development and Function. *Frontiers in Molecular Neuroscience*, *13*, 51. https://doi.org/10.3389/fnmol.2020.00051

Smidt, M. P., & Burbach, J. P. H. (2007). *How to make a mesodiencephalic dopaminergic neuron*. 12.

Stamatakis, A. M., Jennings, J. H., Ung, R. L., Blair, G. A., Weinberg, R. J., Neve, R. L., Boyce, F., Mattis, J., Ramakrishnan, C., Deisseroth, K., & Stuber, G. D. (2013). A Unique Population of Ventral Tegmental Area Neurons Inhibits the Lateral Habenula to Promote Reward. *Neuron*, *80*(4), 1039–1053. https://doi.org/10.1016/j.neuron.2013.08.023

Stuber, G. D., Hnasko, T. S., Britt, J. P., Edwards, R. H., & Bonci, A. (2010). Dopaminergic Terminals in the Nucleus Accumbens But Not the Dorsal Striatum Corelease Glutamate. *Journal of Neuroscience*, *30*(24), 8229–8233. https://doi.org/10.1523/JNEUROSCI.1754-10.2010

Sulzer, D. (2007). Multiple hit hypotheses for dopamine neuron loss in Parkinson's disease. *Trends in Neurosciences*, *30*(5), 244–250. https://doi.org/10.1016/j.tins.2007.03.009

Swanson, L. W. (1982). *The Projections of the Ventral Tegmental Area and Adjacent Regions: A Combined Fluorescent Retrograde Tracer and Immunofluorescence Study in the Rat*. *9*, 321–353.

Tarfa, R. A., Evans, R. C., & Khaliq, Z. M. (2017). Enhanced Sensitivity to Hyperpolarizing Inhibition in Mesoaccumbal Relative to Nigrostriatal Dopamine Neuron Subpopulations. *The Journal of Neuroscience*, *37*(12), 3311–3330. https://doi.org/10.1523/JNEUROSCI.2969-16.2017

The Deciphering Developmental Disorders Study. (2015). Large-scale discovery of novel genetic causes of developmental disorders. *Nature*, *519*(7542), 223–228. https://doi.org/10.1038/nature14135

Thompson, L. (2005). Identification of Dopaminergic Neurons of Nigral and Ventral Tegmental Area Subtypes in Grafts of Fetal Ventral Mesencephalon Based on Cell Morphology, Protein Expression, and Efferent Projections. *Journal of Neuroscience*, *25*(27), 6467–6477. https://doi.org/10.1523/JNEUROSCI.1676-05.2005

Tian, J., Huang, R., Cohen, J. Y., Osakada, F., Kobak, D., Machens, C. K., Callaway, E. M., Uchida, N., & Watabe-Uchida, M. (2016). Distributed and Mixed Information in Monosynaptic Inputs to Dopamine Neurons. *Neuron*, *91*(6), 1374–1389. https://doi.org/10.1016/j.neuron.2016.08.018

Tiklová, K., Björklund, Å. K., Lahti, L., Fiorenzano, A., Nolbrant, S., Gillberg, L., Volakakis, N., Yokota, C., Hilscher, M. M., Hauling, T., Holmström, F., Joodmardi, E., Nilsson, M., Parmar, M., & Perlmann, T. (2019). Single-cell RNA sequencing reveals midbrain dopamine neuron diversity emerging during mouse brain development. *Nature Communications*, *10*(1), 581. https://doi.org/10.1038/s41467-019-08453-1

Tolve, M., Ulusoy, A., Patikas, N. Sameen Islam, K. U., Bodea, G. O., Ötzürk, E., Broske, B., Mentani, A., Wagener, A., van Loo, K. M. J., Britsch, S., Liu, P., Khaled, W. T., Metzakopian, E., Baader, S. L., Di Monte, D. A., Blaess, (2021). S. The transcription factor BCL11A defines distinct subsets of midbrain dopaminergic neurons. *Cell Reports*, 36(11), 109697. https://doi.org/10.1016/j.celrep.2021.109697

Tritsch, N. X., Ding, J. B., & Sabatini, B. L. (2012). Dopaminergic neurons inhibit striatal output through non-canonical release of GABA. *Nature*, *490*(7419), 262–266. https://doi.org/10.1038/nature11466

Tye, K. M., Mirzabekov, J. J., Warden, M. R., Ferenczi, E. A., Tsai, H.-C., Finkelstein, J., Kim, S.-Y., Adhikari, A., Thompson, K. R., Andalman, A. S., Gunaydin, L. A., Witten, I. B., & Deisseroth, K. (2013). Dopamine neurons modulate neural encoding and expression of depression-related behaviour. *Nature*, *493*(7433), 537–541. https://doi.org/10.1038/nature11740

Ulusoy, A., & Di Monte, D. A. (2013). α-Synuclein Elevation in Human Neurodegenerative Diseases: Experimental, Pathogenetic, and Therapeutic Implications. *Molecular Neurobiology*, *47*(2), 484–494. https://doi.org/10.1007/s12035-012-8329-y

Van Hove, H., Antunes, A. R. P., De Vlaminck, K., Scheyltjens, I., Van Ginderachter, J. A., & Movahedi, K. (2020). Identifying the variables that drive tamoxifen-independent CreERT2 recombination: Implications for microglial fate mapping and gene deletions. *European Journal of Immunology*, *50*(3), 459–463. https://doi.org/10.1002/eji.201948162

Villarroel-Campos, D., & Gonzalez-Billault, C. (2014). The MAP1B case: An old MAP that is new again: Novel Roles for MAP1B. *Developmental Neurobiology*, *74*(10), 953–971. https://doi.org/10.1002/dneu.22178

Wang, F., Flanagan, J., Su, N., Wang, L.-C., Bui, S., Nielson, A., Wu, X., Vo, H.-T., Ma, X.-J., & Luo, Y. (2012). RNAscope. *The Journal of Molecular Diagnostics*, *14*(1), 22–29. https://doi.org/10.1016/j.jmoldx.2011.08.002

Watabe-Uchida, M., Zhu, L., Ogawa, S. K., Vamanrao, A., & Uchida, N. (2012). Whole-Brain Mapping of Direct Inputs to Midbrain Dopamine Neurons. *Neuron*, *74*(5), 858–873. https://doi.org/10.1016/j.neuron.2012.03.017

Wiegreffe, C., Simon, R., Peschkes, K., Kling, C., Strehle, M., Cheng, J., Srivatsa, S., Liu, P., Jenkins, N. A., Copeland, N. G., Tarabykin, V., & Britsch, S. (2015). Bcl11a (Ctip1) Controls Migration of Cortical Projection Neurons through Regulation of Sema3c. *Neuron*, *87*(2), 311–325. https://doi.org/10.1016/j.neuron.2015.06.023

Winterer, G., & Weinberger, D. R. (2004). Genes, dopamine and cortical signal-to-noise ratio in schizophrenia. *Trends in Neurosciences*, *27*(11), 683–690. https://doi.org/10.1016/j.tins.2004.08.002

Wise, R. A. (2009). Roles for nigrostriatal—Not just mesocorticolimbic—Dopamine in reward and addiction. *Trends in Neurosciences*, *32*(10), 517–524. https://doi.org/10.1016/j.tins.2009.06.004

Woodworth, M. B., Greig, L. C., Liu, K. X., Ippolito, G. C., Tucker, H. O., & Macklis, J. D. (2016). Ctip1 Regulates the Balance between Specification of Distinct Projection Neuron Subtypes in Deep Cortical Layers. *Cell Reports*, *15*(5), 999–1012. https://doi.org/10.1016/j.celrep.2016.03.064

Wu, J., Kung, J., Dong, J., Chang, L., Xie, C., Habib, A., Hawes, S., Yang, N., Chen, V., Liu, Z., Evans, R., Liang, B., Sun, L., Ding, J., Yu, J., Saez-Atienzar, S., Tang, B., Khaliq,

Z., Lin, D.-T., … Cai, H. (2019). Distinct Connectivity and Functionality of Aldehyde Dehydrogenase 1a1-Positive Nigrostriatal Dopaminergic Neurons in Motor Learning. *Cell Reports*, *28*(5), 1167-1181.e7. https://doi.org/10.1016/j.celrep.2019.06.095

Yu, Y., Wang, J., Khaled, W., Burke, S., Li, P., Chen, X., Yang, W., Jenkins, N. A., Copeland, N. G., Zhang, S., & Liu, P. (2012). Bcl11a is essential for lymphoid development and negatively regulates p53. *Journal of Experimental Medicine*, *209*(13), 2467–2483. https://doi.org/10.1084/jem.20121846

Zhang, S., Qi, J., Li, X., Wang, H.-L., Britt, J. P., Hoffman, A. F., Bonci, A., Lupica, C. R., & Morales, M. (2015). Dopaminergic and glutamatergic microdomains in a subset of rodent mesoaccumbens axons. *Nature Neuroscience*, *18*(3), 386–392. https://doi.org/10.1038/nn.3945

8. ACKNOWLEDGEMENTS

I would like to thank Prof. Dr. Sandra Blaess for giving me the opportunity to perform my PhD thesis in her working group. Her supervision, intellectual input, encouragement and advice have been essential throughout this research project and helped me to grow as a scientist. I would like to express my gratitude for her kind nature and empathy that she showed especially during the most challenging and toughest times of my doctoral thesis work. I also thank her for correcting this thesis with patience.

I thank Prof. Dr. Stephan Baader for supporting me with the behavioral experiments and for analysing the data. I also thank Prof. Dr. Donato A. Di Monte and Dr. Ayse Ulusoy for performing the a α-synuclein overexpression experiments presented in this study.

I would like to thank current and former members of Prof. Blaess´s lab: Ankita Vaswani, Erick Martinez Chavez, Viktoria Bosch, Alessandro Petese, Astrid Mentani, Ushna Khondker Sameen Islam, Adriàn Lopez Fernandez, Norisa Meli and Rui Lois Tan. I am grateful to all of them for providing a good working atmosphere in the lab, for helping me whenever possible and for all the coffee breaks and friendly talks. Special thanks go to Frederike Klaus, Michela Albertini, Ankita Vaswani, Fabio Marsoner, Kevin Weynans, Silvia Brocchetti, Astrid Mentani and Alessandro Petese. I am grateful for their friendship, support and positivity and for helping me in any possible way during the toughest times of this journey.

I would not have been able to complete this work without the help of my family. I am beyond grateful to my parents Donato and Maria Grazia, my brother Nicola and my grandparents Anna and Giuseppe. Their constant support and love but also hard work and sacrifices have allowed me to complete my studies and to be where I am now. Finally, I wish to thank my boyfriend Jonas for his love, support, patience and encouragement and for believing in me.

9. PUBLICATIONS AND CONFERENCES

Publications:

- **Tolve, M.**, Ulusoy, A., Patikas, N. Sameen Islam, K. U., Bodea, G. O., Ötzürk, E., Broske, B., Mentani, A., Wagener, A., van Loo, K. M. J., Britsch, S., Liu, P., Khaled, W. T., Metzakopian, E., Baader, S. L., Di Monte, D. A., Blaess, (2021). S. The transcription factor BCL11A defines distinct subsets of midbrain dopaminergic neurons. *Cell Reports*, 36(11), 109697. https://doi.org/10.1016/j.celrep.2021.109697
- Paß, T., Aßfalg, M., **Tolve, M.**, Blaess, S., Rothermel, M., Wiesner, R. J., Ricke, R. J. (2020). The impact of mitochondrial dysfunction on dopaminergic neurons of the olfactory bulb and odor detection. *Mol. Neurobiol.*, 57, 3646-3657. https://doi.org/10.1007/s12035-020-01947-w
- Gazea, M., Tasouri, E., **Tolve, M.**, Bosch, V., Kabanova, A., Gojak, C., Kurtulmus, B., Novikov, O., Spatz, J., Pereira, G., Hübner, W., Brodski, C., Ticker, K. L., Blaess, S. (2016). Primary cilia are critical for Sonic hedgehog-mediated dopaminergic neurogenesis in the embryonic midbrain. *Dev. Biol.*, 409(1), 55-71. https://doi.org/10.1016/j.ydbio.2015.10.033

Conferences and seminars:

- Development of the dopaminergic system – from stem cells to circuits. Conference, 13-15 May 2019, Crete, Greece. Poster presentation.
- 5[Th] Bonn Brain3 conference, 25-27 March 2019, Bonn, Germany. Talk, Young Investigator Research Session.
- "Chemical Neuromodulation", FENS SfN Summer School, 18-23 July 2017, Bertinoro, Italy. Poster presentation.